Recent Advances in Ball-Milled Materials and Their Applications for Adsorptive Removal of Aqueous Pollutants

Pei Gao [1,*], Xuanhao Fan [1], Da Sun [2,*], Guoming Zeng [1], Quanfeng Wang [1] and Qihui Wang [1]

1   School of Civil Engineering and Architecture, Chongqing University of Science and Technology, Chongqing 401331, China
2   Institute of Life Sciences & Biomedical Collaborative Innovation Center, Wenzhou University, Wenzhou 325035, China
*   Correspondence: rococo_gao@163.com (P.G.); sunday@wzu.edu.cn (D.S.)

Abstract: Ball milling, as a cost-effective and eco-friendly approach, has been popular in materials synthesis to solve problems involving toxic reagents, high temperatures, or high pressure, which has the potential for large-scale production. However, there are few reviews specifically concentrating on the latest progress in materials characteristics before and after ball milling as well as the adsorptive application for aqueous pollutants. Hence, this paper summarized the principle and classification of ball milling and reviewed the advances of mechanochemical materials in categories as well as their adsorption performance of organic and inorganic pollutants. Ball milling has the capacity to change materials' crystal structure, specific surface areas, pore volumes, and particle sizes and even promote grafting reactions to obtain functional groups to surfaces. This improved the adsorption amount, changed the equilibrium time, and strengthened the adsorption force for contaminants. Most studies showed that the Langmuir model and pseudo-second-order model fitted experimental data well. The regeneration methods include ball milling and thermal and solvent methods. The potential future developments in this field were also proposed. This work tries to review the latest advances in ball-milled materials and their application for pollutant adsorption and provides a comprehensive understanding of the physicochemical properties of materials before and after ball milling, as well as their effects on pollutants' adsorption behavior. This is conducive to laying a foundation for further research on water decontamination by ball-milled materials.

Keywords: ball milling; adsorbents; aqueous pollutants; physicochemical property; regeneration performance

1. Introduction

With the rapid development of society and the economy, environmental pollution caused by organic and inorganic substances has gained significant concerns due to the potential adverse risks to aquatic environments and human health [1,2]. The excess emission of heavy metals is susceptible to causing diseases such as chronic poisoning [3], lung cancer [4], and kidney cancer [5]. The accumulation of colored dyes in water not only has disadvantages on the photosynthesis process in aquatic plants but also causes carcinogenicity and mutagenicity in human bodies [6]. The widespread antibiotic residues in water resulting from improper use of medicines and unabsorbed loss are capable of causing high levels of antibiotic resistance to threaten human health [7]. Therefore, in order to solve these serious problems, various techniques have been chosen for water decontamination, including adsorption [8–10], microbiological methods [11,12], advanced oxidation process [13–15], and membrane technology [16–18]. Among them, adsorption is considered one of the most suitable techniques due to its simplicity, effective removal of pollutants, and environmental friendliness [19]. Various techniques are reported to prepare materials for adsorption, such as pyrolysis, hydrothermal synthesis, and co-precipitation. But, the

disadvantages of these methods limit their potential for large production. For example, although the operation of the pyrolysis method is simple, it involves high temperature, large energy consumption, long process time, and gaseous pollutants [20,21]. Despite the reaction of hydrothermal synthesis being chemical, it requires high pressure, high temperature, or both of them to prepare materials [22,23]. Co-precipitation has a short reaction time, but the use of large amounts of solvents and even toxic reagents results in expensive cost and safety risks [24,25]. On the contrary, the ball milling technology provides an environmentally friendly method for preparing/modifying materials due to the mild reaction conditions, high efficiency, low energy consumption, and technical and economic feasibility [26–28]. So far, a large numbers of ball-milled materials, such as commercial activated carbons [29], biochars [30], carbon nanotubes (CNTs) [31], graphenes [32], zero-valent irons (ZVIs) [33], zero-valent aluminums (ZVAls) [34] and their modified materials have been already reported for water decontamination.

However, the current reviews on ball milling mostly concentrated on biochars and biochar-based nanocomposites for gas and aqueous pollutants removal [35,36], single-atom catalysts for versatile catalytic applications [37], ball-milled catalysts, and reagents for water decontamination [38,39], ball-milled ZVIs for pollution remediation [40] and ball milling technology for the treatment of contaminated soils [41]. To the best of our knowledge, there are almost no reviews only concentrating on the reported ball-milled materials and their effectiveness in the adsorptive removal of inorganic and organic pollutants from water. Therefore, this review aims to describe the principle of ball milling for materials, review the advances in the reported ball-milled materials, evaluate the changes in the physicochemical properties of materials before and after ball milling, and adsorption performance of the ball-milled adsorbents. Adsorption mechanisms between adsorbents and aqueous pollutants are also investigated, as well as regeneration studies. This work tries to fill the gaps caused by the scattered knowledge and provides a thorough understanding of the adsorption behavior associated with ball-milled adsorbents.

2. Principles and Mechanisms of Ball Milling

Ball milling is a mechanical process that intentionally induces reactions among solids or solidified reagents both physically and chemically in solvent-free or limited solvent conditions. Non-hydrostatic mechanical stress and related strain generated in the ball milling process affect the physical and chemical behaviors of individual molecules, as well as ordered and disordered solids [42]. These transformations occur locally, specifically in regions where the conditions for mechanical deformation are met [43,44]. In general, ball milling relies on collisions between milling tools and an intermittent reactor containing powder materials (Figure 1). During each collision, a portion of the powder is trapped on the reactor surface and experiences mechanical loads [45]. This typically results in repeated processes, such as compress, crack, fracture, and cold welding, to induce physical and chemical transformations to the generation, migration, and interaction of lattice defects. In terms of whether the liquid is added to a grinding process, ball milling treatment is divided into dry ball milling and wet ball milling. Dry ball milling grinds with only precursors or with solid chemicals together. The commonly reported solid chemicals include metal oxide powders [46], sulfur powders [47], and zero-valent metals [48], which could change materials' surface functional groups or obtain magnetic properties for simple separation. But, because of the shape of the tanks, the materials in the dead space could not be adequately milled, and the materials tend to sink to the bottom during a dry ball milling process. This leads to an incomplete reaction. The addition of solvents is available to promote the mobility of the mixed precursors, improve the above phenomenon, and even trigger desired reactions [39]. Water [49], ethanol [50], and NaCl solution [51] are often used as grinding aids, while hydrogen peroxide [52], acid solutions [53], alkaline solutions [54], and silane coupling agents [55] are applied to change materials' surface functional groups. The materials obtained by a wet ball milling method have relatively concentrated particle dispersion and tend to agglomerate [37]. However, ball milling is still

a simple and environmentally friendly mechanochemical method for grinding powder into fine particles with rough morphology [30,56–59], introducing oxygen-containing functional group to the surface [59,60] and preparing desired targeted materials, compared to other conventional methods.

A ball milling process is realized by a ball grinding mill machine. The working method is to put precursors and grinding mediums into a ball mill container and set operating parameters. Because ball milling is a mechanochemical reaction, it transforms the energy obtained from the grinding mill into the materials to be ground [40]. The operating parameters are capable of controlling the input energy, such as milling speed [60], milling time [61], the ball-to-powder ratio, the size and quality of balls [62], etc. The high milling speed, long milling time, and low ball-to-powder ratio contribute to high input energy with unavoidable frictional energy to heat materials [63]. Heat, in some cases, can induce physical and chemical reactions to obtain the desired materials. But sometimes, the excessively high heat is disadvantageous to materials preparation, such as the formation of undesired phase, sacrificial crystallinity, and destroyed construction [63–66]. The interposition of pauses in a ball milling treatment or operation in jars with appropriate temperature control is beneficial to avoid this unwanted heating effect [67].

Based on the movement of containers and balls, ball grinding mills are categorized into four types, namely a stirred ball mill (Figure 2a), a vibration ball mill (Figure 2b), a tumbler ball mill (Figure 2c), and a planetary ball mill (Figure 2d). A stirred ball mill consists of a cylindrical abrasive chamber and a stirrer. Fine media, particles, and liquids are placed into a stirring motion through a rotating axis. The density of the medium has a major effect on the products [68]. A vibrating ball mill consists of a cylindrical container containing grinding balls. It vibrates in a vertical/horizontal direction to produce high milling forces, which provides relatively high noise levels and noticeable dust dispersion during a grinding process [69]. A tumbler ball mill contains a cylinder with milling balls in which an axial rotation causes these balls to roll down and impact against the powder [35]. A planetary ball mill commonly consists of four jars arranged on a wheel eccentrically. The wheel and jars are rotated in opposite directions, generating the impact force, squeezing force, and friction force to synthesize/modify materials. The materials are sealed in ball milling jars during a grinding process to prevent dust dispersion [62]. A planetary ball mill is capable of providing high-energy transfers. Based on the above advantages, planetary ball mills are commonly employed for materials synthesis/modification.
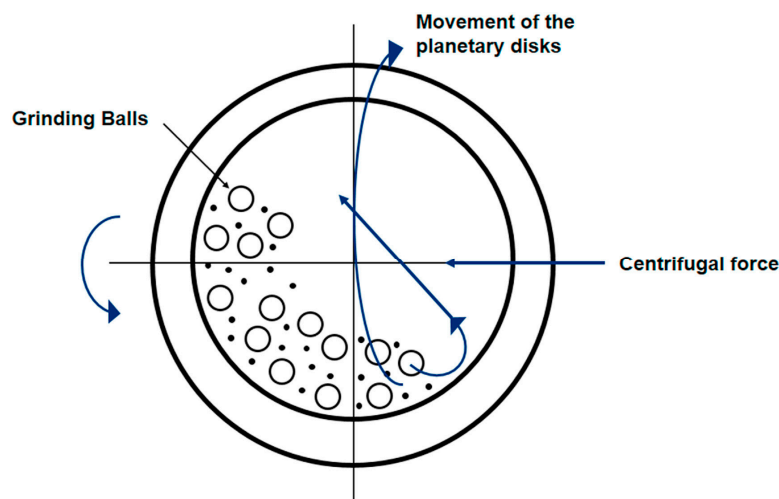

Figure 1. Horizontal section of a grinding container and powder mixture [70]. Reprinted from Current Research Green and Sustainable Chemistry, 5, Thambiliyagodage C., Wijesekera R., Ball milling—A green and sustainable technique for the preparation of titanium based materials from ilmenite, 100236, Copyright (2022), with permission from Elsevier.
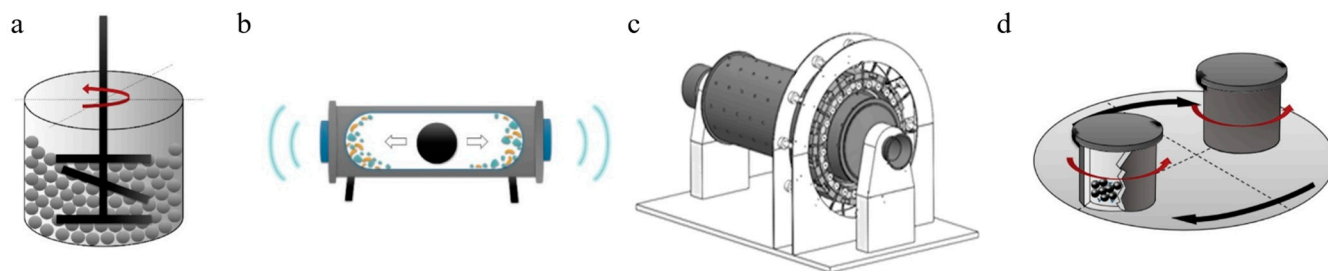
Figure 2. The classification of ball mills: (**a**) a stirred ball mill, (**b**) a vibration ball mill, (**c**) a tumbler ball mill, and (**d**) a planetary ball mill [39,71]. Reprinted from Science of The Total Environment, 825, Yin Z., Zhang Q., Li S.; Cagnetta G., Huang J., Deng S., Yu G., Mechanochemical synthesis of catalysts and reagents for water decontamination: Recent advances and perspective, 153992, Copyright (2022), with permission from Elsevier. Reprinted from LET Electric Power Applications, 16, Xu Y., Zhang B., Feng G., Electromagnetic design and thermal analysis of module combined permanent magnet motor with wrapped type for mine ball mill, 139–157, Copyright (2021), with permission from Wiley.

3. Ball-Milled Materials

3.1. Ball-Milled Commercial Activated Carbons

Commercial activated carbons have been widely applied in water purification with large specific surface area and pore volumes [72]. In recent years, ball milling technology has been applied to modify activated carbons (ACs). Bae et al. [73] subjected ACs to 40 h of milling, resulting in an increase in specific surface area from 1155 m^2/g to 1317 m^2/g with micropore volume increasing from 0.583 cm^3/g to 0.654 cm^3/g. This was mainly owing to the destruction of channeled inter-particular pores rather than intra-pores. Similarly, Fang et al. [9] reported that the specific surface area of ACs increased from 846 m^2/g to 929 m^2/g after ball milling 20 μm sized ACs with 5 mm sized steel balls for 60 min. Many carboxylic groups were formed during the ball milling process, which led to more negative zeta potentials. Ball milling also has the ability to prepare super-fine powdered ACs (-1.0 mm), which had a higher external surface area (720 m^2/g) and meso- and macropores (0.2102 cm^3/g) than the origin one (208.5 m^2/g and 0.0316 cm^3/g) [74]. However, Yuan et al. [75] claimed a significant decrease in the specific surface area of ACs after ball milling and an increase in crystallinity and bulk-phase oxygen contents due to a rearrangement or oxidation of defective carbon atoms. Nasrullah et al. [56] presented that there was no direct correlation between specific surface area and ball milling time, but the particle size of ACs decreased with increasing milling time.

The functionalized ACs could be simply obtained by the addition of modifiers during a ball milling process. Carbon quantum dots prepared by ball milling a mixture of ACs and KOH followed by an ultrafiltration purification had a large amount of oxygen-containing functional groups confirmed by the stretching vibrations of –OH, –C=O, and –C–O [76]. Ball milling ACs with NaOH for 6 h could form –OH on the surface of materials, and –OH was transformed to –COOH by ball milling them with chloroacetic acid again [77] (Figure 3a). Wang et al. [8] ball-milled ZVIs with ACs for 30 min at 300 rpm to obtain ball-milled iron–carbon composites (ZVIs-ACs), which had a significant increase in specific surface area (16.9 m^2/g) than that of the original micron-scale ZVIs (1.49 m^2/g). Shan et al. [78] synthetized an ultrafine magnetic composite by ball milling ACs with Fe_3O_4 for 2 h. It was observed that there was a decrease in the specific surface area and pore volumes compared to raw ACs, which were ascribed to the block by nanoscale Fe_3O_4 generated in the ball milling process. Similarly, the porous network of Fe_3O_4-modified ACs was found to be somewhat damaged, resulting in a decrease in both the specific surface area and pore volume. But the surface of the obtained materials was smoother and the amount of acidic functional group was higher than raw ACs [57].
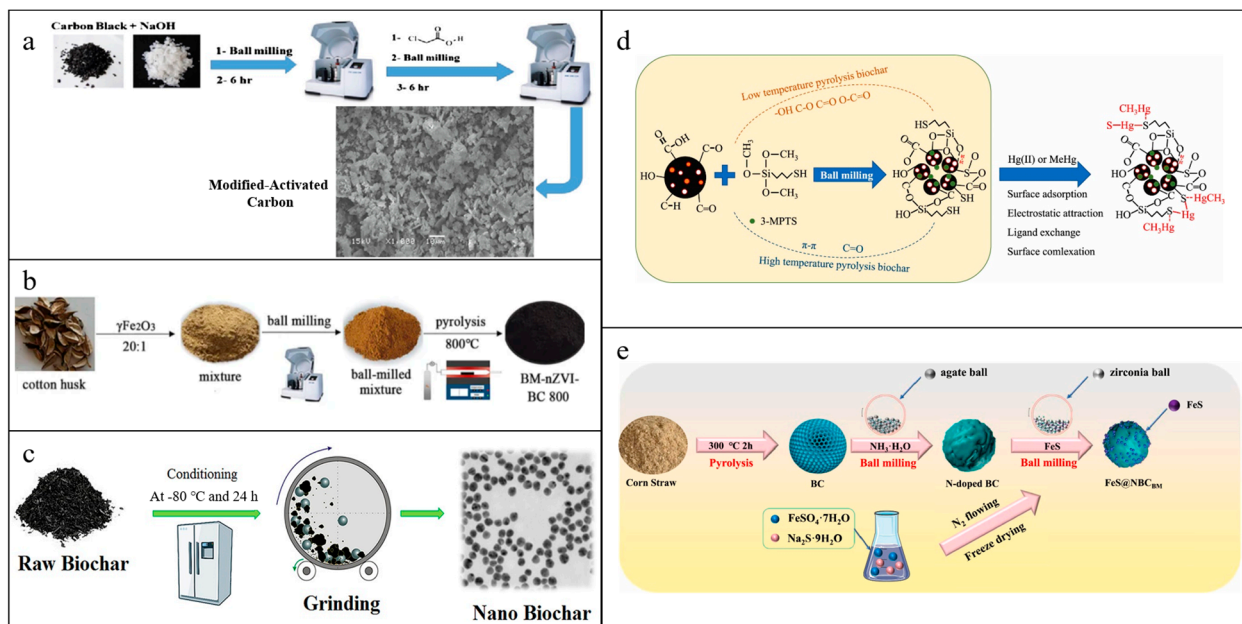
Figure 3. Schematic representation of (**a**) carboxylic groups-modified ACs (AC-COOH) [77], (**b**) ball-milled iron–biochar composites [79], (**c**) nanobiochars [80], (**d**) thiol-modified biochars [55], (**e**) BM-FeS@NBCs [10] preparation. (**a**) Reprinted from Journal of Molecular Liquids, 346, Sh. Gohr M., Abd-Elhamid A.I., El-Shanshory A.A., Soliman H.M.A., Adsorption of cationic dyes onto chemically modified activated carbon: Kinetics and thermodynamic study, 118227, Copyright (2022), with permission from Elsevier. (**b**) Reprinted from Environmental Science And Pollution Research, 30, Chen C., Yang F., Beesley L., Trakal L., Ma Y., Sun Y., Zhang Z., Ding Y., Removal of cadmium in aqueous solutions using a ball milling-assisted one-pot pyrolyzed iron-biochar composite derived from cotton husk, 12571–12583, Copyright (2023), with permission from Springer Nature. (**c**) Reprinted from Journal of Cleaner Production, 164, Naghdi M., Taheran M., Brar S.K., Rouissi T., Verma M., Surampalli R.Y., Valero J.R., A green method for production of nanobiochar by ball milling-optimization and characterization, 1394–1405, Copyright (2017), with permission from Elsevier. (**d**) Reprinted from Chemosphere, 294, Zhao L., Zhang Y., Wang L., Lyu H., Xia S., Tang J., Effective removal of Hg(II) and MeHg from aqueous environment by ball milling aided thiol-modification of biochars: Effect of different pyrolysis temperatures, 133820., Copyright (2022), with permission from Elsevier. (**e**) Reprinted from Environmental Pollution, 306, Qu J., Zhang W., Bi F., Yan S., Miao X., Zhang B., Wang Y., Ge C., Zhang Y., Two-step ball milling-assisted synthesis of N-doped biochar loaded with ferrous sulfide for enhanced adsorptive removal of Cr(VI) and tetracycline from water, 119398, Copyright (2022), with permission from Elsevier.

3.2. Ball-Milled Biochar-Based Materials

Although biochars are carbon-rich materials produced from low-cost and widely available biomass residues through simple pyrolysis, the drawbacks of low specific surface area and few functional groups limit their application. Ball milling is an effective route to address the above problems [30,58,59]. Based on the order of ball milling and pyrolysis, ball milling technology in biochar preparation/modification is classified as ball milling before biomass pyrolysis, ball milling after biomass pyrolysis, and ball milling biomass without pyrolysis.

Ball milling before biomass pyrolysis could change the biomass structure or mix with modifiers uniformly to functionalize materials. Ball milling unfolded the fibers of newspapers into a large plane and destroyed the fiber network and pores, leading to a decrease in the newspaper-derived biochars' specific surface area and pores. On the contrary, ball milling compressed the porous structure of straws into a denser and thinner one, resulting in an increase in specific surface area and pores of the straw-derived biochars [33]. Chen et al. [79] showed that ball milling biomass with γ-Fe$_2$O$_3$ before

pyrolysis was beneficial to making ZVls produced in the pyrolysis process more uniform, dispersed, and regular in biochars, compared to the one prepared without ball milling. And it also reduced the blockage of pores and was conductive to form the mesoporous structure (Figure 3b). Liu et al. [81] implied ball milling eggshells with rice straw powders and then pyrolysis to transform the calcium carbonate in eggshells to CaO and CO_2 to obtain CaO–biochar composites. The formation of CO_2 in the pyrolysis process could act as an activation agent to broaden the pore sizes of materials and increase specific surface area and pore volume. Ball milling cellulose with minerals (montmorillonite, calcite, and quartz) and then pyrolysis could change the obtained composites' microstructure, morphology, and surface properties [82].

There are two main strategies for the classification of ball milling after biomass pyrolysis: (1) ball milling biochars and (2) ball milling biochars with modifiers. Ball milling raw/modified biochars are similar to ACs, which changes the specific surface area and pore volumes, reduces particle sizes, introduces oxygen-containing functional groups to the surfaces in the form of C–O, C=O, and –OH, exposures more active sites, and prepares nanoscale biochars (Figure 3c) [80,83,84]. Furthermore, Zou et al. [85] suggested that ball milling changed the physicochemical properties of iron oxides in the biochars. The existing forms of iron oxide particles loaded on the biochars before ball milling were magnetite and lepidocrocite, but all of them changed to magnetite after ball milling. Calcination temperature is one of the significant factors in the specific surface area of ball-milled biochars. Lyu et al. [86] showed that ball milling increased only the external specific surface area of low-temperature pyrolyzed biochars (300 °C) by reducing their grain sizes, while ball milling increased both external and internal specific surface area of high-temperature pyrolyzated biochars (450 °C) by decreasing grain sizes and opening pores. The milling atmosphere is another important factor in surface morphology and functional groups of ball-milled biochars. Xu et al. [87] observed that N_2 and vacuum atmosphere were beneficial in reducing biochars' sizes and inhibited the introduction of oxygen-containing functional groups to biochars' surfaces than air atmosphere.

Ball milling biochars with modifiers is a simple way to realize biochar modification. H_2O_2 added in the ball milling process facilitated the opening of closed pores of biochars derived from high pyrolysis temperatures (600 °C), thereby increasing specific surface area, while it reduced the specific surface area of biochars derived from low pyrolysis temperatures (300 °C and 450 °C) by blocking microspores [88]. Phytic acid was employed to introduce P-containing moiety to biochars via a ball milling route, reducing grain sizes and increasing the microporous surface area by exposing blocked microspore networks [89]. The addition of alkaline ammonia solution in a ball milling process could prepare N-doped biochars by a facile method to solve the problem of traditional methods involving complicated synthetic steps or specific machinery [88]. N-doped biochars were obtained by ball milling biochars (1.8 g) with $NH_3 \cdot H_2O$ (18 mL, 29%) in 500 mL agate jars containing 180 g agate balls at 300 rpm for 12 h with the rolling orientation shifted each 3 h. Most of the N was loaded on the surface of ball-milled biochars in the forms of –NH_2 and C≡N through the dehydration of –COOH and –OH [90]. Qu et al. [10,91] also successfully synthesized N-doped biochars by ball milling biochars (1 g), $NH_3 \cdot H_2O$ (15 mL), and agate balls (15, 10, and 6 mm in diameter, mass ratio = 1:10:11) at 300 rpm for 12 h. In order to avoid oxidation during preparation, the agate pot was cleaned by purified N_2 (>99%) for at least 30 min before ball milling. In addition, urea was also used as an N-precursor to prepare N-doped biochars via a ball milling route to cover the shortage of $NH_3 \cdot H_2O$ with toxicity, un-safety, and volatility [92]. Thiol groups could be successfully loaded on the surface of biochars through –OH, C–O, and C=O by ball milling biochars with 3-trimethoxysilylpropanethiol (3-MPTS) in agate jars containing agate balls, water, and ethanol for 30 h at a speed of 400 rpm [55,93]. The low-temperature pyrolyzated biochars were conducive to graft thiol groups due to high oxygen-containing functional groups. Furthermore, the formed oxygen-containing functional groups during the ball milling process could also facilitate the loading of –SH groups (Figure 3d) [55]. P-doped biochars

were obtained by mixing red phosphorus (0.5 g) with biochars (10 g) into an agate tank (containing 200 g agate balls) and running at 300 rpm for 12 h [94]. MgO [95], CuO [96], ZnO [97], attapulgite [98], and vermiculites [99] could also be introduced to the surface of biochars via a ball milling way, which occupied the interstitial pores of biochars and led to a decrease in specific surface area. A FeS_2–biochar composite was prepared by ball milling biochar with natural pyrite [100,101]. Zhao et al. [102] reported that biochars ball milled with $Fe(NO_3)_3 \cdot 9H_2O$ and Na_2CO_3 solution for 24 h at 200 rpm could produce an α–FeOOH/biochar composite while promoting the degree of graphitization.

Magnetic biochars (MBCs) are widely used materials due to their recyclability, whereas Fe_3O_4 particles are extremely popular in a ball milling method. Shi et al. [103] synthesized MBCs by ball milling biochars with Fe_3O_4 in a 500 mL agate tank containing 180 g agate ball at 400 rpm for 24 h in ambient air. The rotation direction was altered every 6 h. The characterization of MBCs showed that Fe was successfully loaded on the biochars' surface, and an increase in the external surface area was ascribed to the diameter reducing from 10 μm to approximately 1 μm. The methods of synthesizing MBCs reported by Shan et al. [78] and Li et al. [104] were similar to the above method.

Ball milling is also an effective way to realize dual functions for materials. A novel nanocomposite CeO_2/Fe_3O_4/biochar was synthesized by ball milling biochars, Fe_3O_4 and CeO_2 (weight ratio = 0.54:1:0.33) simultaneously at 500 rpm for 12 h. The rotation direction was changed every 3 h with an interval of 5 min [105]. Ai et al. [106] also implied that sulfur-doped nano zero-valent iron–biochar composites (BM-SnZVI@BC) were obtained by ball milling biochars, sulfur powders, and iron powders with zirconia balls simultaneously at 400 rpm for 12 h. This method not only synthesized the bifunctional biochars but also solved the easy agglomeration and aging difficulties of ZVIs. The N-doped biochar loaded with FeS (BM-FeS@NBCs) was prepared by a two-step ball milling method. The N-doped biochar was firstly prepared by mixing biochars and $NH_3 \cdot H_2O$ (mass ratio = 1:15) with 45 g of agate balls in N_2 atmosphere at speed of 300 rpm. Then, the obtained N-doped biochar was ball milled again with FeS (mass ratio = 2:1) at the same ball milling parameters to address the agglomeration of FeS (Figure 3e) [10,91]. As one of the mineral materials, layered double hydroxides (LDHs) possessing controllable composition, favorable ion exchange capacity, and nontoxicity have gained much attention for biochar modification. However, the time-consuming and tedious procedures limited their application. Wang et al. [107] found that ball milling could solve these above problems and have the potential for large-scale production of LDHs-modified biochars. The Mg/Al hydroxides-modified biochars (Mg/Al-BCs) were obtained by ball milling 1.5 g biochars with 0.897 g $Mg(OH)_2$ and 0.603 g $Al(OH)_3$ simultaneously at 300 rpm for 8 h. The results showed that $Mg(OH)_2$ and $Al(OH)_3$ loading on the biochars' surface were uniformly. Cui et al. [108] implied that ball milling could not only synthesize LDHs-modified biochars (BM-LDH-BCs) but also realized the exfoliation of LDHs at the same time demonstrated by the enlarged basal spacing and reduced crystallite size of LDHs.

Interestingly, Yang et al. [53,109] found that biomass (hickory wood) could be converted to biochars by one-step acidic or alkaline ball milling for 12 h at 300 rpm in ambient air without any external heat treatment. The strong oxidized H_2SO_4 used in the ball milling process facilitated the graphitization degree by decreasing the defects in the ordered structure and influencing sp^2 hybridization [53,109]. NaOH solution prompted graphitization by destroying and reconstructing micro-domains via sodium intercalation/deintercalation and relieving subsequent distortion stresses [53,109]. Both H_2SO_4 and NaOH solutions enhanced the formation of oxygen-containing functional groups.

3.3. Ball-Milled CNTs-Based Materials

CNTs possess amorphous carbons and one-dimensional structures with sealing at both ends [110]. Ball milling is capable of altering CNTs' surface properties. Graphite could be transformed into nanoarches or highly curled CNTs during a high-energy ball-milling process [111], whereas short open-ended CNTs could be prepared mechanically [112,113].

The length of single-walled carbon nanotubes (SWCNTs) became short without significant damage to the structures for the first 2 h of ball milling. And then, the SWCNTs' structure was destroyed and gradually transformed into multi-layered polyromantic carbon with prolonged ball milling to 50 h [65]. Soares et al. [31] indicated that there was an increase in the specific surface area of multi-walled carbon nanotubes (MWCNTs) and a decrease in particle sizes after ball milling for 240 min, resulting from the opening or breaking of the nanotubes. With ball milling treatment time going, the specific surface area gradually decreased owe to compaction and particle sizes increased because of agglomerates formation. Ball milling intensity also affect MWCNTs' structure. Mild intensity (260 rpm for 1–10 h) had almost no change on MWCNTs' structure, whereas high intensity (720 rpm for 1.3 h) transformed MWCNTs entirely into amorphous materials. Moderate ball milling intensity (370–510 rpm for 2 h) could generate open and short MWCNTs and yield a high yield of open tips with minimal damage to the tubular structure [64]. Solvents is another factor in CNTs' physicochemical property. Dry ball milling could quickly collapse MWCNTs, while wet ball milling with alcohol made MWCNTs short and open, resulting from the destroyed structure [114].

Ball milling is also adopted to synthesize CNTs-based composites. N-doped CNTs synthesized by ball milling MWCNTs with triazine/urea and then thermal decomposition incorporated N-functionalities onto the carbon surface in forms of quaternary nitrogen, pyrrolic, and pyridinic groups [115]. Côa et al. [116] prepared humic acid-coated MWCNTs (HA-MWCNTs) by a ball milling method to form a stable coating on the MWCNTs' surface with a short length. And the oxygen contents and defects at the graphitic structure increased with irregular surfaces and wide diameters. The obtained HA-MWCNTs had long-term dispersion stability in ultrapure water (>96 h). Moreover, Cu [117], Al [118], Fe_3O_4 [119], SnO_2, ZnO, and TiO_2 particles [120] were also introduced to CNTs' surfaces by a drying ball milling strategy. A combination of ball milling and hydrothermal method could develop a FeOx@CNTs nanocomposite by milling CNTs in a mixture solution of $FeCl_3 \cdot 6H_2O$ and KOH. And the obtained magnetic iron oxides (Fe_3O_4) were loaded on the sidewalls of CNTs through –OH, C–H, and C–O functional groups (Figure 4a) [66].
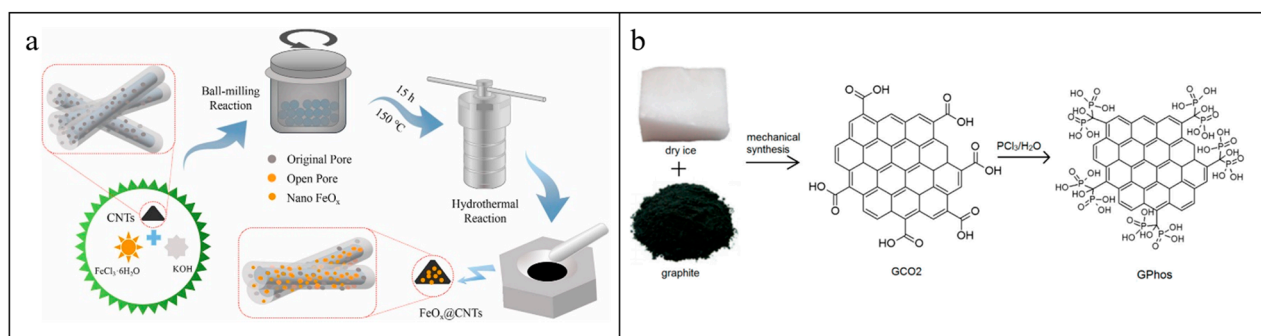
Figure 4. Schematic diagram of (**a**) FeOx@CNTs [66] and (**b**) PGO preparation [121]. (**a**) Reprinted from Chemosphere, 288, Cheng Z., Lyu H., Shen B., Tian J., Sun Y., Wu C., Removal of antimonite (Sb(III)) from aqueous solution using a magnetic iron-modified carbon nanotubes (CNTs) composite: Experimental observations and governing mechanisms, 132581, Copyright (2022), with permission from Elsevier. (**b**) Reprinted from Nanomaterials, 9, Olszewski R., Nadolska M., Lapinski M., Przesniak-Welenc M., Cieslik B.M., Zelechowska K., Solvent-free synthesis of phosphonic graphene derivative and its application in mercury ions adsorption, 485, Copyright (2019), with permission from MDPI.

3.4. Ball-Milled Graphene-Based Materials

Graphene is a two-dimensional atomic crystal composed of single-layer sp^2-hybrid carbon atoms with a honeycomb structure characterized by a huge specific surface area and rich π electron structure [122,123]. Ball milling is a simple and environmentally friendly strategy to exfoliate graphite, synthesize graphene and graphene-based materials, and pre-

pare graphene oxides. Few-layer functionalized graphene with a sole functional group [124] and edge-carboxylate graphene (ECG) [125] were obtained by means of dry ball milling graphite powders with milling balls. Chandran et al. [126] found that D-sorbitol could assist in the ball milling of graphite to graphene, and the polyhydric nature of D-sorbitol was able to insert and interact with layers via non-conventional OH–π and CH–π H-bonding. This was conducive to the shear force-assisted exfoliation and introduced edge functionalization to the obtained graphene. A novel holey graphene architecture (HGO) was synthesized by graphite exfoliation via jaggery assisted wet ball milling technique, hydrothermal treatment, and further calcination without employing any oxidizing agents for creating holes [127]. Graphene nanosheets/Al_2O_3 composites could also be prepared by milling Al_2O_3, graphite with ethanol. It was found that there was a positive relationship between ball milling speed (200–300 rpm) and layers of graphene nanosheets achieving the highest graphene conversion efficiency at a speed of 300 rpm [50]. ZrO_2 nanopowders dispersed on graphenes were obtained by a similar way of ball milling graphite with ZrO_2 in 1-methyl-2-pyrrolidinone solution. But no characteristic peak of graphene oxide was observed in the composites, suggesting a small oxidation degree of graphene [128]. Potassium perchlorate could be used as an oxidizing agent in a wet ball milling process to synthesize graphene oxide from graphite. Ball milling time contributed to the oxidation level of materials until 12 h, and then oxygen-containing functional groups, such as hydroxyl, carboxyl, and epoxyl, were presented on the samples [129].

Ball milling could also induce defects to graphene sheets derived from the stripping through shearing force and broadening of edges through compression force. And then, defects were changed to oxygen-containing functional groups due to the participation of O_2 from the atmosphere [32]. Olszewski et al. [121] indicated that ball milling graphite with CO_2 not only introduced oxygen-containing functional groups into the edges of graphite planes but also prevented the materials from uncontrollable destruction and remained the layered structure with lower defects compared to the one ball milling in air. This method eliminated the use of solvents without by-products and was conductive to converse carboxylic groups into un-hydrolyzed phosphonic groups by reacting with PCl_3 to obtain phosphonic graphene derivatives (PGO) (Figure 4b).

Furthermore, ball milling graphenes/graphenes oxide with modifiers is widely employed to prepare novel composites. N-functional groups [130], nickel-based metal–organic framework [131], Ti [132], Fe/Co/N [133], Mg/Ni [134], Si [135] and NiO [136] were introduced to graphenes by a ball milling route, while CuS [137], TiO_2 [138], SnO_2-MoO_2 [139], and indium tin oxides [140] were loaded on the surfaces of graphene oxides mechanically. Furthermore, ball milling graphene oxides in an Ar atmosphere was used to produce reduced graphene oxides by introducing defects and reducing oxygen functional groups [141]. A sulfidated ZVI/reduced graphene oxide composite was prepared by ball milling graphite oxide with ZVI and S under a N_2 atmosphere [142].

3.5. Ball-Milled ZVIs-Based Materials

In recent years, ZVIs have become popular in the water treatment industry with the advantages of high abundance, low cost, and environmental benignity [143]. However, the problem of the surface oxide layer caused by the oxidation of ZVIs at ambient conditions blocked their application. Ball milling ZVIs directly only flatted the particles trapped between the balls by compressive forces generated from the collision of balls and led to ZVIs disintegration, which resulted in small particles, rough surface, and large specific surface area (Figure 5) [144]. Adding reagents/modifiers in the ball milling ZVIs process could destroy or alter the surface iron oxide layer, which included formic acid [145], oxalic acid [146], boric acid [147], tannic acid [148], ethylenediaminetetraacetic acid [149], FeS [150], FeS_2 [151], MoS_2 [152], ferrous oxalate [153], Fe_3O_4 [34], FeS [150], FeS/Cu [154], $CaCO_3$ [155], S [156], lignosulfonate [157], L-cysteine [158], nitridation source (urea, melamine, and dimethylimidazole) [159], and coffee grounds [160]. For instance, oxalic acid modification altered the composition of the iron (hydro) oxide layer coated on

ZVIs mechanically and formed FeC_2O_4 on the surface [146]. Ball milling ZVIs with FeS not only decreased particle sizes and increased the specific surface area but also increased the crystallinity and exposure of ZVIs. A high ball milling speed contributed to a suitable passivation inhibition effect [150]. $CaCO_3$ used in the ZVIs ball milling process was in favor of stripping the original oxide layer, dispersing it in solution, and protecting the fresh ZVIs from forming an oxide layer [155].
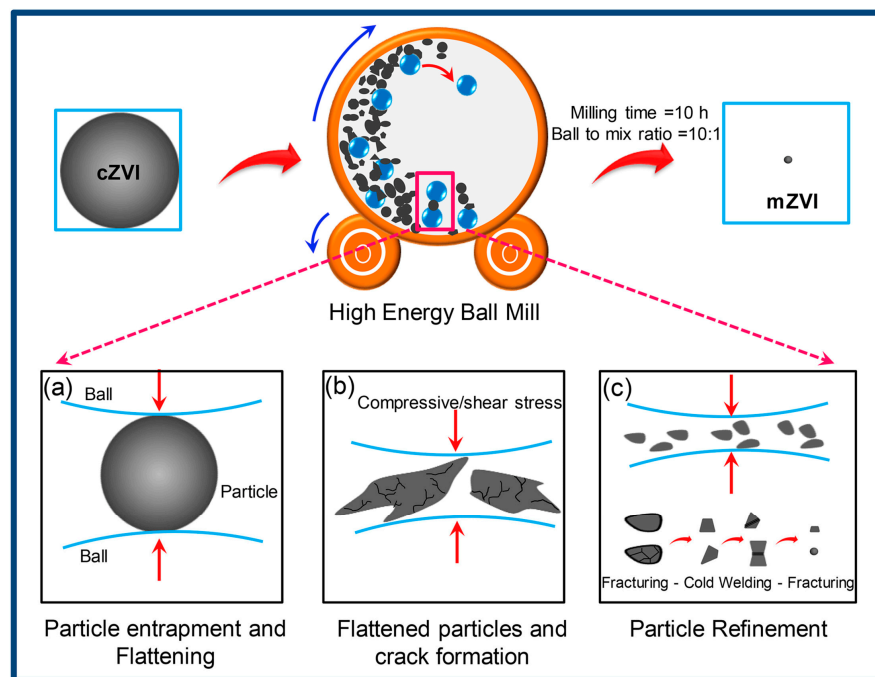

Figure 5. Mechanochemical synthesis of ZVIs [144]. Reprinted from Journal of Environment Management, 181, Ambika S., Devasena M., Nambi I.M., Synthesis, characterization and performance of high energy ball milled meso-scale zero valent iron in Fenton reaction, 847–855, Copyright (2016), with permission from Elsevier.

3.6. Ball-Milled ZVAls-Based Materials

ZVAls become one of the current research hotspots because of abundant reserves in the earth's crust [161]. As with ZVIs, the surface oxide layer of ZVAls also limits their application. Ethyl alcohol [162] and NaCl [163] were employed to pretreat the oxide layer of ZVAls via a ball milling method, while ball milling ZVAls with ACs/NaCl [164] and graphite/NaCl [51] were effective means of modifying ZVAls. Ethyl alcohol inhibited the cold welding of ZVAls and kinetic energy generated in a ball milling process. This promoted the fracture of ZVAls and led to the enlarged specific surface area, reduced particle sizes, and destroyed the oxide layer [162]. NaCl grains embedded in ZVAls by ball milling caused the destruction of the original dense oxide layer on the surface of ZVAl and resulted in a rough surface [163]. And then, ACs formed a thin layer of ZVAls to prevent agglomeration of the particles [164]. Graphite-modified ZVAls via a ball milling method could not only prevent agglomeration of ZVAls but also promote absorbability, electrical conductivity, and hydrophobicity of materials [51].

4. Application of Ball-Milled Adsorbents for Water Purification

4.1. Removal of Inorganic Pollutants

Table 1 lists the removal of inorganic pollutants by various ball-milled adsorbents. The enlarged specific surface area and oxygen-containing functional groups of ball-milled ACs are conducive to Cr(VI) removal. Wang et al. [8] indicated that the larger specific surface area of ZVIs-ACs facilitated the adsorption amount of Cr(VI) on the ZVI-ACs' surface. Fang et al. [9] presented that the adsorption capacity of Cr(VI) by ACs increased from

18.9–22.4 mg/g to 31.6–32.6 mg/g after ball milling due to the enriched carboxylic groups formed in the ball milling process via complexation effect. The adsorption isotherm-fitted Freundlich model indicated that it was multilayer adsorption, and the thermodynamic study implied that the Cr(VI) adsorption was endothermic and spontaneous.

The variation in physicochemical properties of biochars before and after ball milling gives rise to the change in the adsorption amount, equilibrium time, and adsorption mechanism of inorganic pollutants. Most reports showed that the adsorption amounts of inorganic pollutants by biochars-based materials increased after ball milling with a short equilibrium time (Table 1). The adsorption isotherm, in accordance with the Langmuir model, shows that the adsorption of pollutants on ball-milled materials is monolayer coverage with a similar energy of adsorption sites [165,166]. The alignment of adsorption kinetics with the pseudo-second-order model indicates that the ball milling brings numerous active sites to materials, and the adsorption kinetics stays in correlation with the availability of adsorption sites on the surface of adsorbents rather than adsorbate concentrations in bulk solution [121]. The best fit of the Redlich–Peterson and Elovich model on Ni(II) adsorption by the ball-milled biochars (BM-BCs) suggested that it was heterogeneous, involving multi-mechanism adsorption processes [86]. The increase in external and internal surface areas of BM-BCs exposed the graphitic structure and thus improved Ni(II) adsorption via strong cation–π interaction. An improvement in oxygen-containing functional groups after ball milling could both enhance the complexation effect and decrease the surface potential to enhance electrostatic interaction to improve Ni(II) adsorptive uptakes (Figure 6a). The adsorption selectivity experiment showed that the cations uptakes were arranged in the order Ni(II) (193 mmol/kg) > K(I) (14.8 mmol/kg) > Na(I) (1.57 mmol/kg) > Ca(II) (0.53 mmol/kg) > Mg(II) (0.015 mmol/kg), indicating BM-BCs had a high selection to Ni(II). This reason was that the small ionic radius of Ni(II) (0.069 nm) was beneficial for entering into the channels of BM-BCs, and other large cations were only adsorbed on the surface of BM-BCs. The process of Pb(II) by BM-BCs was chemical adsorption with endothermicity and spontaneousness [167]. The increase in oxygen-containing groups on BM-BCs favored Pb(II) adsorption at the low pH values assigned to the enhanced electrostatic attraction between deprotonated hydroxyl and carboxyl of BM-BCs and positive Pb(II). The addition of $NaNO_3$ and Na_2SO_4 suppressed Pb(II) captures by BM-BCs attributed to the competition of Na^+ for adsorption sites [167]. Li et al. [168] suggested that ball milling introduced more minerals, oxygen functional groups, and unsaturated carbon bonds to wheat straw-derived biochars, which improved Pb(II) adsorption by co-precipitation, π electronic interaction, and complexation with maximum adsorption capacity increasing from 73.50–164.23 mg/g to 103.99–210.90 mg/g, compared to raw biochars. Ball-milled nitrogenous bone biochars (BM-NBBCs) exposed more hydroxy, carboxyl, and aromatic esters, pyridinic-N, pyridonic-N, and phosphate groups and thus adsorbed Pb(II), Cd(II), and Cu(II), which was a spontaneous and endothermic process [169]. The adsorption mechanism included cation exchange with inorganic components, surface complexation via oxygen-containing and nitrogen-containing groups, dissolution–precipitation via phosphate groups, electrostatic interactions between positively charged heavy metals and negatively charged materials, and cation–π interaction via aromatic/graphitic carbon with π electrons (Figure 6b). The increase in $NaNO_3$ did not affect Pb(II) removal due to the major interaction of chemical precipitation and inner-surface complexation, while the increasing $NaNO_3$ concentration influenced Cd(II) and Cu(II) uptakes negatively due to the dominant mechanism of cation exchange and/or outer-surface complexation. Similarly, Li et al. [170] also showed that the addition of $NaNO_3$ was unfavorable for Hg(II) adsorption. Both the ball-milling potassium ferrate-activated biochars (BM-PBCs) [171] and the ball-milled biochar/iron oxide composites (BM-Fe-BCs) [85] could remove Cr(VI) in an acid solution. The coexisting Cl^-, SO_4^{2-}, and PO_4^{3-} affected Cr(VI) removal negatively due to competition adsorption sites, and this indicated that electrostatic interaction was important in Cr(VI) removal. Moreover, PO_4^{3-} had the largest inhibition, probably due

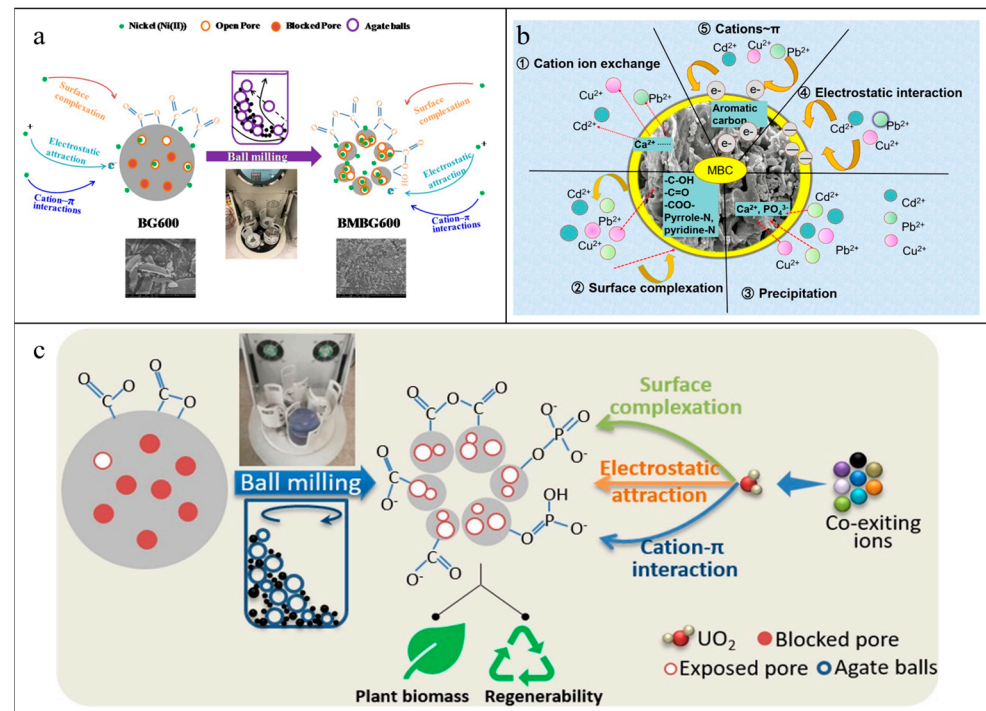to the formation of Fe-P compounds on the surface of BM-Fe-BCs, which blocked Cr(VI) adsorption [85].

Figure 6. Mechanism diagrams of governing mechanisms of (**a**) Ni(II) adsorption onto unmilled and milled biochars [86]; (**b**) Cd(II), Cu(II), and Pb(II) adsorption on BM-NBBCs [169]; (**c**) U(VI) uptake on PFBCs [89]. (**a**) Reprinted from Environmental Pollution, 233, Lyu H., Gao B., He F.; Zimmerman A.R., Ding C., Huang H., Tang J., Effects of ball milling on the physicochemical and sorptive properties of biochar: Experimental observations and governing mechanisms, 54–63, Copyright (2018), with permission from Elsevier. (**b**) Reprinted from Journal of Hazardous Materials, 387, Xiao J.; Hu R.; Chen G., Micro-nano-engineered nitrogenous bone biochar developed with a ball-milling technique for high-efficiency removal of aquatic Cd(II), Cu(II) and Pb(II), 121980, Copyright (2020), with permission from Elsevier. (**c**) Reprinted from Journal of Molecular Liquids, 303, Zhou Y., Xiao J., Hu R., Wang T., Shao X., Chen G., Chen L., Tian X., Engineered phosphorous-functionalized biochar with enhanced porosity using phytic acid-assisted ball milling for efficient and selective uptake of aquatic uranium, 112659, Copyright (2020), with permission from Elsevier.

The embedded functional groups in biochars facilitate inorganic pollutants' adsorptive removal. When CaO was embedded in the biochars, the adsorption capacity of phosphate was improved greatly, and the saturated adsorption amount reached 96.4–231 mg/g with an equilibration time of 6 h [81]. The disappearance of pore structure in the CaO-biochars and the appearance of flocculent precipitate ($Ca_5(PO_4)_3OH$(HAP)) on adsorbents' surface and pores confirmed that precipitate was the main adsorption mechanism. The embedded FeS could mitigate the oxidation-induced surface passivation of ZVIs to extend the use lifetime of BM-SnZVI@BC to 60 d aging in air with the saturated adsorption amount of 25.00–39.72 mg/g for phosphorus [106]. The main adsorption mechanism included precipitate ($Fe_5(PO_4)_4(OH)_3 \cdot 2H_2O$) produced between Fe and P, the formation of O–H–P hydrogen bonds, ligand exchange by phosphate ions replacing hydroxyl groups, and electrostatic attraction. The adsorption processes of phosphate by both CaO-BCs [81] and BM-SnZVI@BC [106] were spontaneous and endothermic, but the negative effects of coexisting anions on phosphate adsorption were different. The anions NO_3^- and Cl^- had an insignificant effect on phosphate adsorption by CaO-biochars, even in the case of high concentrations. The coexisting HCO_3^- and SO_4^{2-} affected phosphate uptakes on CaO-biochars negatively, resulting from the formation of insoluble or poorly soluble substances

between Ca^{2+} and HCO_3^-/SO_4^{2-} [81]. The inhibition of Cl^- on phosphate adsorption by BM-SnZVI@BC was weakened with increasing concertation of Cl^-. The anions NO_3^- unfavored phosphate adsorption on BM-SnZVI@BC due to the accelerated corrosion of BM-SnZVI@BC and formation of passivation layers. The co-existence of HCO_3^- disadvantaged phosphate uptakes by BM-SnZVI@BC since the competition for specific adsorption sites resulted from the structural similarities of HCO_3^- and $H_2PO_4^-$ and the HCO_3^- increased the solution pH value [106]. MgO-biochars not only had the ability to adsorb phosphate by electrostatic action and surface precipitation but also remove Ni(II) via van der Waals force, metal ion exchange, metal–π interaction, and surface functional group complexation [172]. The coexisting Cl^- and SO_4^{2-} promoted Ni(II) uptakes owing to the exposure of active groups of MgO-biochars caused by electrostatic interactions of anions. The co-existence of Mn(II) and Co(II) suppressed Ni(II) adsorption, resulting from competitive adsorption by occupying the active sites on MgO-biochars. The embeddedness of SiO_2 on biochars was able to remove Cu(II), Zn(II), and Pb(II) with an adsorption capacity of 27.55–34.60 mg/g within 60 min by means of electrostatic interaction [173]. The ball-milled Fe_3O_4-modified biochars (BM-Fe_3O_4-BC) presented larger removal rates to Pb(II) with a maximum adsorption capacity of 183.99–339.39 mg/g within 20 min [174]. The positive $\Delta H°$ and the negative $\Delta G°$ indicated it was an endothermic and spontaneous process. The presence of Na^+ and K^+ showed a slight influence on Pb(II) capture by BM-Fe_3O_4-BC because of their low charge density. Both vermiculite [99] and Mg/Al hydroxides [107] loading on biochars contributed to As(V) adsorption. The coexisting Cl^- and NO_3^- had negligible influence on As(V) removal by Mg/Al-BCs, while HCO_3^- facilitated As(V) adsorption onto Mg/Al-BCs due to the changed pH values of the solution [107]. The FeS_2-modified biochars (FeS_2-BCs) could remove Cr(VI) by electrostatic attraction and surface complexation, ion exchange, and complexation [100]. The loaded attapulgite [98], ZVIs [79], Fe/Mn oxides [175], and LDHs [108] on biochars benefited Cd(II) removal. The mechanism involved physical adsorption, precipitate, complexation, electrostatic interaction, ion exchange, Cd–π interaction, and chelation. The inhibiting effect of different valence metal ions on Cd(II) adsorption by the Fe/Mn oxide–biochar nanocomposites (Fe/Mn-BCs) was arranged in the order Al(III) > Ca(II) > Na(I). This was because Al(III) and Ca(II) were more potential to form inner-sphere complexes with Fe/Mn-BCs and Na^+ were more likely to form outer-sphere complexes with Fe/Mn-BCs [175]. The presence of NaCl, KCl, and KNO_3 did not affect Cd(II) removal by BM-LDH-BCs significantly. On the contrary, the effect of NH_4Cl and $CaCl_2$ had an inhibited influence on Cd(II) adsorption, due to the more attraction between NH_4^+/Ca^{2+} and active sites than Na(I)/K(I) [108].

Phosphorous-functionalized biochars (PFBCs) by ball milling biochars with phytic acid adsorbed U(VI) in 60 min with the saturated adsorption amount of 78.6–114.9 mg/g, while biochars and BM-BCs had the saturated adsorption amount of 23.2–43.3 mg/g and 73.4–100.5 mg/g, respectively [89]. The enhanced mechanisms for U(VI) uptakes were the coordination of U(VI) with O atoms of P=O induced by the filling of empty valence orbital of U(VI) with lone pairs of electrons of neutral P=O groups, complexation effect between U(VI) and exposed oxygen-containing functional groups, electrostatic attraction between deprotonated adsorption sites and positively charged U(VI) species and cation–π bonding of U(VI) with the π electron donor provided by the electronic structure of biochars (Figure 6c). The U(VI) adsorption of PFBCs was an exothermic and spontaneous course. The presence of Cs(I), Sr(II), Co(II), Cd(II), Cu(II), Ni(II), Mn(II), Mg(II), and Ca(II) inhibited U(VI) removal slightly, while Fe(III) and Al(III) suppressed U(VI) significantly. It was ascribed to more competition of Fe(III) and Al(III) for the coordination on the surface of PFBCs due to the higher valence and smaller ionic radius. Thiol-modified biochars had a saturated adsorption capacity of 270.60 ± 2.67–401.8 ± 2.27 mg/g for Hg(II), which was more than 1.6 times higher than BM-BCs. The adsorption mechanism was surface adsorption, electrostatic attraction, complexation, and ligand exchange [55].

The specific adsorption sites of grated functional groups to CNTs via a ball milling route benefit heavy metal removal. The saturated adsorption capacity of Cu(II) by HA-

MWCNTs was 68.5 ± 3.5 mg/g, which was approximately 2.5 times higher than the one by nitric acid oxidized MWCNTs. This indicated that the adsorption capacity was positively related to the oxygen content of materials. The oxygen functional groups (especially with respect to –C=O) of HA-MWCNTs contributed to the adsorption capacity of Cu(II) through chemical complexation [116]. The adsorption capacity of Cr(VI) by CeO_2 supported on CeO_2-CNTs (28.3 mg/g) was 1.5 and 1.8 times higher than that of ACs and ball-milled CNTs, respectively. All of the specific affinity between Ce and Cr(VI), the small size of CeO_2 particles, and uniform distribution on the surface of CNTs were conducted to enhance Cr(VI) adsorptive removal [176]. Cheng et al. [66] reported that the Sb(III) adsorption capacity by FeOx@CNTs was much higher than that by CNTs, and the best-fitted Redlich–Peterson model indicated that it was a mixed removal process dominated by chemical reactions. The weak peak intensity of –OH and movement of the Fe–O peak from 575 cm^{-1} to 587 cm^{-1} in the FTIR spectrum after Sb(III) adsorption suggested the involvement of –OH and Fe–O in the removal of Sb(III). The formation of $FeO–H_2SbO_3$, $Fe–Sb(OH)_2$, and Fe–O–Sb on the surface of FeOx@CNTs further proved that complexation played a primary role in Sb(III) adsorption. The coexisting CO_3^{2-} (10 mg/L) facilitated Sb(III) adsorption slightly. However, the presence of Cl^- and PO_4^{2-} (1–10 mg/L) had an almost negligible effect on Sb(III) adsorption due to the electrostatic repulsion between the above anions and FeOx@CNTs. Additionally, excessively high ball milling speed caused the destruction of FeOx@CNTs' molecular structure, resulting in a decrease in Sb(III) removal, whereas the ball-milling time did not affect Sb(III) adsorption significantly.

The oxygen functional groups of graphene are in favor of inorganic pollutants' adsorptive removal. It showed that the saturated adsorption of the amounts of U(VI) by ball-milled graphene sheets was 71.93 mg/g at pH = 4.5 within 2 h, and the oxygen-containing functional groups were responsible for U(VI) captures [32]. The acidic solution (pH = 1) was beneficial to Cr(VI) removal by HGO. The FTIR spectrum of Cr(VI) adsorption by HGO before and after adsorption suggested that the interaction of Cr(VI) with the epoxy and –OH proved by the reduction in the intensity of peak at 1041 cm^{-1} and 1115 cm^{-1} corresponding to epoxy and C–OH binding. The peaks shifted from 1594 cm^{-1} to 1620 cm^{-1}, associating with aromatic C=C stretching frequency, indicating some sort of interaction between Cr species and the aromatic π network [127]. Olszewski et al. [121] presented that the adsorptive data of Hg(II) by the PGO-fitted Langmuir model and the maximum adsorption capacity were 82.2 mg/g through the interaction between Hg(II) and phosphonic groups. The presence of Cd(II) and Ni(II) did not affect Hg(II) adsorption, resulting from the enhanced interaction between phosphonic acid (soft base) and Hg(II) (soft acid) and the fast adsorption rate of Hg(II).

An improvement in specific surface area and pore volumes of ball-milled ZVIs composites and ball-milled ZVAls composites contributed to As(III) [151] and Cr(VI) removal [161,177]. The high concentration of Cl^- (0.1 mM) and low pH value were conducive to As(III) removal by FeS_2-ZVIs due to the corrosion of ZVIs [151]. The presence of Mg(II), Ca(II), Cl^-, SO_4^{2-}, and NO_3^- was not sensitive to Cr(VI) removal by $ZVAls/NiFe_2O_4$ due to the outer-sphere adsorption between the above anions and surface. The high concentration of CO_3^{2-} increased the pH values to alkaline conditions and affected Cr(VI) adsorption negatively due to the reduction in Cr(VI) to Cr(III) and precipitation on the surface to further inhibit adsorption as well as the enhanced electrostatic repulsion. HA inhibited Cr(VI) adsorption attributed to the complexation between HA and Cr(VI), which enhanced the electrostatic repulsion between Cr(VI) and $ZVAl/NiFe_2O_4$ [161]. Wang et al. [34] found that Cr(VI) was completely removed by $ZVAl/Fe_3O_4$ within 30 min, while the removal rate was not achieved at 10% by ZVAls and Fe_3O_4 at a dose of 3 g/L. The maximum adsorption capacity of Cr(VI) by $ZVAl/Fe_3O_4$ reached 8.10 mg/g, which was related to the ball milling parameters, such as the weight ratio of $ZVAl/Fe_3O_4$, milling speed, and milling time. Furthermore, the broken surface oxide layer and exposure of ZVls were in favor of Cr(VI) removal by lignosulfonate-modified zero-valent irons (LS-ZVIs) [157]. The presence of coexisted cationic Mg(II) and Ca(II) facilitated the initial removal rate of

Cr(VI) by LS-ZVIs because of the neutralization of LS-ZVIs' surface charges caused by the adsorption of cations, whereas the coexisting NO_3^-, Cl^-, and SO_4^{2-} inhibited initial removal rate of Cr(VI). Furthermore, the more inhibiting effect was caused by higher NO_3^- concentration (5–20 mM) assigned to competition for electrons between NO_3^- and Cr(VI) and the enhanced passivation of LS-ZVIs surface caused by NO_3^-. However, Zhao et al. [156] suggested that iron (oxyhydr) oxides were the primary adsorption sites for As(III) removal, and the increase in S reduced ZVIs contents, thus leading to decreasing removal rates of As(III). Ball milling ZVIs with coffee grounds (CG) introduced abundant carboxylic acid and some polyphenolic substances from caffeine and tannins to the surface of obtained materials, which improved Cr(VI) adsorption via the complexation interaction of CG–COOH···$HCrO_4^-$ [160].

Table 1. Ball-milled adsorbents' characterization and their application for inorganic pollutants adsorptive removal.

Materials	Ball Milling Treatment	Material Characterization	Pollutants	Experimental Condition	Isotherm Model	Adsorption Experiment Adsorption Capacity	Kinetic Model	Equilibrium Time	Adsorption Mechanism	Ref.
Ball-milled ACs-based materials										
ZVIs-ACs	P, BM: ACs (300 mg) +ZVIs (5.6 mg), ZrO$_2$ balls (Φ = 6 and 10 mm, MR = 4:1), RS = 300 rpm, MT = 30 min, air atmosphere	S = 16.9 m^2/g, Fe = 69.4%, C = 27.3%, O = 2.9%, P = 0.4%	Cr(VI)	T = 25 $\pm$ 2 °C, pH = 3.93	Langmuir model	14.35 mg/g [a]	PSO	2 h	Pore filling	[8]
HSACs	P, BM: ACs (10 g), steel balls (Φ = 5 mm), RS = 300 rpm, MT = 60 min	S = 929 m^2/g, APS = 4 μm, D = 15.3 Å, AFGs = 1.84 mmol/g, carboxyl = 0.97 mmol/g, phenolic, hydroxyl, and lactols = 0.87 mmol/g, C = 91.24%, N = 0.93%, O = 6.86%, S = 0.97%, zeta potential pH = 2–10$\approx$−22.5~−37.5 mV ACs: S = 846 m^2/g, APS = 20 μm, D = 19.0 Å, AFGs = 1.31 mmol/g, carboxyl = 0.31 mmol/g, phenolic, hydroxyl, lactols = 1.00 mmol/g, zeta potential (pH = 2–10) $\approx$−15~−23 mV	Cr(VI)	T = 295–313 K, pH = 6	Freundlich model	3.843–5.523 (mg/g)/(mg/L)$^{1/n}$ [b] ACs: 0.002–0.441 (mg/g)/(mg/L)$^{1/n}$ [b]	PSO	2 h	Complexation	[9]

<p align="center">Table 1. *Cont.*</p>

Materials	Ball Milling Treatment	Material Characterization	Pollutants	Experimental Condition	Isotherm Model	Adsorption Experiment Adsorption Capacity	Kinetic Model	Equilibrium Time	Adsorption Mechanism	Ref.
Ball-milled biochar-based materials										
BM-BCs	P, BM: biochars (1.8 g), agate balls (Φ = 6 mm, 180 g), RS = 300 rpm; MT = 3–24, TA = 0.5 h, air atmosphere	S = 364 m^2/g, V = 0.125 cm^3/g, D = 3.4 nm, hydrodynamic radius = 140 nm, TAG = 2.5 mmol/g, carboxyl = 1.1 mmol/g, lactols groups = 0.5 mmol/g; phenolic hydroxyl = 0.9 mmol/g, pH$_{pzc}$ < 1.6 Biochars: S = 359 m^2/g, V = 0.009 cm^3/g, D = 3.6 nm, grain size = 0.5–1 mm; TAG = 0.8 mmol/g, carboxyl = 0.5 mmol/g, lactols groups = 0 mmol/g, phenolic hydroxyl = 0.3 mmol/g, pH$_{pzc}$ ≈ 4.0	Ni(II)	T = 20 ± 2 °C, pH = 6.0	Redlich–Peterson model	1949 mmol/kg [a] Biochars: 211 mmol/kg [a]	Elovich mode	24 h Biochars: 30 h	Physical adsorption, electrostatic interaction, complexation	[86]
BM-BCs	BM: biochars (10 g), ZrO$_2$ balls, RS = 1600 rpm, MT = 60 s, T = 30	S = 74.39 m^2/g, V = 0.1540 cm^3/g, D = 8.3741 nm, C = 54.36%, N = 2.80%, O = 30.65%, pH$_{pzc}$ = 2.3 Biochars: S = 46.20 m^2/g, V = 0.1274 cm^3/g, D = 10.9337 nm, C = 63.22%, N = 3.19%, O = 23.94%	Pb(II)	T = 298–308 K	Langmuir model	163.63–170.09 mg/g [a]	PSO	60 min	-	[167]

Table 1. *Cont.*

Materials	Ball Milling Treatment	Material Characterization	Pollutants	Experimental Condition	Isotherm Model	Adsorption Experiment		Equilibrium Time	Adsorption Mechanism	Ref.
						Adsorption Capacity	Kinetic Model			
BM-BCs	V, BM: biochars (150 g), ZrO$_2$ balls (Φ = 6–10 mm, 1500 g), MT = 20 min	S = 53.82 $\pm$ 5.82–217.03 $\pm$ 4.36 m^2/g, V = 0.030 $\pm$ 0.006–0.113 $\pm$ 0.005 cm^3/g, V$_{micro}$ = 0.013 $\pm$ 0.002–0.027 $\pm$ 0.005 cm^3/g, D = 7.882 $\pm$ 1.797–13.04 $\pm$ 3.427 nm, carboxyl = 0.34 $\pm$ 0.01–0.36 $\pm$ 0.02 mmol/g, lactones = 0.16 $\pm$ 0.02–0.23 $\pm$ 0.02 mmol/g, phenolic hydroxyl = 0.12 $\pm$ 0.02–0.26 $\pm$ 0.03 mmol/g, OFGs = 0.62 $\pm$ 0.05–0.84 $\pm$ 0.03, CEC = 6.44 $\pm$ 0.92–15.07 $\pm$ 0.89 cmol/kg, pH = 9.31 $\pm$ 0.10–9.67 $\pm$ 0.11 Biochars: S = 14.37 $\pm$ 0.75–198.11 $\pm$ 2.61 m^2/g, V = 0.010 $\pm$ 0.001–0.094 $\pm$ 0.002 cm^3/g, V$_{micro}$ = 0.009 $\pm$ 0.001–0.009 $\pm$ 0.002 cm^3/g, D = 4.708 $\pm$ 0.252–6.072 $\pm$ 0.535 nm, carboxyl = 0.20 $\pm$ 0.03–0.24 $\pm$ 0.02 mmol/g, lactones = 0.09 $\pm$ 0.02–0.15 $\pm$ 0.01 mmol/g,	Pb(II)	T = 25 °C, pH = 5 $\pm$ 0.05	Langmuir model	103.99–210.90 mg/g [a] Biochars: 73.50–164.23 mg/g [a]	PSO	Equilibrium time shortened Biochars: 8–16 h	Co-precipitation, π electronic interactions, and complexation	[168]

Materials	Ball Milling Treatment	Material Characterization	Pollutants	Experimental Condition	Isotherm Model	Adsorption Experiment Adsorption Capacity	Kinetic Model	Equilibrium Time	Adsorption Mechanism	Ref.
		phenolic hydroxyl = 0.04 ± 0.01–0.18 ± 0.03 mmol/g, OFGs = 0.33 ± 0.01–0.57 ± 0.02 mmol/g, CEC = 6.27 ± 0.87–14.60 ± 1.21 cmol/kg, pH = 10.03 ± 0.14–10.28 ± 0.16								
BM-BCs	V, BM: biochars (8 g), ZrO$_2$ balls (Φ = 6–10 mm, 800 g), MT = 5 min	S = 130.14 ± 3.48 m^2/g, V = $(22.49 \pm 4.12) \times 10^{-3}$ cm^3/g, PS$_{10}$ = 1.30 ± 0.02 μm, PS$_{50}$ = 4.32 ± 0.06 μm, PS$_{90}$ = 14.20 ± 0.99 μm, H/C = 0.22 ± 0.00, O/C = 0.06 ± 0.00, CEC = 3.25 ± 0.05 mmol/g, AFGs = 0.57 ± 0.02 mmol/g, pH$_{pzc}$ = 9.77 ± 0.02. Biochars: S = 6.89 ± 1.28 m^2/g; V = $(7.04 \pm 2.25) \times 10^{-3}$ cm^3/g; PS$_{10}$ = 14.65 ± 0.92 μm, PS$_{50}$ = 71.20 ± 4.38 μm, PS$_{90}$ = 256.00 ± 36.77 μm, H/C = 0.19 ± 0.00, O/C = 0.04 ± 0.00, CEC = 3.31 ± 0.06 mmol/g, AFGs = 0.36 ± 0.01 mmol/g, pH$_{pzc}$ = 9.87 ± 0.01	Pb(II)	T = 25 °C, pH = 5.0	-	100.00 ± 0.00–134.68 ± 0.95 mg/g [c] Biochars: 99.45 ± 0.49–119.55 ± 0.64 mg/g [c]	-	-	Ion exchange, precipitation, and complexation	[178]

Table 1. *Cont.*

Materials	Ball Milling Treatment	Material Characterization	Pollutants	Experimental Condition	Isotherm Model	Adsorption Experiment Adsorption Capacity	Kinetic Model	Equilibrium Time	Adsorption Mechanism	Ref.
BM-NBBCs	BM: biochars (3.30 g) + DW(60 g), agate spheres, RS = 300 rpm, MT= 12 h, TA = 3 h	S = 35.49–313.09 m²/g, S_{micro} = 0–193.89 m²/g, $S_{external}$ = 35.49–119.20 m²/g, V = 0.1635–0.4538 cm³/g, D = 6.46–11.74 nm, pH_{pzc} = −2.0–3.1 Biochars: S = 2.76–52.78 m²/g, S_{micro} = 0–24.32 m²/g, $S_{external}$ = 2.76–28.46 m²/g, V = 0.0175–0.0975 cm³/g, D = 8.22–14.48 nm	Cd(II)	T = 298 K, pH = 5.0	Langmuir model	66.33–165.77 mg/g [a] Biochars: 31.12–75.15 mg/g [a]	PSO	200 min	Surface complexation, cation exchange, precipitation, electrostatic attraction, and cation–π interaction	[169]
			Cu(II)			159.27–287.58 mg/g [a] Biochars: 86.35–163.80 mg/g [a]		200 min		
			Pb(II)			339.34–558.88 mg/g [a] Biochars: 209.35–389.51 mg/g [a]		90 min		
BM-MBC	P, BM: MBC (1 g), agate balls (Φ = 5 mm, 100 g), MT = 12 h, TA = 20 min, RP = 10 min	S = 296.3 m²/g, V = 0.091 cm³/g, C = 47.98%, H = 0.88%, O = 27.89%, N = 0.53%, Fe = 12.32%, Na = 0.13%, Mg = 0.61%, Si = 0.13%, Ca = 2.13%, P = 0.12%, K = 0.88%, pH_{zpc} = 4.43, MS = 15.39 emu/g Magnetic biochars: S = 198.6 m²/g, V = 0.006 cm³/g, C = 57.82%, H = 2.48%, O = 21.98%, N = 0.87%, Fe = 1.25%, Na = 0.12%, Mg = 0.58%, Si = 0.11%, Ca = 2.10%, P = 0.11%, K = 0.81%, MS = 10.76 emu/g	Hg(II)	T = 24 ± 2 °C	Langmuir model	127.4 mg/g [a]	PSO	12 h	Electrostatic interactions, Hg–π interaction, and surface complexation	[170]

Table 1. *Cont.*

Materials	Ball Milling Treatment	Material Characterization	Pollutants	Experimental Condition	Isotherm Model	Adsorption Experiment		Equilibrium Time	Adsorption Mechanism	Ref.
						Adsorption Capacity	Kinetic Model			
BM-PBCs	P, BM: potassium ferrate-activated biochars, agate balls (MR of large, medium, and small = 2:18:15), RS = 300 rpm, MT = 12 h	S = 284.17–282.47 m^2/g, D = 11.62–12.10 nm, pH_{pzc} = 3.2–4.9, MS = 18.94–20.33 emu/g	Cr(VI)	T = 15, 25, 35 °C, pH = 2	Langmuir model	75.65–117.49 mg/g [a]	PSO	80–150 min	Ion exchange, pore filling, electrostatic attraction, precipitation, and surface complexation	[171]
BM-Fe-BCs	P, BM: biochar/iron oxide composites, RS = 500 rpm, MT = 4 h	S = 241 m^2/g. Biochar/iron oxide composites: S = 199 m^2/g	Cr(VI)	T = 22 ± 0.5 °C, pH = 5	Langmuir model	48.1 mg/g [a]	Elovich mode	200 min	Electrostatic interaction	[85]
CaO-biochars	BM: eggshell and rice straw powder (MR = 1:4–2:1), ZrO_2 balls (Φ = 0.8 cm, 60 g), MT = 30 min, pyrolysis (800 °C for 2 h)	S = 8.30–25.8 m^2/g, V = 0.0273–0.0467 cm^3/g; D = 6.70–13.1 nm, Ca = 19.5–42.2%, C = 4.32–16.7%, O = 15.8–25.4%, H = 1.68–2.42% Biochars: S = 7.87 m^2/g, V = 0.0126 cm^3/g, D = 6.40 nm, Ca = 1.00%, C = 46.6%, O = 7.59%, H = 1.90%	Phosphate	T = 298 K, pH = 7	Langmuir model	96.4–231 mg/g [a] Biochars: 5.58 mg/g [a]	PSO Biochars: PFO.	6 h Biochars: 6 h	Precipitate	[81]

Table 1. *Cont.*

Materials	Ball Milling Treatment	Material Characterization	Pollutants	Experimental Condition	Isotherm Model	Adsorption Experiment Adsorption Capacity	Kinetic Model	Equilibrium Time	Adsorption Mechanism	Ref.
MgO-biochars	BM: biochars (1.0 g) + MgO (0.5 g), agate balls (Φ = 6 and 8 mm, 75 g), RS = 500 rpm, MT = 12 h	S = 10.141–49.324 m^2/g, V = 3.809–3.820 cm^3/g, D = 0.033–0.091 nm, C = 33.72–34.43%, H = 1.71–2.37%, O = 11.33–14.05, N = 1.30–1.89, H/C = 0.05–0.07, O/C = 0.34–0.41, (O + N)/C = 0.38–0.45, pH_{pzc} = 2.14–2.19 Biochars: S = 2.088–2.458 m^2/g, V = 3.820–3.836 cm^3/g, D = 0.001–0.002 nm, C = 42.58–59.79%, H = 0.88–2.97%, O = 1.63–10.82%, N = 1.82–2.16%, H/C = 0.01–0.05, O/C = 0.03–0.19, (O + N)/C = 0.06–0.23	Ni(II)	T = 298, 308, 318 K, pH = 6.0	Freundlich model	99.3 $\pm$ 5.4–239.6 $\pm$ 3.7 $(mg/g)/(mg/L)^{1/n}$ [b]	PSO	5–20 h	Van der Waals force, metal ion exchange, metal–π interaction, surface functional group complexation	[172]
MgO-biochars	BM: biochars (1.8 g) + MgO (10–50% wt/wt), RS = 500 rpm, MT = 12 h, TA = 3 h	S = 140 m^2/g, V = 0.100 cm^3/g, C = 47.71%, O = 29.77%, Mg = 21.8%, Si = 0.72% Biochars: S = 249.7 m^2/g, V = 0.112 m^3/g BM-BC: S = 310.7 m^2/g, V = 0.140 m^3/g	Phosphate	T = 25 $\pm$ 2 °C	-	2–12 mg/g [c] Biochars and BM-BCs < 0	-	-	Electrostatic action and surface precipitation	[95]

Table 1. *Cont.*

Materials	Ball Milling Treatment	Material Characterization	Pollutants	Experimental Condition	Isotherm Model	Adsorption Experiment Adsorption Capacity	Kinetic Model	Equilibrium Time	Adsorption Mechanism	Ref.
SiO$_2$@C	BM: biochars+ SiO$_2$	S = 262.39 m^2/g, V = 0.1480 cm^3/g D = 2.2527 nm, SiO$_2$ = 27.02%, C = 72.98%, zeta potential = −71 mV	Cu(II) / Pb(II) / Zn (II)	pH = 6	-	34.60 mg/g [d] / 23.47 mg/g [d] / 27.55 mg/g [d]	PSO	60 min	Electrostatic interaction	[173]
Ball-milled biochar–vermiculite nanocomposites	P, BM: biochars (1.8 g)+ expanded vermiculite (MR = 1:9, 1:4, 3:7 and 2:3), beads (Φ = 6 mm, 180 g), RS = 300 rpm, MT = 12 h, TA = 0.5 h	S = 16.078 m^2/g, V = 0.047 cm^3/g, D = 12.929 nm Biochars: S = 214.622 m^2/g, V = 0.009 cm^3/g, D = 1.140 nm	As(V)	T = 25 ± 0.5 °C, pH = 6	Langmuir model	20.1 mg/g [a]	PSO	36 h	Ion exchange and electrostatic attraction	[99]
Biochar–attapulgite nanocomposites	P, BM: biochars (1 g)+ attapulgite (0.5–2 g), agate balls (Φ = 2–5 mm, 150–300 g), RS = 550 rpm, MT = 5 h, TA = 0.5 h	S = 16.1–17.12 m^2/g, V = 0.0536–0.0613 cm^3/g, D = 13.32–14.32 nm, C = 24.58–45.79%, N = 0.30–0.41%, H = 2.32–3.22%. Biochars: S = 4.46 m^2/g, V = 0.0056 cm^3/g, D = 5.04 nm, C = 65.54%, N = 0.88%, H = 4.79%, C/O = 2.88	Cd(II)	T = 25 °C	Freundlich model	5.9916–17.8571 L/g [b] Biochars: 2.1513 L/g [b]	PSO	4 h	Silicate precipitate, acid-oxygenated groups complexation, and electrostatic interaction	[98]
FeS$_2$-BCs	P, BM: biochars (0.6 g) + FeS$_2$ (2 g), ZrO$_2$ balls (Φ = 3, 5, 15 mm, 200 g, MR = 3:5:2), RS = 400 rpm, MT = 24 h, AT = 6 h, purged with N$_2$ (> 99%) for 30 min	S = 82.9 m^2/g, V = 0.021 cm^3/g, D = 3.53 nm, C = 13.7%, H = 1.74%, O = 38.1%, N = 0.06%, S = 24.7%, Fe = 21.7%, H/C = 0.13, O/C = 2.78, (N + O)/C = 2.79, pH$_{pzc}$ = 6.4	Cr(VI)	pH = 4.7	Langmuir model	134 ± 1.32 mg/g [a]	PSO	-	Electrostatic attraction and surface complexation	[100]

Table 1. *Cont.*

Materials	Ball Milling Treatment	Material Characterization	Pollutants	Experimental Condition	Isotherm Model	Adsorption Experiment Adsorption Capacity	Kinetic Model	Equilibrium Time	Adsorption Mechanism	Ref.
		Biochars: S = 455 m^2/g, V = 0.015 cm^3/g, D = 1.65 nm, C = 85.7%, H = 1.90%, O = 12.2%, N = 0.20%, H/C = 0.022, O/C = 0.14, (N + O)/C = 0.15 BM-BCs: S = 568 m^2/g, V = 0.141 cm^3/g, D = 2.33 nm, C = 78.3%, H = 2.41%, O = 19.1%, N = 0.19%, H/C = 0.031, O/C = 0.24, (N + O)/C = 0.25								
ZVIs-BCs	BM: cotton husk + ZVIs, pyrolysis (800 °C for 1 h), stainless balls (Φ = 5 mm, 40 g), RS = 350 rpm, MT = 2.5 h, TA = 10 min	S = 378.66 m^2/g, V = 0.1704 cm^3/g, D = 1.7996 nm, H/C = 0.01, O/C = 0.09; (O + N)/C = 0.11, Fe = 8.99% Biochars: S = 4.32 m^2/g, V = 0.008217 cm^3/g, D = 7.6157 nm, H/C = 0.01, O/C = 0.07, (O + N)/C = 0.08, Fe =0.04%	Cd(II)	T = 298 K	Langmuir model	96.40 mg/g [a] Biochars: 84.19 mg/g [a]	PSO	4 h	Physical adsorption, electrostatic attraction, and complexation	[79]
BM-Fe$_3$O$_4$-BC	P, BM: biochars + Fe$_3$O$_4$ (MS = 1:100), agate balls (Φ = 6, 10, and 15 mm), MM =1:2, RS= 500 rpm, MT = 12 h, TA = 3 h	S = 10.1178 m^2/g, V = 0.0015 cm^3/g, pH$_{pzc}$ = 5.3, MS = 5.29 emu/g. Biochars: S = 82.10 m^2/g	Pb(II)	T = 10–50 °C	Langmuir model	183.99–339.39 mg/g [a]	Avrami fractional-order model	20 min	Electrostatic attraction, precipitation, complexation, cation exchange, and co-precipitation.	[174]

Table 1. *Cont.*

Materials	Ball Milling Treatment	Material Characterization	Pollutants	Experimental Condition	Isotherm Model	Adsorption Experiment Adsorption Capacity	Kinetic Model	Equilibrium Time	Adsorption Mechanism	Ref.
BM-NaOH-BC	BM: NaOH-modified biochars (2 g) + Fe_3O_4 (2 g), agate balls (Φ = 6 mm, 200 g), RS = 500 rpm, MT = 12 h, TA = 3 h	S = 148.41 m^2/g, V = 0.178 cm^3/g, D = 1.985 nm, pH_{pzc} = 10.52, MS = 37.09 emu/g NaOH-modified biochars: S = 288.91 m^2/g, V = 0.315 cm^3/g, D = 3.061 nm	Cd(II)	T = 25 °C, pH = 7.0	Freundlich model	183.59 mg/g [a] NaOH-modified biochars: 101.51 mg/g [a]	PSO	60 min NaOH-modified biochars: 120 min	Pore adsorption, precipitation, ion exchange, complexation, and Cd–π interaction	[179]
BM-SnZVI@BC	P, BM: biochars (3 g) + S (1 g) + Fe (1 g), ZrO_2 balls (Φ = 5, 10, 15 mm, 150 g, MR = 1:1:1), RS = 400 rpm, MT = 12 h, TA = 30 min, N_2 purging for 20 min	pH_{pzc} = 9.49, MS = 11.91 emu/g	Phosphorus	T = 298, 308, 318 K, pH ≈ 6	Langmuir model	25.00–39.72 mg/g [a]	PFO	240 min	Electrostatic attraction, surface precipitation, hydrogen bonding, and ligand effects	[106]
BM-FeS@NBCs	BM: biochars (1 g) + $NH_3 \cdot H_2O$ (15 g), agate balls (Φ = 15, 10, 6 mm, 45 g, MR = 2:20:22), RS = 300 rpm, MT = 12 h, AT = 3 h, N_2 purging for 30 min BM: N-biochars (1 g) + FeS (0.5 g), agate balls (Φ = 15, 10, 6 mm, 27 g, MR = 1:10:11), RS = 300 rpm, MT = 12 h, AT = 3 h, N_2 purging for 30 min	pH_{pzc} = 3.9	Cr(VI)	T = 15–25 °C	Langmuir model	149.38–194.69 mg/g [a]	Avrami fractional-order model	250 min	Electrostatic attraction, ion exchange, and complexation	[10]

Table 1. *Cont.*

Materials	Ball Milling Treatment	Material Characterization	Pollutants	Experimental Condition	Isotherm Model	Adsorption Experiment Adsorption Capacity	Kinetic Model	Equilibrium Time	Adsorption Mechanism	Ref.
BM-LDH-BCs	P, BM: biochars + LDHs + water (MR = 10:1:1), agate balls, RS = 500 rpm, MT = 4 h, TA = 5 min	$S = 226$ m^2/g, $V = 0.140$ cm^3/g, $D = 3.51$ nm, zeta potential (pH = 5.5) $= -17.5$ mV Biochars: $S = 122$ m^2/g, $V = 0.108$ cm^3/g, $D = 3.86$ nm, zeta potential (pH = 5.5) $= -15.7$ mV BM-BCs $S = 246$ m^2/g, $V = 0.101$ cm^3/g, $D = 3.52$ nm, zeta potential (pH = 5.5) $= -26.3$ mV	Cd(II)	$T = 25\ °C$, pH = 5.5	Freundlich model	41.0 (mg/g)/(mg/L)$^{1/n}$ [b] Biochars: 7.82 (mg/g)/(mg/L)$^{1/n}$ [b] BM-BCs 26.9 (mg/g)/(mg/L)$^{1/n}$ [b]	PFO	8 h	Surface complexation, chelation, precipitation, and physical adsorption	[108]
Mg/Al-BCs	BM: biochars (1.5 g) + Mg(OH)$_2$ (0.897 g) + Al(OH)$_3$ (0.603 g), agate balls (300 g), RS = 300 rpm, MT = 8 h, TA = 0.5 h	$S = 17.577$ m^2/g, $V = 0.0885$ cm^3/g, $D = 12.56$ nm, C = 12.51%, H = 2.79%, N = 1.54%, pH$_{pzc}$ = 4.56 Biochars: $S = 14.108$ m^2/g, $V = 0.0383$ cm^3/g, $D = 14.26$ nm, C = 25.87%, H = 1.23%, N = 3.51%, pH$_{pzc}$ = 3.42 BM-BCs $S = 16.199$ m^2/g, $V = 0.0749$ cm^3/g, $D = 12.74$ nm, C = 24.17%, H = 1.69%, N = 3.27%, pH$_{pzc}$ = 3.66	As(V)	$T = 25–35\ °C$, pH = 7.0	Freundlich model	TM: 24.49 mg/g [c] Biochars: 0.48 mg/g [c] BM-BCs 6.73 mg/g [c]	PSO	20 h	Precipitation, ion exchange, surface complexation, and electrostatic interaction.	[107]

Table 1. *Cont.*

Materials	Ball Milling Treatment	Material Characterization	Pollutants	Experimental Condition	Isotherm Model	Adsorption Experiment		Equilibrium Time	Adsorption Mechanism	Ref.
						Adsorption Capacity	Kinetic Model			
Fe/Mn-BCs	P, BM: biochars, agate balls, MM = 1:100, RS = 300 rpm, MT = 6 h	S = 226.50–331.5 m^2/g, V_{meso} = 0.32–0.36 cm^3/g, D = 4.16–5.21 nm, pH_{pzc} = 1.73–3.06 Biochars: S = 14.02–30.35 m^2/g, V_{micro} = 0.003–0.006 cm^3/g, V_{meso} = 0.006–0.03 cm^3/g, D = 6.49–7.49 nm	Cd(II)	T = 298 K, pH = 5	Langmuir model	65.3–100.9 mg/g [a] Biochars: 12.9–20.9 mg/g [a]	PSO Before: PFO	3 h Biochar: 4 h	Surface complexation, cation exchange, Cd–π interaction, precipitation, and electrostatic attraction.	[175]
BM-PBCs	P, BM: biochars (3.3 g) and phytic acid (0–50% wt% solution), agate balls (Φ = 6 mm, 330 g), RS = 12 h, MT = 12 h, TA = 3 h, RP = 30 min	S = 66–285 m^2/g, S_{micro} = 36–205 m^2/g; V = 0.089–0.273 cm^3/g, V_{micro} = 0.017–0.092 cm^3/g, APS = 307–615 nm, C = 73.5–80.0%, O = 15.9–21.8%, N = 2.7–2.9%, P = 0.9–1.9%, $pH_{pzc} \approx$ 2.00–2.61 Biochars: S = 7 m^2/g, V = 0.026 cm^3/g, APS = 1353 nm, C = 85.3%, O = 12.2%, N = 2.5%, pH_{pzc} = 3.14 BM-BCs: S = 433 m^2/g, S_{micro} = 356 m^2/g, V = 0.379 cm^3/g, V_{micro} = 0.158 cm^3/g, APS = 414 nm, C = 78.3%, O = 18.0%, N = 3.7%, pH_{pzc} < 2.0	U(VI)	T = 298.15–338.15 K, pH = 4.0	Langmuir model	78.6–114.9 mg/g [a] Biochars: 23.2–43.3 mg/g [a] BM-BCs: 73.4–100.5 mg/g [a]	PSO	60 min	Complexation, electrostatic attraction, cation–π bonding, and coordination	[89]

Table 1. *Cont.*

Materials	Ball Milling Treatment	Material Characterization	Pollutants	Experimental Condition	Isotherm Model	Adsorption Experiment Adsorption Capacity	Kinetic Model	Equilibrium Time	Adsorption Mechanism	Ref.
Thiol-modified biochars	BM: biochars (2 g) + 3-trimethoxysilyl-propanethiol (1.6 mL with strong nitrogen purging) + DW (2.4 mL) + ethanol (76 mL) + NH_4OH, agate balls (Φ = 3, 5, 15 mm, 200 g, MR = 3:5:2), RS = 400 rpm, MT = 30 h, TA= 6 h	S = 56.05—458.94 m^2/g, V = 0.271–0.635 cm^3/g; D = 5.53–19.34 nm, C = 59.15–71.24%, O = 18.45–27.95%, N = 0–2.25%, S = 2.98–5.63%, Si = 7.03–10.77%, O/C = 0.259–0.473, pH_{pzc} < 2. BM-BC: S = 3.78–385.80 m^2/g, V = 0.0163–0.182 cm^3/g, D = 2.59–17.22 nm, C = 73.12–87.49%, O = 12.51–25.88%, Si = 1–1.00%, O/C = 0.143–0.354, pH_{pzc} < 2	Hg(II)	T = 25± 0.2 °C, pH = 7.0 ± 0.2	Langmuir model	270.60 ± 2.67–401.8 ± 2.27 mg/g [a] BM-BC:163.70 ± 8.45–386.34 ± 23.45 mg/g [a]	PSO	4 h Ball-milled biochar: 1 h	Surface adsorption, electrostatic attraction, surface complexation, and ligand exchange.	[55]
Ball-milled CNTs-based materials										
HA-MWCNTs	V, BM: CNTs (0.01 g) + HA (1.0 g), stainless steel ball (Φ = 30.0 mm, 112.0 g), RS = ~ 617 rpm, MT = 15 min	C = 74.2%, O = 20.2%, Si = 3.1%, Al = 2.5%, Zeta potential (DW) = −42.5 ± 1.0 mV	Cu(II)	Reconstituted water (Daphnia magna medium), pH = 7.0	-	68.5 ± 3.5 mg/g [a]	-	3 h	Chemical complexation	[116]
CeO_2-CNTs	BM: CNTs	—	Cr(VI)	T = 25 °C, pH = 3–11	Langmuir model	23.26–31.55 mg/g [a]	-	-	Specific affinity between hydrous oxides of Ce and Cr(VI)	[176]

Table 1. *Cont.*

Materials	Ball Milling Treatment	Material Characterization	Pollutants	Experimental Condition	Isotherm Model	Adsorption Experiment Adsorption Capacity	Kinetic Model	Equilibrium Time	Adsorption Mechanism	Ref.
FeO$_x$@CNTs	P, BM: CNTs (0.2 g) + FeCl$_3$·6H$_2$O (0.6 g) + KOH (1.25 g), a spherical planetary ball mill, agate ball (Φ = 5 mm, 200 g), RS = 300 rpm, MT = 12 h, TA = 3 h	S = 242 m^2/g, V = 0.523 cm^3/g, D = 3.42 nm, pH$_{pzc}$ = 4.3 CNTs: S = 228 m^2/g, V = 1.86 cm^3/g, D = 30.5 nm, pH$_{pzc}$ = 5.7	Sb(III)	T = 298 K, pH = 6.35	Redlich–Peterson model	172 mg/g [a] CNTs: 4.01 mg/g [a]	PSO	12 h	Complexation and surface pore adsorption	[66]
Ball-milled graphenes-based materials										
Ball-milled graphene sheets	BM: graphene sheets + N-methylpyrrolidone, stainless steel ball, RS = 300 rpm, MT = 50 h	-	U(VI)	T = 298 K pH = 4.5	Langmuir model	71.93 mg/g [a]	PSO	2 h	Chemical oxidation	[32]
HGO	P, BM: jaggery + graphite + DW, hydrothermal treatment, and further calcination, MR = 100:1, stainless steel balls (Φ = 1 cm and 2 cm), RS = 70 rpm, MT = 30 h	-	Cr(VI)	pH = 1	-	5.48 mg/g [c]	-	1 h	C–O–C and –OH functionalities, aromatic π network	[127]

Table 1. *Cont.*

Materials	Ball Milling Treatment	Material Characterization	Pollutants	Experimental Condition	Isotherm Model	Adsorption Experiment Adsorption Capacity	Kinetic Model	Equilibrium Time	Adsorption Mechanism	Ref.
PGO	P, BM: graphene (2 g) + dry ice (40 g), modification by PCl_3, ZrO_2 balls, RS = 350 rpm, MT = 48 h, RP = 10 min	S = 25 m^2/g, C = 85.4%, O = 14.2% and P = 0.4%	Hg(II)	Room temperature, pH = 7	Langmuir model	82.2 mg/g [a]	PSO	-	Complexation	[121]
Ball-milled metal-based materials										
FeS$_2$-ZVIs	BM: ZVIs + FeS_2 (total amount = 5.0 g, MR = 1:0, 4:1, 1:1, 1:4 and 0:1), steel balls (4.0 g), RS = 300 rpm, MT = 30 min	S = 0.912 m^2/g, O = 5.87%, S = 27.12%, Fe = 67.00%. Ball-milled FeS_2: S = 1.190 m^2/g, O = 13.99%, S = 43.48%, Fe = 42.53%. Ball-milled ZVIs: S = 0.800 m^2/g, O = 11.77%, S = 0.70%, Fe = 87.52%	As(III)	T = 25 °C, pH = 6.8	-	78.3–97% [c] Ball-milled FeS_2: 18.1% [c] Ball-milled ZVIs: 19.3% [c]	-	90 min	-	[151]
Sulfidated ZVIs	P, BM: ZVIs + S (MR = 0.1–0.2), ZrO_2 balls, RS = 400 rpm, MT = 20 h, N_2 atmosphere	S = 1.46–2.08 m^2/g Ball-milled ZVIs: S = 0.21 m^2/g	Cr(VI)	T = 25 ± 0.5 °C, pH = 6	-	3.831mg/g [b]	PSO	180 min	-	[177]
LS-ZVIs	P, BM: ZVIs (2.5 g) + lignosulfonate (0.025–0.25 g), ZrO_2 balls (Φ = 6 mm), RS = 400 rpm, MT = 2–20 h, Ar headspace	S = 2.59 m^2/g, Fe(0) = 10.5%, Fe(II) = 59.7%, Fe(III) = 19.8% ZVIs: S = 0.76 m^2/g, Fe(0) = 3.4%, Fe(II) = 76.9%, Fe(III) = 19.7%	Cr(VI)	T = 25 °C, pH = 5.5	-	4.0–100% [c] ZVIs: ≈0% [c]	PSO	60 min	Chemical adsorption	[157]

Table 1. *Cont.*

Materials	Ball Milling Treatment	Material Characterization	Pollutants	Experimental Condition	Isotherm Model	Adsorption Experiment Adsorption Capacity	Kinetic Model	Equilibrium Time	Adsorption Mechanism	Ref.
Sulfidated ZVIs	P, BM: ZVIs + S (MR = 0.01–0.2), ZrO_2 balls (Φ = 6 mm), RS = 400 rpm, MT = 20 h, Ar headspace	S = 1.5 m^2/g Ball-milled mZVIs: S = 0.21 m^2/g	As(III)	T = 25 ± 5 °C, pH = 7, oxic condition	-	174.91–275.10 mg/g [d] Ball-milled ZVIs: 353.27 mg/g [d]	PSO	24 h Ball-milled ZVIs: 72 h	Chemical adsorption	[156]
Coffee grounds-modified ZVIs	P, BM: ZVIs + coffee grounds (MR = 2–8%), ZrO_2 balls (Φ = 6 and 9 mm, 100 g, MR = 3:2), RS = 550 rpm, MT = 2 h	S = 1.48–1.85 m^2/g, APS = 80 μm, Fe = 84.20–95.70%, C = 0.75–3.60%, O = 3.55–12.20% Ball-milled ZVIs: S = 1.45 m^2/g, APS = 71 μm, Fe = 98.20%, C = 0.55%, O = 1.25%	Cr(VI)	T = 25 °C, pH = 6.5	-	80–100% [c] Ball-milled ZVIs: <10% [c]	PFO	120 min	Complexation	[160]
ZVAls/Fe_3O_4	P, BM: ZVAls (2 g) + Fe_3O_4 (1.0 g), ZrO_2 balls (3.0g), RS = 300 r/min, MT = 1.5 h	S = 6.5154 ± 0.1963 m^2/g, pH_{pzc} = 9.2, SM = 10.03 emu/g ZVAls: S = 4.0427± 0.7390 m^2/g	Cr(VI)	T = 25 ± 2 °C, pH = 7	Langmuir model	8.10 mg/g [a]	PFO	30 min ZVAls: 50 min	Surface adsorption	[34]
ZVAls/MFe_2O_4 (M = Mn, Zn, Ni)	BM: ZVAl (1.0 g) + MFe_2O_4 powders (0.5 g), ZrO_2 balls (Φ = 8, 4, 2, 1 mm, 15 g, MR = 1: 2: 4: 8), RS = 300 rpm, MT = 2 h	S = 17.344–24.646 m^2/g, V = 0.067–0.076 cm^3/g; D = 5.136–7.443 nm, pH_{pzc} ≈ 9.5, SM = 7.84–51.59 emu/g ZVAls: S = 1.826 m^2/g, V = 0.007 cm^3/g, D = 4.140 nm	Cr(VI)	T = 298 K, pH = 7	-	89.15–100% [c] ZVAls: 0% [c]	PSO	30 min	Surface adsorption and ion exchange	[161]

Notes: P: planetary ball mills; V: ultrafine vibration ball mills; DW: deionized water; Φ: ball diameter; MR: mass ratio. MM: ratios of materials to balls; RS: rotate speed; MT: milling time; TA: time of alteration rotation direction; RP: a rest period; T: times; S: surface area; V: pore volume; APS: average particle size; D: average pore diameter; AFGs: acidic functional groups; OFGs: oxygen functional groups; CEC: cation exchange capacity; TAG: total acidic group; pH_{pzc}: point of zero charge; MS: values of saturation magnetization; [a]: maximum adsorption amounts obtained from adsorption isotherm parameters; [b]: values obtained from the Freundlich model; [c]: adsorption amounts/adsorption rates at equilibrium; [d]: adsorption amounts obtained from kinetic parameters; PFO: pseudo-first-order mode; PSO: pseudo-second-order mode.

4.2. Removal of Organic Pollutants

Table 2 lists the removal of organic pollutants by various ball-milled modified materials. Nasrullah et al. [56] indicated that BM-ACs were conductive to remove cationic methylene blue (MB) via electrostatic interaction, and the adsorption amount of MB was positively related to the particle size of BM-ACs. The Langmuir-model-based maximum adsorption amount of MB on BM-ACs was 505 mg/g. The kinetic data followed the pseudo-second-order model, and both film and intraparticle diffusion controlled the process. The negative value of $\Delta G°$ and positive values of $\Delta H°$ and $\Delta S°$ demonstrated that MB adsorption by BM-ACs was spontaneous and endothermic. On the contrary, Gohr et al. [77] implied that the grafted carboxylic groups played a major role in cationic dye adsorption. The maximum adsorption amount of MB and crystal violet (CV) by AC–COOH were 123.02 and 120.30 mg/g, respectively, with an equilibrium time of 15 min. The thermodynamic study claimed that the adsorption process of MB and CV on AC–COOH was spontaneous and endothermic. Ball milling ACs with Fe_3O_4 not only introduced magnetic properties through mechanical extrusion but were also available to further improve MB adsorption capacity [104]. Meng et al. [180] suggested that extending the mass ratio of Fe_3O_4 and balling milling time to ACs could increase the magnetic separation property but reduce the adsorption capacity for perfluorinated compounds (PFCs). The positive relationship between adsorption capacity and the chain length of PFCs indicated that hydrophobic interaction played a major role in PFC adsorption by magnetic ACs.

Since the physicochemical properties of organic pollutants are different, there is a discrepancy in the organic pollutants' adsorptive behavior by BM-BCs as well as adsorption mechanisms. A combination of ball milling and 2,2,6,6-tetramethylpiperidine-1-oxyl-oxidation improved imidacloprid (IMI) and sulfadiazine (SUL) uptakes by pore filling, H-bonding, and cation/p/π–π EDA interaction, and further promoted IMI removal via electrostatic interaction and cation–π EDA interaction [33]. The formation of oxygen-containing groups and mesoporous layered structure by biochars derived from cellulosic biomass and montmorillonite (BCs-CBM) facilitated MB uptakes via ion exchange and electrostatic interaction [109]. The adsorption amount of tetracycline hydrochloride (TC) on BM-BCs was positively correlated with the external specific surface area and total pore volume/mesoporous volume, which suggested surface adsorption and pore filling were the main contributors [83]. Neutral solution (pH = 6–8) was beneficial to TC by BM-BCs ascribed to enhanced electrostatic interaction. Coexisting Na(I), K(I), and Mg(II) had an adverse effect on TC adsorption due to the competition for adsorption sites, while the presence of Ca(II) improved TC removal resulting from formation of TC-Ca^{2+} complexes. Zhang et al. [181] also reported that biochars modified by ball milling directly possessed enhanced adsorption amount of MB (from 14.4 ± 1.3–17.2 ± 3.5 mg/g to 213 ± 19–354 ± 20 mg/g) with shorter equilibrium time (16 h to 8 h) ascribed to the increasing specific surface area, pore volume, and surface oxygen-containing groups as well as exposing graphitic structure, which improved π–π interaction and electrostatic effect (Figure 7). Xu et al. [87] demonstrated that the saturation adsorption amount of reactive red (RR) based on the Langmuir model increased from 1.70–3.60 mg/g to 9.2–34.8 mg/g within 120 min on account of high external specific surface area and less negative charge on BMNCs. Pine-wood-derived nanobiochars (PWNBCs) adsorbed carbamazepine (CBZ) via hydrogen bonding interaction between NH_2 functional groups in CBZ and oxygen-containing functional groups of PWNBCs [182]. The results showed that rotational speeds were an important factor in CBZ adsorption by PWNBCs. When the rotational speed was raised from 90 to 210 rpm, the adsorption rate of CBZ increased from 29% to 67%. But the removal rate did not increase with further increasing the rotational speed. It was probably because the improvement in rotational speed could lead to the thinner boundary layer and then enhance the mass transfer rate. The addition of the surfactant (Tween 80) promoted CBZ onto PWNBCs because the formation of hydrogen bonding between O and N in the amide group of CBZ and hydrophilic head of Tween 80 and hydrophobic interaction between the hydrophobic tail of Tween 80 and graphite-like structure of PWNBCs. In addition, the

adsorption of galaxolide [183], sulfamethoxazole (SMX) [84,184,185], sulfapyridine [184], TC [170], ciprofloxacin (CIP) [186] and fluconazole [187] by BM-BCs involving pore filling, π–π conjugation, complexation, electrostatic interaction, H-bonding interaction, hydrophobic effect, or their combined interactions. The co-existence of NaCl, NaNO$_3$, and CaCl$_2$ (0–100 mmol/L) had negligible effects on SMX adsorption on ball milling and magnetization co-modified sludge-derived biochars (BC-SBCs) [185] and BM-PBCs [171], which was attributed to the weak contribution of salting out enhancement effect and electrostatic screening inhibition impact or the equivalence of their actions. The coexisting HCO$_3^-$ might increase the pH values of the solution to increase the electrostatic repulsion or compete for adsorption sites to inhibit SMX adsorption on BC-SBC and BM-PBC. The presence of HA was insensitive to SMX removal by BC-SBC and BM-PBC, which was assigned to the weak action of both completion and promotion effects. Li et al. [170] presented that the increase in NaNO$_3$ slightly decreased TC adsorption on BM-MBCs due to the competition for available adsorption sites. Tang et al. [186] suggested that both NaNO$_3$ and CaCl$_2$ had adverse impacts on CIP adsorption by the Fe-Mg-layered double oxides bagasse biochars (BM-LDOs-BC) resulting from the competition for available adsorption sites and the soluble complexes between cationic CIP and the inorganic salt. The higher inhibitory intensity of CaCl$_2$ than NaNO$_3$ was ascribed to the larger ionic strength of CaCl$_2$.
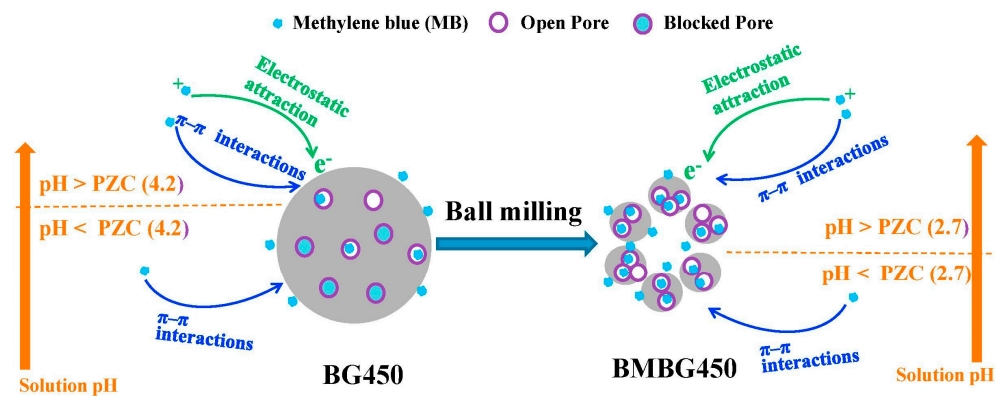

Figure 7. Mechanism diagrams of governing mechanisms of MB adsorption onto unmilled and milled biochars [181]. Reprinted from Chemical Engineering Journal, 335, Lyu H., Gao B., He F., Zimmerman A.R., Ding C., Tang J., Crittenden J.C. Experimental and modeling investigations of ball-milled biochar for the removal of aqueous methylene blue, 110–119, Copyright (2018), with permission from Elsevier.

The acidic and alkaline one-step ball milling of hickory wood without pyrolysis possessed great carbonization and a large diversity of oxygen-containing functional groups to effectively remove dyes [53,109]. H$_2$O$_2$ modification could introduce more oxygen-containing functional groups to biochars to improve cationic MB adsorption [188], while NH$_3$·H$_2$O [90] and CuO [96] modification were available to graft protonated and positively charged groups to biochars to enhance anionic reactive red (RR) uptakes. Thiol-modified biochars improved MeHg uptakes from 19.53 ± 1.03–25.54 ± 4.12 to 39.14 ± 1.46–108.16 ± 3.11 mg/g (saturated adsorption capacity) within equilibrium time reducing from 24 h to 9 h via surface adsorption, electrostatic attraction, surface complexation and ligand exchange [55]. But the excessive 3-MPTS decreased MeHg uptakes due to the self-polymerize on the surface of biochars. The zeta potential and the point of zero charge of N-doped biochars by ball milling biochars with NH$_3$·H$_2$O increased, which was beneficial to anionic RR removal through electrostatic interaction [90]. The TC adsorption amount increased from 37.8 mg/g to 81.3 mg/g after ball milling biochars with NH$_3$·H$_2$O, and the TC uptakes further increased to 132.6 mg/g after ball milling N-doped biochars with FeS [10]. The TC adsorption by BM-FeS@NBCs was endothermic and spontaneous. The TC adsorption capacity was related to pH values with the maximum adsorption capacity of TC at pH = 4. The addition of cationic Na(I), K(I), Ca(II), and Mg(II) promoted TC adsorption capacity

by BM-FeS@NBCs due to the decreasing electrostatic repulsion between BM-FeS@NBCs and TC.

The CuO embedded on the surface of biochars made adsorption sites positively and had the ability to remove anionic RR via electrostatic attraction with a short equilibrium time (3 h) [96]. The pH values of 4–10 did not affect RR adsorption significantly since the point of zero charge of CuO-biochars was around 10, and electrostatic attraction was the main adsorption mechanism. The Fe_3O_4 [174] and $FeCl_3$ [189] loaded on biochars were beneficial to TC removal, which was increased by 71.22% and 82.64%, respectively. The TC adsorption process by both BM-Fe_3O_4-BC [174] and iron-containing biochars (Fe@MBC) [189] was spontaneous and endothermic, and TC uptakes increased with increasing temperatures. The ionic strength had an ignorable effect on the TC adsorption by Fe@MBC because the electrostatic effect was not the major mechanism [189]. The presence of K(I), NO_3^-, Cl^- and SO_4^{2-} favored TC adsorption by Fe@MBC, whereas Cu(II), Na(I), PO_4^{3-} and CO_3^{2-} unfavored TC uptakes onto Fe@MBC [189]. Qu et al. [174] suggested that the coexisting Ca(II) could act as a bridge to promote TC removal on BM-Fe_3O_4-BC. The Fe_3O_4 on biochars also improved MB adsorption amount by almost 27-fold compared to BM-BCs, and the alkaline solution was beneficial to MB removal due to less competition between H^+ and MB [104]. However, Yan et al. [190] found that the loading of magnetic powers blocked the pores of biochars, resulting in a decreasing adsorption amount of MB, and an extra ball milling step counteracted the reduction in adsorption invariably caused by magnetite loading due to the restoration of specific surface area and surface functional groups. The experimental data were in agreement with Freundlich and pseudo-second-order models. The thermodynamic study showed that it was a spontaneous and endothermic process governed by chemical adsorption and π–π and electrostatic interactions were the main adsorption mechanism for MB on the twice-milled magnetic biochars.

Because CNTs' ends are closed and aggregated seriously in water, the adsorption sites on the outer surface decrease significantly and thus have adverse effects on pollutant removal. CNTs become short and open and have few tangled phenomena after ball milling, which enhanced aniline and nitrobenzene adsorptive removal with the adsorption capacity increasing from 14.9 mg/g to 22.2–36.2 mg/g and 19.8 mg/g to 24.4–41.5 mg/g, respectively [113,191]. The adsorption capacity of aniline and nitrobenzene by ball-milled CNTs was positive to the ball milling time, and the main adsorption mechanism was the capillary effect on both short open-ended inner cavities and compressed aggregated pores. Ball-milled carbon/CNTs were available to remove sodium fluoride via physical adsorption and ion exchange. The ball-milled carbon/CNTs could adsorb fluoride ions at low pH, and the experimental data fitted the pseudo-second-order model and Langmuir model well. The thermodynamic study showed that the adsorption process was endothermic, spontaneous, and more random. The large specific surface area and ion exchange were responsible for fluoride ions removal onto ball-milled carbon/CNTs [192].

The ECG presented high adsorptive rates (>90%) toward both cations and anions dyes within 5–20 min via physical absorption and electrostatic interaction [125]. In addition, a removal rate of 99.23 $\pm$ 0.14% achieved by ECG for the mixture dyes solution suggested that ECG had remarkable potential for industrial dyes removal. An increase in the number of active metal sites on the nickel-based metal–organic framework/graphene oxide composites (Ni-MOF-GO) improved congo red (CR) adsorption due to the enhanced acid–base interaction between active metal sites (Lewis acid) and –NH_2 (Lewis base) [131]. The adsorption data, in accordance with the Freundlich model, implied heterogeneous adsorption surfaces with multilayer adsorption. The thermodynamic study suggested that it was physisorption with spontaneous, endothermic, and more random. Al–carbon composites synthesized via NaCl-aided ball milling had the ability to adsorb hexabromocyclododecane in 1 h with >90% removal rates at a dosage of 4 g/L and initial concentration of 2 mg/L. The adsorbed hexabromocyclododecane was enriched on the carbon surface of obtained materials and ready for subsequent degradation [164].

Table 2. Ball-milled adsorbents' characterization and their application for organic pollutants adsorptive removal.

Materials	Treatment	Material Characterization	Pollutants	Experimental Condition	Isotherm Model	Adsorption Experiment Adsorption Capacity	Kinetic Model	Equilibrium Time	Adsorption Mechanism	Ref.
Ball-milled ACs-based materials										
BM-ACs	BM: ACs (1 g), milling balls (4 g), RS = 350 rpm, MT = 60 min	S = 496.32 m^2/g, V$_t$ = 0.278 cm^3/g, V$_{micro}$ = 0.203 cm^3/g, V$_{meso}$ = 0.075 cm^3/g, D = 2.248 nm, APS = 1.57 μm, pH$_{pzc}$ = 6.46 ACs: S = 526.80 m^2/g, V$_t$ = 0.293 cm^3/g, V$_{micro}$ = 0.182 cm^3/g, V$_{meso}$ = 0.110 cm^3/g, D = 2.225 nm, APS = 5.30 μm	MB	T = 25 °C, pH = 10	Langmuir model	505 mg/g [a] Biochars: 227.14 mg/g [c]	PSO	420 min	Electrostatic interaction	[56]
AC-COOH	P, BM: ACs (5 g) + NaOH (25 g) + DW (50 mL), RS = 400 rpm, MT = 6 h BM: obtained materials + chloroacetic acid (25 g), RS = 400 rpm, MT = 6 h	C = 79.00%, O = 21.00%, pH$_{pzc}$ = 6.20	MB ——— CV	T = 20 °C, pH = 7	Langmuir model	123.02 mg/g [a] ——— 120.3 mg/g [a]	PSO	15 min	Electrostatic interaction	[77]
Magnetic ACs	P, BM: ACs (0.45 g) + Fe$_3$O$_4$ (1.35 g), agate balls (Φ = 6 mm, 180 g), RS = 500 rpm, MT = 12 h	S = 75.4 m^2/g, V = 0.05 cm^3/g, D = 2.6 nm, APS = 609 nm, C = 47.4%, H = 0.71%, O = 25.0%, N = 0.02%, Fe = 21.6%, pH$_{pzc}$ < 3, MS = 33.8 emu/g ACs: S = 743.7 m^2/g, V = 0.39 cm^3/g, D = 2.1 nm, APS = 0.5–1 mm, C = 70.8%, H = 2.97%, O = 18.7%, N = 0.05%, Fe = 0.04%, pH$_{pzc}$ < 3 BM-ACs: S = 544.9 m^2/g, V = 0.31 cm^3/g, D = 2.3 nm,	MB	T = 25 ± 2 °C	Langmuir model	304.2 mg/g [a] BM-ACs: 298.7 mg/g [a] ACs: 111.9 mg/g [a]	PSO	8 h	-	[104]

Table 2. *Cont.*

Materials	Treatment	Material Characterization	Pollutants	Experimental Condition	Isotherm Model	Adsorption Experiment		Equilibrium Time	Adsorption Mechanism	Ref.
						Adsorption Capacity	Kinetic Model			
		APS = 479 nm, C = 72.7%, H = 2.63%, O = 17.4%, N = 0.09%, Fe = 0.03%, pH_{pzc} < 3								
Magnetic ACs	P, BM: ACs (2.25 g) + Fe_3O_4 (0.75 g), milling balls (Φ = 5.60 mm, 120 g), RS = 550 rpm, MT = 2 h, TA = 0.5 h	C = 66.3%, O = 17.4%, Si = 0.3%, Fe = 16.1%, APS ≈ 1 μm, pH_{pzc} ≈ 6.46, MS = 24.2 emu/g ACs: C = 95.5%, O = 3.8%, Si = 0.7%, Fe = 0.0%, APS = 48 μm	Potassium perfluorooctane sulfonate	T = 28 °C	Langmuir model	1.63 mmol/g [a]	PFO	<2 h	Hydrophobic interaction	[180]
			Perfluorooctanoic acid			0.90 mmol/g [a]				
			Potassium perfluorohexane sulfonate			0.33 mmol/g [a]				
			Potassium perfluorobutane sulfonate			0.21 mmol/g [a]				
Ball-milled biochar-based materials										
Graphite-like biochars	BM: aqueous mixture of biomass (newspaper or maize straw raw), oxidation and pyrolysis, agate balls (200 g), RS = 300 rpm, MT = 2 h	S = 871.5–1065 m^2/g, V = 1.46–4.45 cm^3/g, V_{macro} = 0.031–0.145 cm^3/g, V_{meso} = 1.13–3.53 cm^3/g, V_{micro} = 0.304–0.768 cm^3/g, D = 4.9–8.5 nm, C = 68.5 ± 0.16–84.9 ± 0.23%, H = 1.4 ± 0.06–1.5 ± 0.14%, O = 4.7 ± 0.17–6.4 ± 0.01%, N = 0.5 ± 0.07–0.7 ± 0.05%, (O + N)/C = 1.53–1.65, H/C = 0.20–0.26	IMI	T = 25 ± 1 °C, pH = 8.0–8.7	Freundlich model	67.8–181.1 $(mg/g)/(mg/L)^{n}$ [b] Biochars: 4.74–19.8 $(mg/g)/(mg/L)^{n}$ [b] Biochars derived from ball-milled biomass: 13.3–16.2 $(mg/g)/(mg/L)^{n}$ [b]	-	-	Pore filling, H-bonding, and cation/p/π–π EDA interactions	[33]

Table 2. *Cont.*

Materials	Treatment	Material Characterization	Pollutants	Experimental Condition	Isotherm Model	Adsorption Experiment Adsorption Capacity	Kinetic Model	Equilibrium Time	Adsorption Mechanism	Ref.
Graphite-like biochars	BM: aqueous mixture of biomass (newspaper or maize straw raw), oxidation and pyrolysis, agate balls (200 g), RS = 300 rpm, MT = 2 h	Biochars derived from biomass: S = 144.8–545.8 m^2/g, V = 1.52–1.89 cm^3/g, V_{macro} = 0.015–0.034 cm^3/g, V_{meso} = 1.25–1.52 cm^3/g, V_{micro} = 0.257–0.330 cm^3/g, D = 7.8–11.4 nm, C = 72.0 ± 0.10–85.5 ± 0.17%, H = 1.8 ± 0.01–1.9 ± 0.10%, O = 2.6 ± 0.60–4.3 ± 0.35%, N = 0.7 ± 0.02–1.3 ± 0.07%, (O + N)/C = 1.66–1.68, H/C = 0.25–0.32 Biochars derived from ball-milled biomass: S = 277.0–407.5 m^2/g, V = 0.78–1.11 cm^3/g, V_{macro} = 0.025–0.028 cm^3/g, V_{meso} = 0.57–0.89 cm^3/g, V_{micro} = 0.179–0.195 cm^3/g, D = 7.0–9.6 nm, C = 71.8 ± 0.18–85.3 ± 0.25%, H = 1.8 ± 0.01–1.9 ± 0.03%, O = 2.6 ± 0.29–4.2 ± 0.61%, N = 0.7 ± 0.02–1.4 ± 0.08%, (O + N)/C = 1.68–1.69, H/C = 0.25–0.32	SUL	T = 25 ± 1 °C, pH = 8.0–8.7	Freundlich model	40.2–43.1 $(mg/g)/(mg/L)^{n}$ [b] Biochars derived from biomass: 8.41–12.6 $(mg/g)/(mg/L)^{n}$ [b] Biochars derived from ball-milled biomass: 10.8–16.0 $(mg/g)/(mg/L)^{n}$ [b]	-	-	Pore filling, H-bonding, cation/p/π–π EDA interactions, and electrostatic interactions	[33]
BCs-CBM	P, BM: cellulose+ montmorillonite, pyrolysis, RS = 1000 r/min, MT = 4 h	S = 95.472 m^2/g, V = 0.123 cm^3/g, D = 2.2–4.2 nm	MB	T = 25 °C	Freundlich model	11.489 ± 1.516 $(mg/g)/(mg/L)^{n}$ [b]	PSO	8 h	Cation exchange	[82]

Table 2. *Cont.*

Materials	Treatment	Material Characterization	Pollutants	Experimental Condition	Isotherm Model	Adsorption Experiment Adsorption Capacity	Kinetic Model	Equilibrium Time	Adsorption Mechanism	Ref.
Acidic ball-milled biochars	P, BM: hickory chips (1 g) + H_2SO_4 (20 mL, 9.2 mol/L, pH = 1.265) + DW (20 mL), agate balls (Φ = 6 mm, 100 g) RS = 300 rpm, MT = 12 h, RT = 3 h, ambient air	S = 5.619 m^2/g, V = 0.012 cm^3/g, APS = 0.3–4 µm	TY	T = 25 °C	Freundlich model	182.3 mg/g [a]	PSO	12 h	Ion exchange and electrostatic interaction	[109]
Biosorbents derived from acidic and alkaline one-step ball milling of hickory wood	P, BM: hickory wood (1 g) + H_2SO_4 (20 mL, 9.2 mol/L)/NaOH (20 mL, 3.75 mol/L), agate balls (Φ = 6 mm, 100 g), RS = 300 rpm, MT = 24 h, RT = 3 h	S = 5.191–5.619 m^2/g, V = 0.023–0.030 cm^3/g	CR / CV	T = 25 °C	Freundlich model	0.68 ± 0.20–311.01 ± 2.13 $(mg/g)/(mg/L)^{n}$ [b] / 149.02 ± 4.62 $(mg/g)/(mg/L)^{n}$ [b]	PSO	>8 h / >3 h	Surface complexation	[53]
BM-BCs	BM: biochars (10 g), ZrO_2 balls, RS = 1600 rpm, MT = 60 s, T = 30	S = 74.39 m^2/g, V = 0.1540 cm^3/g, D = 8.3741 nm, C = 54.36%, N = 2.80%, O = 30.65%, pH_{pzc} = 2.3 Biochars: S = 46.20 m^2/g, V = 0.1274 cm^3/g, D = 10.9337 nm, C = 63.22%, N = 3.19%, O = 23.94%	MB	T = 298–308 K	Langmuir model	408.79–419.11 mg/g [a]	PSO	120 min	-	[167]
BM-BCs	P, BM: biochars (1.8 g), agate balls (Φ = 6 mm, 180 g), RS = 300 rpm, MT = 12 h, TA = 3 h	S = 331 m^2/g, V = 0.099 cm^3/g, APS = 170nm, AFGs = 1.35 mmol/g, -COOH = 0.45 mmol/g, lactonic groups = 0.05 mmol/g, –OH = 0.85 mmol/g, pH_{pzc} = 2.7	MB	T = 20 ± 2 °C, pH = 4.5 and 7.5	Dual Langmuir model	213 ± 19–354 ± 20 mg/g [a] Biochars: 14.4 ± 1.3–17.2 ± 3.5 mg/g [a]	PSO	8 h Biochars: 16 h	pH = 4.5: π–π interaction pH = 7.5: π–π interaction and electrostatic effect	[181]

Table 2. *Cont.*

Materials	Treatment	Material Characterization	Pollutants	Experimental Condition	Isotherm Model	Adsorption Experiment Adsorption Capacity	Kinetic Model	Equilibrium Time	Adsorption Mechanism	Ref.
		Biochars: S = 51 m^2/g, V = 0.008 cm^3/g, APS = 0.5–1 nm, AFGs = 0.30 mmol/g, lactonic groups = 0.08 mmol/g, –OH = 0.23 mmol/g, pH$_{pzc}$ = 4.2								
BM-BCs	P, BM: biochars (1.8 g), steel balls (Φ = 5 mm, 180 g), RS = 300 rpm, MT = 24 h, TA = 3 h, N$_2$/vacuum environment	S = 300–452 m^2/g, D = 140–223 nm, C = 77.3–82.8%, O = 15.2–19.9%, Si = 1.50–3.00%, O/C = 0.184–0.257, –C–O = 13.6–15.9%, –C=O = 1.61–4.09%, pH$_{pzc}$ < 2.2 Biochars: S = 2.60–343 m^2/g, C = 86.5–92.8%, O = 6.70–12.5%, Si = 0.0–0.90%, O/C = 0.072–0.145, –C–O = 6.37–10.9%, –C=O = 1.33–1.56%, pH$_{pzc}$ ≈ 2.2	RR	T = 25 ± 2 °C, pH = 6 ± 0.1	Langmuir model	9.2–34.8 mg/g [a] Before: 1.70–3.60 mg/g [a]	PSO	120 min	Electrostatic adsorption	[87]
PWNBCs	P, BM: biochars, stainless steel balls (Φ = 2.4 mm, 45 g), RS = 575 rpm. MT = 100 min, ambient conditions	S = 47.25 m^2/g, APS = 60 ± 20 nm, C = 83.1%, H = 3.5%, N < 1%, CEF = 14.8 ± 1.2 meq/100, zeta potential (6.61) = −31.3 mV	CBZ	T = 25 ± 1 °C, pH = 6.0	Freundlich model	0.068 (ng/mg)(L/ng)$^{1/n}$ [b]	PSO	2 d	Hydrogen bonding	[182]

Table 2. *Cont.*

Materials	Treatment	Material Characterization	Pollutants	Experimental Condition	Isotherm Model	Adsorption Experiment Adsorption Capacity	Kinetic Model	Equilibrium Time	Adsorption Mechanism	Ref.
BM-BCs	P, BM: biochars, agate balls (Φ = 5 mm), MM = 1:100, RS = 300 rpm, MT = 24 h TA = 3 h	S = 10.8–401 m^2/g, V = 0.043–0.076 cm^3/g, D = 15.1–48.1 nm, C = 58.1–62.7%, H = 1.50–6.80%, O = 30.8–34.6%, N = <0.01–0.50%, O/C = 0.46–0.60, H/C = 0.02–0.12, (O + N)/C = 0.59–0.75, total organic carbon = 541–666 mg/g Biochars: S = 1.25–328 m^2/g, V = 0.002–0.031 cm^3/g, D = 3.42–23.0 nm, C = 61.0–70.0%, H = 0.64–4.61%, O = 29.4–33.9%, N = <0.01–0.52%, O/C = 0.42–0.56, H/C = 0.01–0.08, (O + N)/C = 0.42–0.56, total organic carbon = 553–565 mg/g	Galaxolide	T = 20 $\pm$ 2 °C	Freundlich model	588 ± 31.2f 1955 ± 157 $(mg/kg)/(mg/L)^{n}$ [b] Biochars: 247 ± 3.78- 579 ± 43 $(mg/kg)/(mg/L)^{n}$ [b]	-	48 h	Hydrophobic effect, π–π interaction, and micropore filling	[183]
BM-BCs	P, BM: biochars, milling balls, MM = 1:100, RS = 300 rpm, MT = 24 h, TA = 3 h	S = 13.5–139.89 m^2/g, V = 0.0706–0.3366 cm^3/g, V_{meso} = 0.0706–0.3366 cm^3/g, D = 2.27–4.03 nm, AFGs = 0.48–1.62 mmol/g Biochars: S = 3.9–211.56 m^2/g, V = 0.0174–0.1370 cm^3/g, V_{meso} = 0.0172–0.0473 cm^3/g, D = 2.28–4.84 nm, AFGs = 0.01–1.48 mmol/g	TC	T = 25°C, pH = 7.0	Langmuir model	51.04–96.69 mg/g [a] Biochars: 17.19–21.29 mg/g [a]	PSO	60 h	Surface adsorption and pore filling	[83]

Table 2. *Cont.*

| Materials | Treatment | Material Characterization | Pollutants | Experimental Condition | Isotherm Model | Adsorption Experiment | | Equilibrium Time | Adsorption Mechanism | Ref. |
						Adsorption Capacity	Kinetic Model			
BM-BCs	P, BM: biochars, milling balls (Φ = 6 mm, 180 g), MM = 1:100, RS = 300 rpm, MT = 12 h, RT = 3 h	S = 309.0 m^2/g, zeta potential (pH = 3.5–8.5) = −36–43 mV Biochars: S = 9.8 m^2/g	SMX	T = 25 ± 0.5 °C, pH = 6.0	Langmuir model	100.30 mg/g [a]	Elovich model	8–12 h	Hydrophobic interaction, π–π interaction, hydrogen bonding, and electrostatic interaction	[184]
			Sulfapyridine			57.90 mg/g [a]		12 h		
BM-BCs	P, BM: MBC (1 g), agate balls (Φ = 5 mm, 100 g), MT = 12 h, TA = 20 min, RP = 10 min	S = 296.3 m^2/g, V = 0.091 cm^3/g, C = 47.98%, H = 0.88%, O = 27.89%, N = 0.53%, Fe = 12.32%, Na = 0.13%, Mg = 0.61%, Si = 0.13%, Ca = 2.13%, P = 0.12%, K = 0.88%, pH$_{zpc}$ = 4.43, MS = 15.39 emu/g Magnetic biochars: S = 198.6 m^2/g, V = 0.006 cm^3/g, C = 57.82%, H = 2.48%, O = 21.98%, N = 0.87%, Fe = 1.25%, Na = 0.12%, Mg = 0.58%, Si = 0.11%, Ca = 2.10%, P = 0.11%, K = 0.81, MS = 10.76 emu/g	TC	T = 24 ± 2 °C	Langmuir model	268.3 mg/g [a]	PSO	12 h	Electrostatic interactions, hydrogen bonds, and π–π interaction	[170]
BM-BCs	BM: MBC (1 g), stainless steel balls (Φ = 6 and 10 mm, 100 g, MR = 2: 8), RS = 400 rpm, MT = 24 h, RT = 6 h	S = 124.96 m^2/g, C = 28.22%, H = 1.656%, O = 21.69%, N = 0.76%, O/C = 0.58, H/C = 0.70, (N + O)/C = 0.60, MS = 55.15 emu/g Magnetic biochars: S = 211.18 m^2/g, C = 31.33%, H = 0.892%, O = 11.06%, N = 0.79%, O/C = 0.26, H/C = 0.34, (N + O)/C = 0.29	Fuconazole	T = 293–313 K, pH = 5.6	Langmuir model	12.19–15.90 mg/g [a] Magnetic biochars: 2.21–3.30 mg/g [a]	Elovich model	6 h	π–π interactions, hydrogen bonding, and surface complexation	[187]

Table 2. *Cont.*

Materials	Treatment	Material Characterization	Pollutants	Experimental Condition	Isotherm Model	Adsorption Experiment Adsorption Capacity	Kinetic Model	Equilibrium Time	Adsorption Mechanism	Ref.
BC-SBCs	P, BM: MBC, RS = 500 rpm, MT = 60 min	S = 73.4 m^2/g, V = 0.186 cm^3/g, D = 10.1 nm, C = 11.42%, O = 26.71%, Si = 11.66%, Fe = 50.22%, pH_{pzc} = 3.75, MS = 12.9 emu/mg	SMX	T = 25 °C	Freundlich model	851 $(ug/g)/(ug/L)^{n}$ [b]	PSO	200 min	π–π conjugation, pore filling, H-bonding, Fe–O complexation, and electrostatic interaction	[185]
BM-PBCs	P, BM: potassium ferrate-activated biochars, agate balls (MR of large, medium, and small balls = 2:18:15), RS = 300 rpm, T = 12 h	S = 284.17–282.47 m^2/g, D = 11.62–12.10 nm, pH_{pzc} = 3.2–4.9, MS = 18.94–20.33 emu/g	TC	T = 15, 25, 35 °C, pH = 4.2	Langmuir model	56.35–90.31 mg/g [a]	Avrami fractional-order model	80–150 min	Hydrogen bonding force, complexation, pore filling, and π–π stacking	[171]
BM-LDOs-BC	P, BM: Fe-Mg-LDOs biochar, MM = 1:100, RS = 700 rpm, MT = 2 h	S = 155.90 m^2/g, V = 0.0513 cm^3/g, D = 1.316 nm, C = 56.73%, O = 27.95%, Mg = 6.60%, Fe = 8.72%, pH_{pzc} < 3. Biochars: S = 67.676 m^2/g, V = 0.000852 cm^3/g, D = 0.050 nm, C = 84.81%, O = 14.55%, Mg = 0.17%, Fe = 0.47% LDOs-BC: S = 464.89 m^2/g, V = 0.156 cm^3/g, D = 1.342 nm, C = 65.86%, O = 19.81%, Mg = 6.78%, Fe = 7.56%	CIP	T = 298 K	Freundlich model	56.80 (mg/g mg/L)$^{-1/n}$ [b]	PSO	720 min	Pore filling, electrostatic interaction, H-bonding, complexation, and π–π conjugation	[186]

Table 2. *Cont.*

Materials	Treatment	Material Characterization	Pollutants	Experimental Condition	Isotherm Model	Adsorption Experiment Adsorption Capacity	Kinetic Model	Equilibrium Time	Adsorption Mechanism	Ref.
Ball-milling iron-loaded biochars	BM: iron-loaded biochars (1.8 g), agate balls (180 g), RS = 300 rpm, MT = 12 h, RT = 3 h, air atmosphere	$S = S_{external} = 48.3$ m^2/g, C = 40.4%, O = 32.8%, Fe = 11.3%, Cl = 15.5%, pH$_{pzc}$ = 9.19–9.48. Iron-loaded biochars: S = 24.9 m^2/g, $S_{external}$ = 24.1 m^2/g, $S_{internal}$ = 0.774 m^2/g, C = 60.8%, O = 22.0%, Fe = 6.50%, Cl = 10.7%, pH$_{pzc}$ < 2.3	RR	T = 25 ± 2 °C, pH = 3 and 7.5	Freundlich model	39.2–53.8 mg^{1-n} L^n g^{-1} [b] Iron-loaded biochars: 18.1–20.2 mg^{1-n} L^n g^{-1} [b]	Elovich model	1000 min	Surface adsorption and electrostatic interaction	[193]
BP-SBCs	BM: phosphoric acid-modified biochars, stainless steel balls, MM = 1:25, RS = 500 rpm, MT = 60 min	S = 146 m^2/g, V = 0.327 cm^3/g, D = 8.95 nm, CEC = 41.5 cmol/kg, C = 40.5%, H = 0.089%, O = 48.3%, N = 1.3% Biochars: S = 39.2 m^2/g, V = 0.147 cm^3/g, D = 15 nm, CEC = 7.6 cmol/kg, C = 45.3%, H = 0.084%, O = 42.5%, N = 1.4%	SMZ	T = 25 °C	Langmuir model	46.1 mg/g [a] Biochars: 7.32 mg/g [a]	PSO	720 min	Pore filling, π–π conjugation, H-bonding, and P–O complexation	[84]
Mg/Al-BCs:	P, BM: Fe-Al bimetallic oxides functionalized biochars, MM = 1:100, RS = 700 rpm, MT = 2 h	S = 91.357 m^2/g, V = 0.105 cm^3/g, D = 4.579 nm, pH$_{zpc}$ = 3.0, MS = 4.36 emu/g Biochars: S = 23.159 m^2/g, V = 0.031 cm^3/g, D = 5.327 nm Fe-Al bimetallic oxides functionalized biochars: S = 191.85 m^2/g, V = 0.206 cm^3/g, D = 4.289 nm, pH$_{zpc}$ ≈ 6.5	TC	T = 298 K	Langmuir model	116.59 mg/g [a]	Elovich model	1440 min	π–π interaction, hydrogen bonding, complexation, and pore filling	[194]

Table 2. *Cont.*

Materials	Treatment	Material Characterization	Pollutants	Experimental Condition	Isotherm Model	Adsorption Experiment Adsorption Capacity	Kinetic Model	Equilibrium Time	Adsorption Mechanism	Ref.
H_2O_2-modified ball-milled biochars	P, BM: biochars (1.8 g), modification by H_2O_2, agate balls (Φ = 6 mm, 180 g) RS = 300 rpm, MT = 12 h, RT = 3 h	S = 9.2 m^2/g, C = 77.1%, O = 21.4%, N = 1.4% Biochars: S = 3.8 m^2/g	MB	-	Langmuir model	310.115 mg/g [a] Biochars: 6.780 mg/g [a]	PSO	6 h	Electrostatic interaction and ion exchange	[188]
N-doped biochars	P, BM: biochars (1.8 g) + $NH_3 \cdot H_2O$ (18 mL), agate balls (Φ = 6 mm, 180 g), RS = 300 rpm, MT = 12 h, RT = 3 h	S = 441–548 m^2/g, V = 0.302–0.415 cm^3/g, V_{micro} = 0.171–0.215 cm^3/g, D = 2.55–3.34 nm, C = 89.2–94.6%, O = 4.51–9.10%, N = 0.87–1.68%	RR	T = 25 $\pm$ 2 °C	-	22.0–37.4 mg/g [c]	-	-	Electrostatic interaction	[90]
Thiol-modified biochars	BM: biochars (2 g) + 3-trimethoxysilyl-propanethiol (1.6 mL with strong nitrogen purging) + water (2.4 mL) + ethanol (76 mL) + NH_4O, agate balls (Φ = 3, 5, 15mm, 200 g, MR = 3:5:2), RS = 400 rpm, MT = 30 h, TA = 6 h	S = 56.05–458.94 m^2/g, V = 0.271–0.635 cm^3/g, D = 5.53–19.34 nm, C = 59.15–71.24%, O = 18.45–27.95%, N = 0–2.25%, S = 2.98–5.63%, Si = 7.03–10.77%, O/C = 0.259–0.473, pH_{pzc} < 2. BM-BCs: S = 3.78–385.80 m^2/g, V = 0.0163–0.182 cm^3/g; D = 2.59–17.22 nm, C = 73.12–87.49%, O = 12.51–25.88%, Si = 1–1.00%, O/C = 0.143–0.354, pH_{pzc} < 2	MeHg	T = 25 °C, pH = 7.0 $\pm$ 0.2	Langmuir model	39.14 $\pm$ 1.46–108.16 $\pm$ 3.11 mg/g [a] BM-BCs: 19.53 $\pm$ 1.03–25.54 $\pm$ 4.12 mg/g [a]	PSO	24 h Ball-milled biochar: 9 h	Surface adsorption, electrostatic attraction, surface complexation, and ligand exchange	[55]

Table 2. *Cont.*

Materials	Treatment	Material Characterization	Pollutants	Experimental Condition	Isotherm Model	Adsorption Experiment Adsorption Capacity	Kinetic Model	Equilibrium Time	Adsorption Mechanism	Ref.
BM-FeS@NBCs	BM: biochars (1 g) + $NH_3 \cdot H_2O$ (15 g), agate balls (Φ = 15, 10, 6 mm, 45 g, MR = 2:20:22), RS = 300 rpm, MT = 12 h, TA = 3 h, N_2 purging for 30 min BM: N-biochars (1 g) + FeS (0.5 g), agate balls (Φ = 15, 10, 6 mm, 27 g, MR = 1:10:11), RS = 300 rpm, MT = 12 h, TA = 3 h, N_2 purging for 30 min	pH_{pzc} = 3.9	TC	T = 15–25 °C	Langmuir model	174.82–371.29 mg/g [a]	Avrami fractional-order model	350 min	Pore filling, hydrogen bonding, and π–π stacking interactions	[10]
MBCs	P, BM: biochars (0.45 g) + Fe_3O_4 (1.35 g), agate balls (Φ = 6 mm, 180 g), RS = 500 rpm, MT = 12 h	S = 362.4 m^2/g, V = 0.09 cm^3/g, D = 3.82 nm, APS = 482 nm, C = 49.5%, H = 1.29%, O = 19.7%, N = 0.04%, Fe = 20.3%, pH_{pzc} < 3, MS = 34.9 emu/g Biochars: S = 227.4 m^2/g, V = 0.14 cm^3/g, D = 2.09 nm, APS = 0.5–1 mm, C = 83.5%, H = 2.73%, O = 4.9%, N = 0.27%, Fe = 0.02%, pH_{pzc} < 3. BM-BCs: S = 319.1 m^2/g, V = 0.23 cm^3/g, D = 2.82 nm, APS = 335 nm, C = 73.7%, H = 3.38%, O = 14.0%, N = 0.18%, Fe = 0.03%, pH_{pzc} < 3	MB	T = 25 ± 2 °C	Langmuir model	500.5 mg/g [a]	PSO	8 h	π electronic interaction, electrostatic attraction, and/or ion exchange	[104]

Table 2. *Cont.*

Materials	Treatment	Material Characterization	Pollutants	Experimental Condition	Isotherm Model	Adsorption Experiment Adsorption Capacity	Kinetic Model	Equilibrium Time	Adsorption Mechanism	Ref.
BM-Fe$_3$O$_4$-BC	P, BM: biochars + Fe$_3$O$_4$ (MS = 1:100), agate balls (Φ = 6, 10, and 15 mm), MM = 1:2, RS = 500 rpm, MT = 12 h, TA = 3 h	S = 10.1178 m^2/g, V = 0.0015 cm^3/g, pH$_{pzc}$ = 5.3, MS = 5.29 emu/g Biochars: S = 82.10 m^2/g	TC	T = 10–50 °C	Langmuir model	102.91–237.51 mg/g [a]	Avrami fractional-order model	100 min	Pore filling, hydrogen bonding, and π–π stacking	[174]
Fe@MBC	V, BM: biochars + FeCl$_3$, MM = 1: 9, RS = 400 rpm, MT = 130 min, RT = 60 min RP = 10 min, T = 3, air atmosphere	S = 17.19 m^2/g, V = 0.13 cm^3/g, D = 28.91 nm Biochars: S = 166.95 m^2/g, V = 0.07 cm^3/g, D = 1.63 nm BM-BCs: S = 219.24 m^2/g, V = 0.30 cm^3/g, D = 5.26 nm	TC	T = 25 °C	Freundlich Model BM-BCs: Langmuir model	24.58 mg$^{1-1/n}$·L$^{1/n}$·g^{-1} [b] BM-BCs: 41.08 mg/g [a]	PSO	24 h	Ion exchange, π–π stacking, van der Waals forces, electrostatic interactions, and hydrogen bonding	[189]
CuO-biochars	P, BM: biochars (1.8 g) + CuO (0.018 g), agate balls (90 g), RS = 400 rpm, MT = 9 h, RT = 1.5 h, air atmosphere	S = 296.5 m^2/g, V = 0.111 cm^3/g, CuO size = 11.4 nm, C = 80.96%, O = 13.25%, Ca = 0.91%, K = 0.29%, Cu = 4.60%, pH$_{zp}$ $\approx$ 3.0	RR	T= 25 °C	Freundlich model	4.01 mg$^{(1-n)}$ L^n g^{-1} [b]	PSO	3 h	Electrostatic attraction	[96]
Twice-milled magnetic biochars	BM: biomass BM: MBC (1.0 g), RS = 400 rpm, MT = 1 h	S = 139.1 m^2/g, AFGs = 0.582 mmol/g, carboxyl = 0.194 mmol/g, lactonic groups = 0.028 mmol/g, phenolic hydroxyl = 0.360 mmol/g, pH$_{pzc}$ $\approx$ 3.9	MB	T = 25 $\pm$ 1 °C	Freundlich model	78.96 (mg/g)(L/mg)$^{1/n}$ [b]	PSO	24 h	π–π and electrostatic interactions	[190]

Table 2. *Cont.*

Materials	Treatment	Material Characterization	Pollutants	Experimental Condition	Isotherm Model	Adsorption Experiment Adsorption Capacity	Kinetic Model	Equilibrium Time	Adsorption Mechanism	Ref.
Ball-milled CNTs-based materials										
Ball-milled CNTs	P, BM: CNTs (1–2 g), agate balls (Φ = 18, 12, and 6 mm, MR = 1:10:25), RS = 160 rpm, MT = 12–50 h	S = 213–220 m^2/g, mean length = 100–800 nm, open end, none, and few tangled phenomena CNTs: S = 198 m^2/g, mean length > μm, closed-end, serious tangled phenomena	Aniline	-	-	22.2–36.2 mg/g [c] CNTs: 14.9 mg/g [c]	-	-	Capillary adsorption	[191]
Ball-milled CNTs	P, BM: CNTs, milling balls, RS = 140 rpm, T = 6–30 h	Even length = 100–200 nm tens of micron, open tube tips, clearly reduced tangled phenomena, D = 9–15 nm CNTs: even length = tens of microns, closed tube tips, serious tangled phenomena, D = 30 nm	Nitrobenzene	-	-	24.4–41.5 mg/g [c] CNTs: 19.8 mg/g [c]	-	24 h	Capillary adsorption	[113]
Ball-milled carbon/CNTs	P, BM: carbon/CNTs, stainless steel balls (Φ = 3 mm), MM = 1:12, MT = 3 h	S = 358 m^2/g, APS = ~500 nm CNTs: S = 78 m^2/g	Sodium fluoride	T = 323 K, pH = 2	Langmuir model	0.36 mg/g [a]	PSO	3.5 h	Physical adsorption and ion exchange	[192]
Ball-milled graphene-based materials										
ECG	P, BM: graphite, stainless steel balls (Φ = 10 mm), MM = 1:7, RS = 600 rpm, MT = 4 and 8 h	S = 316.47–387.69 m^2/g, V = 0.46–0.55 cm^3/g, APS = 95 ± 5.27–164 ± 8.67 nm, O = 9.37–25.17%, pH_{pzc} < 4.0 Graphite: S = 7.84 m^2/g, V = 0.03 cm^3/g	MB RB MO CV	T = 27.6 °C, pH = 4–10	-	97.7 ± 2–99.7 ± 0.2% [c]	-	20 min	Physical absorption and electrostatic interaction	[125]

Table 2. *Cont.*

Materials	Treatment	Material Characterization	Pollutants	Experimental Condition	Isotherm Model	Adsorption Experiment Adsorption Capacity	Kinetic Model	Equilibrium Time	Adsorption Mechanism	Ref.
Ni-MOF-GO	BM: GO + nickel acetate + 1,3,5-trimesic acid, stainless steel balls (560 g), RS = 235 rpm, MT = 30 min	S = 69.36 m^2/g	CR	T = 298–318 K, pH = 4–10	Freundlich model	211.55–385.65 mg/g(L/mg)$^{1/n}$ [b]	PSO	-	Lewis acid–base interaction and ion exchange	[131]
Al–carbon composites	P, BM: ZVAls (5 g) + NaCl (0.1 g) + ACs (0.05–0.5 g), ZrO$_2$ balls (Φ = 5, 8 and 10 mm, 300 g, MR = 6: 3:1), RS = 300 rpm, MT = 1 h	S = 10.400 m^2/g, Al = 44.05%, O = 10.42%, C = 44.49%, Na = 0.49%, Cl = 0.56% ZVAl: S = 3.099 m^2/g, Al = 66.03%, O = 4.21%, C = 29.75%	Hexabromo-cyclododecane	T = 25 $\pm$ 1 °C, pH = 6.2	-	>90% [c]	-	1 h	-	[164]

Notes: P: planetary ball mills; V: ultrafine vibration ball mills; DW: deionized water; Φ: ball diameter; MR: mass ratio; MM: ratios of materials to balls; RS: rotate speed; MT: milling time; TA: time of alteration rotation direction; RP: a rest period; T: times; S: surface area; V: pore volume; APS: average particle size; D: average pore diameter; AFGs: acidic functional groups; OFGs: oxygen functional groups; CEC: cation exchange capacity; TAG: total acidic group; pHpzc: point of zero charge; MS: values of saturation magnetization; [a]: maximum adsorption amounts obtained from adsorption isotherm parameters; [b]: values obtained from Freundlich model; [c]: adsorption amounts/adsorption rates at equilibrium; PFO: pseudo-first-order mode; PSO: pseudo-second-order mode.

5. Regeneration

Adsorbent regenerations provide realistic feasibility for sustainable adsorption removal of pollutants. The effectiveness of adsorbents is demonstrated by their capability for reuse and recycling in commercial and industrial applications, leading to a substantial reduction in manufacturing costs [195]. Therefore, regeneration performance is an important indicator for evaluating the economics of an ideal adsorbent [196]. The selection of appropriate regeneration techniques is essential to improve the desorption efficiency of contaminants. Table 3 summarizes the regeneration methods of ball-milled adsorbents. The regeneration methods are mainly categorized into ball milling and thermal and solvent regeneration.

Table 3. Regeneration study of eluents by different adsorbents.

Materials	Pollutants	Regeneration Method		Reusability	Ref.
BM-SnZVI@BC	Phosphorus	Ball milling regeneration	Ball milling adsorbents again	The removal rate of phosphate was 91.6% by ball milling adsorbents again, and the removal rate still reached 80.4% after five cycles.	[106]
Mechanically activated ZVAl particles	Cr(VI)		Ball milling adsorbents again	The Cr(VI) removal was restored to 100% by ball milling ZVAls again.	[162]
ZVAls/NiFe$_2$O$_4$	Cr(VI)		Ball milling adsorbents again with additional amount of NiFe$_2$O$_4$	The Cr(VI) removal was restored to 100% after the second ball milling of materials.	[161]
ZVAls/Fe$_3$O$_4$	Cr(VI)		Ball milling adsorbents again with additional amount of magnetic powders.	The removal efficiency of Cr(VI) was restored by ball milling ZVAl/Fe$_3$O$_4$ with magnetic powders again.	[34]
ZVIs/AC	Cr(VI)		Ball milling adsorbents again with additional amount of ACs.	The efficiency of Cr(VI) removal could almost be recovered completely by ball milling ZVI/AC with a small amount of ACs.	[8]
Graphite-like biochars	IMI SUL	Thermal regeneration	Pyrolysis at 500 °C for 2 h under N$_2$ atmosphere	The adsorption capacities of IMI and SUL decreased to 85.6–88.3% and 86.7–89.7% of the initial adsorption capacities, respectively, after the fifth cycle.	[33]
HGO	Cr(VI)	Thermal regeneration combined with solvents	1.0 M NaOH and calcination at 400 °C for 1 h	There was 100% retention of its initial performance in further adsorption studies.	[127]
HACs	Cr(VI)	Solvent regeneration	0.1 M H$_2$SO$_4$	The removal efficiency of Cr(VI) increased from 92.2% to 96.3% after acid regeneration.	[9]
PFBCs	U(VI)		0.6 M HCl	The adsorption capacity of U(VI) decreased by about 33.25% within six cycles.	[89]
			0.1 M Na$_2$CO$_3$	The adsorption capacity of U(VI) decreased by about 21.6%, respectively, within six cycles.	

Table 3. *Cont.*

Materials	Pollutants	Regeneration Method	Reusability	Ref.
Fe/Mn-BCs	Cd(II)	0.1 M HCl	The adsorption capacity maintained 41–70% of the first adsorption capacity after five cycles.	[175]
BM-Fe$_3$O$_4$-BC	Pb(II)	0.5 M NaOH	The adsorption capacity decreased by only 21.14% after three cycles.	[174]
	TC	Anhydrous ethanol	The desorption rate was still above 45.41% after three cycles.	
MgO-biochars	Ni(II)	0.01 M EDTA-2Na	The adsorption capacity remained at ∼80% in the 4th cycle and remained stable after that.	[172]
Fe@MBC	TC	0.1 M NaOH	The adsorption rate decreased from 84.56% to 78.43% after the third cycle.	[189]
Mg/Al-BCs	TC	0.1 M NaOH	The adsorption amount was 54.5 mg/g after the fifth cycle, which was 91.4% of the original adsorption capacity.	[194]
BM-LDOs-BC	CIP	NaOH	The adsorption capacity was still about 50 mg/g after five cycles, which accounted for 83% of the original adsorption capacity.	[186]
Ball-milling iron-loaded biochars	RR	1.0 M NaOH	The adsorption capacities were 47.9 and 54.6 mg/g at pH of 3 and 7.5, respectively, after the third cycle.	[193]
BM-PASBCs	SMX	0.1 M NaOH	The adsorption capacities were 95.3% of the initial adsorption capacities after five cycles.	[84]
BC-SBCs	SMX	0.1M NaOH	The adsorption ability could reach 98.5% of the original amount after five cycles.	[185]
BM-PBCs	Cr(VI) TC	1.0 M NaOH	The desorption efficiencies for Cr (VI) and TC were above 72.6–73.5% and 58.8–65.0% after four cycles.	[171]
BM-BCs	TC Hg(II)	0.2 M NaOH 0.5 M Na$_2$S	The adsorption amounts of TC and Hg(II) were approximately 90.55 and 87.36 mg/g, respectively, after five cycles.	[170]
BM-BCs	Pb(II) MB	0.1 M HNO$_3$ 0.1 M HCl	The adsorption efficiency of Pb(II) and MB remained about 85% after five cycles.	[167]
AC-COOH	MB CV	1.0 M HCl, 1.0 M NaOH, and water (1/1/1, *v/v/v*)	The adsorption capabilities of MB and CV decreased after each cycle.	[77]
Magnetic ACs	PFCs	Methanol	In the first three adsorption cycles, the adsorption amount decreased slightly (from 0.66 mmol/g to 0.53 mmol/g) and then remained stable.	[180]
MBCs	MB	Anhydrous ethanol	The adsorption rates were 90.1%, 86.7%, 84.8%, 82.3%, and 81.9%, respectively, in the five cycles.	[104]
Twice-milled magnetic biochars	MB	Ethanol	There was only a slight drop in the adsorption capacity after four cycles.	[190]

Ball milling is one of the useful methods of regeneration, which destroys the oxide layer on the surface and exposes the adsorption sites of materials. The depletion of ZVls, the formation of Fe-oxides, and the precipitation of $FePO_4$ inhibited adsorption. Ball milling could break the oxide shell on the iron particles, expose fresh ZVls, and improve the removal rate of phosphorus [106]. The removal rates of Cr(VI) by ZVAls and $ZVAls/NiFe_2O_4$ could be restored after ball milling of materials again [161,162], while the Cr(VI) uptakes by $ZVAls/Fe_3O_4$ and ZVIs/AC could be recovered by ball milling target materials with magnetic powders and ACs, respectively [8,34].

Thermal regeneration is applied to degrade absorbed pollutants at high temperatures to restore materials' adsorption performance. Zhang et al. [33] implied that the adsorption capacities of IMI and SUL by graphite-like biochars maintained 85.6–88.3% and 86.7–89.7% of the initial adsorption capacities, respectively, after the fifth cycle. Solvent and calcination were combined to regenerate HGO [127]. HGO was firstly washed with NaOH solution and then pyrolyzated at 400 °C for 1 h. There was almost 100% retention of its initial performance in further adsorption studies.

Solvent regeneration disrupts the equilibrium relationship among adsorbents, solvents, and adsorbates, facilitating the desorption of adsorbates from adsorbents. The commonly used solvents in regeneration studies include acid solution, alkaline solution, and organic solvents. The $Cr(OH)_3$(s) on the pores and surface of highly surface-activated carbon could be removed by H_2SO_4 solution, which slightly enhanced the adsorption performance by creating free paths for diffusion and further Cr(VI) adsorption [9]. HCl (0.6 M) and Na_2CO_3 (0.1M) solution could desorb enriched U(VI) on PFBCs effectively, and the adsorption capacity of U(VI) decreased by about 33.25% and 21.6%, respectively, after six cycles [89]. The alkaline solution, organic solvents, and their mixture could desorb target pollutants from ball-milled adsorbents for reuse. NaOH solution is the commonly used alkaline solvent and successfully regenerated $BM-Fe_3O_4$-BC [174], Mg/Al-BCs [194], BM-LDOs-BCs [186], ball-milling iron-loaded biochars [193], BM-PASBCs [84], BC-SBCs [185], BM-PBCs [171], and BM-BCs [170], respectively. These results showed that there was no significant variation or a decrease in adsorptive removal rates after several adsorption–desorption cycles, which was associated with the loss and non-renewable of adsorption sites in the regeneration cycle. When ethanol was used as a regenerating solvent, there was only a slight decrease for several adsorption–desorption cycles reported on the PFCs and MB removal by magnetic ACs [180], MBCs [104], twice-milled magnetic biochars [190], respectively, indicating that these adsorbents were reusable.

In conclusion, all ball milling, thermal, and solvent methods can regenerate adsorbents, although a loss of adsorption sites during solvent regeneration may result in a slight reduction in the uptake of some organic pollutants. Most adsorbents had suitable recycling performances over 3–5 cycles, demonstrating significant potential for practical applications.

6. Conclusions and Future Prospects

This review summarized the latest development on ball-milled materials and their application for aqueous pollutants adsorptive removal. It is concluded that ball milling is able to change the specific surface area and pore volumes of materials, reduce particle sizes even to nanoscales, introduce functional groups to the surface of materials, and expose more active sites. The adsorption amounts of inorganic and organic pollutants were improved by ball-milled materials, and some studies implied that equilibrium time was shortened. The majority of experimental data for pollutant adsorption agreed with the Langmuir model and pseudo-second-order model. The governing mechanisms for inorganic pollutants adsorption by ball-milled materials were physical adsorption, electrostatic interaction, complexation, ion exchange, precipitation, cation–π interaction, ligand exchange, coordination, or their combined effects. The physical adsorption, electrostatic interaction, H-bonding, cation interaction, π–π effect, hydrophobic interaction, Lewis acid–base interaction, ion exchange, or their combined effects contributed to organic pollutants removal on ball-milled materials. Ball milling, thermal, and solvent methods were employed to regenerate

ball-milled adsorbents. Despite the above significant progress, substantial efforts are still needed for the further development of ball-milled materials and their application in water purification. It is critical to carry out further investigation on the correlations between the synthesis parameters of ball milling and the physicochemical properties of materials since it is the foundation of ball-milled materials' customized conception for selective removal of aqueous contaminants. Although the ecological risk assessment of ball-milled materials is seldom involved in current research, it is urgent to ensure the safety of ball-milled materials before their practical use, considering stability, toxicity, and functional group leaching. The current ball-milled materials are prepared in the laboratory-scale investigation. Large-scale production and even industrial production need to be considered, as well as the balance between economic costs and technical applications for sustainable development. The adsorption experiments about pollutant captures are carried out at the "mg/L" level, which is higher than that in an actual water environment. Therefore, the adsorption performance of pollutants by ball-milled materials in real-life applications needs to be investigated. Furthermore, more emphasis should be placed on a sound life-cycle analysis and risk assessment system of ball-milled materials and their application to pollutant adsorption.

Author Contributions: P.G.: Conceptualization, methodology, visualization, data curation, writing—original draft, project administration. X.F.: Data curation, visualization, investigation, writing—original draft. D.S.: Supervision, writing—review and editing, project administration. G.Z.: Data curation, writing—review and editing. Q.W. (Quanfeng Wang): Data curation, writing—review and editing. Q.W. (Qihui Wang): Investigation, data curation. All authors have read and agreed to the published version of the manuscript.

Data Availability Statement: Data are contained within the article.

Conflicts of Interest: The authors declare no conflicts of interest.

Abbreviations

ACs: Activated carbons; CNTs: Carbon nanotubes; ZVIs: Zero-valent irons; ZVAls: Zero-valent aluminums; BM-ACs: Ball-milled activated carbons; AC-COOH: Carboxylic groups-modified ACs; ZVIs-ACs: Ball-milled iron-carbon composites; HACs: Highly surface ACs; MBCs: Magnetic biochars; BM-SnZVI@BC: Sulfur-doped nano zero-valent iron–biochar composites; BM-FeS@NBCs: N-doped biochars loaded with ferrous sulfide; LDHs: Layered double hydroxides; Mg/Al-BCs: Mg/Al hydroxides-modified biochars; BM-LDH-BCs: Ball-milled layered double hydroxides biochar composites; ZVIs-BCs: Iron–biochar composites; SWCNTs: Single-walled carbon nanotubes; MWCNTs: Multi-walled carbon nanotubes; HA-MWCNTs: Humic acid-coated MWCNTs; CeO_2-CNTs: Ceria nanoparticles supported on aligned carbon nanotubes; ECG: Edge-carboxylate graphenes; HGO: A novel holey graphene architecture; PGO: Phosphonic graphene derivatives; BM-BCs: Ball-milled biochars; BM-NBBCs: Ball-milled nitrogenous bone biochars; BM-PBCs: Ball milling potassium ferrate-activated biochars; BM-PASBCs: Phosphoric acid hydrothermally co-functionalized sludge biochars; 3-MPTS: 3-trimethoxysilylpropanethiol; BM-MBC: Ball-milled magnetic biochars; BM-Fe-BCs: Ball-milled biochar/iron oxide composites; BM-Fe_3O_4-BC: Ball-milled Fe_3O_4-modified biochars; FeS_2-BCs: FeS_2-modified biochars; Fe/Mn-BCs: Fe/Mn oxide–biochar nanocomposites; PFBCs: Phosphorous-functionalized biochars; LS-ZVIs: Lignosulfonate-modified zero-valent irons; MB: Methylene blue; CV: Crystal violet; PFCs: Perfluorinated compounds; IMI: imidacloprid; SUL: sulfadiazine; BCs-CBM: biochars derived from cellulosic biomass and montmorillonite; TC: Tetracycline hydrochloride; PWNBCs: Pine-wood-derived nanobiochars; CBZ: Carbamazepine; SMX: Sulfamethoxazole; CIP: Ciprofloxacin; BC-SBCs: Ball milling and magnetization co-modified sludge-

derived biochars; BM-LDOs-BCs: Fe-Mg-layered double oxides bagasse biochars; RR: Reactive red; Fe@MBC: Iron-containing biochars; Ni-MOF-GO: Nickel-based metal–organic framework/graphene oxide composites; CR: Congo red; TY: Titan yellow; RB: Rhodamine B; MO: Methyl orange.

References

1. Li, Q.; Chen, Z.; Wang, H.; Yang, H.; Wen, T.; Wang, S.; Hu, B.; Wang, X. Removal of organic compounds by nanoscale zero-valent iron and its composites. *Sci. Total Environ.* **2021**, *792*, 148546. [CrossRef]
2. Tang, H.; Wang, J.; Zhang, S.; Pang, H.; Wang, X.; Chen, Z.; Li, M.; Song, G.; Qiu, M.; Yu, S. Recent advances in nanoscale zero-valent iron-based materials: Characteristics, environmental remediation and challenges. *J. Clean. Prod.* **2021**, *319*, 128641. [CrossRef]
3. Gong, Y.; Wang, Y.; Lin, N.; Wang, R.; Wang, M.; Zhang, X. Iron-based materials for simultaneous removal of heavy metal(loid)s and emerging organic contaminants from the aquatic environment: Recent advances and perspectives. *Environ. Pollut.* **2022**, *299*, 118871. [CrossRef] [PubMed]
4. Rahaman, M.S.; Rahman, M.M.; Mise, N.; Sikder, M.T.; Ichihara, G.; Uddin, M.K.; Kurasaki, M.; Ichihara, S. Environmental arsenic exposure and its contribution to human diseases, toxicity mechanism and management. *Environ. Pollut.* **2021**, *289*, 117940. [CrossRef] [PubMed]
5. Genchi, G.; Sinicropi, M.S.; Lauria, G.; Carocci, A.; Catalano, A. The effects of cadmium toxicity. *Int. J. Environ. Res. Public Health* **2020**, *17*, 3782. [CrossRef]
6. Shi, Y.; Chang, Q.; Zhang, T.; Song, G.; Sun, Y.; Ding, G. A review on selective dye adsorption by different mechanisms. *J. Environ. Chem. Eng.* **2022**, *10*, 108639. [CrossRef]
7. Mathur, P.; Sanyal, D.; Callahan, D.L.; Conlan, X.A.; Pfeffer, F.M. Treatment technologies to mitigate the harmful effects of recalcitrant fluoroquinolone antibiotics on the environ- ment and human health. *Environ. Pollut.* **2021**, *291*, 118233. [CrossRef]
8. Wang, W.; Hu, B.; Wang, C.; Liang, Z.; Cui, F.; Zhao, Z.; Yang, C. Cr(VI) removal by micron-scale iron-carbon composite induced by ball milling: The role of activated carbon. *Chem. Eng. J.* **2020**, *389*, 122633. [CrossRef]
9. Fang, Y.; Yang, K.; Zhang, Y.; Peng, C.; Robledo-Cabrera, A.; Lopez-Valdivieso, A. Highly surface activated carbon to remove Cr(VI) from aqueous solution with adsorbent recycling. *Environ. Res.* **2021**, *197*, 111151. [CrossRef]
10. Qu, J.; Zhang, W.; Bi, F.; Yan, S.; Miao, X.; Zhang, B.; Wang, Y.; Ge, C.; Zhang, Y. Two-step ball milling-assisted synthesis of N-doped biochar loaded with ferrous sulfide for enhanced adsorptive removal of Cr(VI) and tetracycline from water. *Environ. Pollut.* **2022**, *306*, 119398. [CrossRef]
11. Kishore, S.; Malik, S.; Shah, M.P.; Bora, J.; Chaudhary, V.; Kumar, L.; Sayyed, R.Z.; Ranjan, A. A comprehensive review on removal of pollutants from wastewater through microbial nanobiotechnology-based solutions. *Biotechnol. Genet.* **2022**, 1–26. [CrossRef]
12. Bhatt, P.; Bhandari, G.; Bhatt, K.; Simsek, H. Microalgae-based removal of pollutants from wastewaters: Occurrence, toxicity and circular economy. *Chemosphere* **2022**, *306*, 135576. [CrossRef] [PubMed]
13. Titchou, F.E.; Zazou, H.; Afanga, H.; El Gaayda, J.; Akbour, R.A.; Nidheesh, P.V.; Hamdani, M. Removal of organic pollutants from wastewater by advanced oxidation processes and its combination with membrane processes. *Chem. Eng. Process.* **2021**, *169*, 108631. [CrossRef]
14. Zhang, Y.; Zhao, Y.-G.; Maqbool, F.; Hu, Y. Removal of antibiotics pollutants in wastewater by uv-based advanced oxidation processes: Influence of water matrix components, processes optimization and application: A review. *J. Water Process. Eng.* **2022**, *45*, 102496. [CrossRef]
15. Oluwole, A.O.; Omotola, E.O.; Olatunji, O.S. Pharmaceuticals and personal care products in water and wastewater: A review of treatment processes and use of photocatalyst immobilized on functionalized carbon in aop degradation. *BMC Chem.* **2020**, *14*, 62. [CrossRef]
16. Baig, U.; Faizan, M.; Sajid, M. Multifunctional membranes with super-wetting characteristics for oil-water separation and removal of hazardous environmental pollutants from water: A review. *Adv. Colloid Interface Sci.* **2020**, *285*, 102276. [CrossRef] [PubMed]
17. Xie, J.; Liao, Z.; Zhang, M.; Ni, L.; Qi, J.; Wang, C.; Sun, X.; Wang, L.; Wang, S.; Li, J. Sequential ultrafiltration-catalysis membrane for excellent removal of multiple pollutants in water. *Environ. Sci. Technol.* **2021**, *55*, 2652–2661. [CrossRef]
18. Obotey Ezugbe, E.; Rathilal, S. Membrane technologies in wastewater treatment: A review. *Membranes* **2020**, *10*, 89. [CrossRef]
19. Salman, M.S.; Hasan, M.N.; Hasan, M.M.; Kubra, K.T.; Sheikh, M.C.; Rehan, A.I.; Waliullah, R.M.; Rasee, A.I.; Awual, M.E.; Hossain, M.S.; et al. Improving copper(II) ion detection and adsorption from wastewater by the ligand-functionalized composite adsorbent. *J. Mol. Struct.* **2023**, *1282*, 135259. [CrossRef]
20. Qu, J.; Shi, J.; Wang, Y.; Tong, H.; Zhu, Y.; Xu, L.; Wang, Y.; Zhang, B.; Tao, Y.; Dai, X.; et al. Applications of functionalized magnetic biochar in environmental remediation: A review. *J. Hazard. Mater.* **2022**, *434*, 128841. [CrossRef]
21. Ahmed, M.J.; Hameed, B.H. Insight into the co-pyrolysis of different blended feedstocks to biochar for the adsorption of organic and inorganic pollutants: A review. *J. Clean. Prod.* **2020**, *265*, 121762. [CrossRef]
22. Chen, Z.; Wei, W.; Chen, H.; Ni, B.J. Recent advances in waste-derived functional materials for wastewater remediation. *Eco-Environ. Health* **2022**, *1*, 86–104. [CrossRef] [PubMed]

23. Wang, Q.; Sun, H.; Wu, S.; Pan, S.; Cui, D.; Wu, D.; Xu, F.; Wang, Z. Production of biomass-based carbon materials in hydrothermal media: A review of process parameters, activation treatments and practical applications. *J. Energy Inst.* **2023**, *110*, 101357. [CrossRef]

24. Li, S.; Deng, J.; Xiong, L.; Wang, J.; Chen, Y.; Jiao, Y.; Jiang, L.; Dan, Y. Design and construct CeO_2-ZrO_2-Al_2O_3 materials with controlled structures via co-precipitation method by using different precipitants. *Ceram. Int.* **2018**, *44*, 20929–20938. [CrossRef]

25. Zhao, H.; Lang, Y. Adsorption behaviors and mechanisms of florfenicol by magnetic functionalized biochar and reed biochar. *J. Taiwan Inst. Chem. Eng.* **2018**, *88*, 152–160. [CrossRef]

26. Gong, L.; Qiu, X.; Tratnyek, P.G.; Liu, C.; He, F. FeN_x(C)-coated microscale zero-valent iron for fast and stable trichloroethylene dechlorination in both acidic and basic pH conditions. *Environ. Sci. Technol.* **2021**, *55*, 5393–5402. [CrossRef] [PubMed]

27. Wang, P.; Hu, J.; Wang, Y.; Liu, T. Enhanced elimination of V^{5+} in wastewater using zero-valent iron activated by ball milling: The overlooked crucial roles of energy input and sodium chloride. *J. Hazard. Mater.* **2022**, *435*, 129050. [CrossRef] [PubMed]

28. Yang, X.; Liu, S.; Liang, T.; Yan, X.; Zhang, Y.; Zhou, Y.; Sarkar, B.; Ok, Y.S. Ball-milled magnetite for efficient arsenic decontamination: Insights into oxidation-adsorption mechanism. *J. Hazard. Mater.* **2022**, *427*, 128117. [CrossRef] [PubMed]

29. Gayathiri, M.; Pulingam, T.; Lee, K.T.; Sudesh, K. Activated carbon from biomass waste precursors: Factors affecting production and adsorption mechanism. *Chemosphere* **2022**, *294*, 133764. [CrossRef]

30. Jiang, B.; Lin, Y.; Mbog, J.C. Biochar derived from swine manure digestate and applied on the removals of heavy metals and antibiotics. *Bioresour. Technol.* **2018**, *270*, 603–611. [CrossRef]

31. Soares, O.S.G.P.; Gonçalves, A.G.; Delgado, J.J.; Órfão, J.J.M.; Pereira, M.F.R. Modification of carbon nanotubes by ball-milling to be used as ozonation catalysts. *Catal. Today* **2015**, *249*, 199–203. [CrossRef]

32. Wang, Z.S.; Wang, Y.; Liao, J.L.; Yang, Y.Y.; Liu, N.; Tang, J. Improving the adsorption ability of graphene sheets to uranium through chemical oxidation, electrolysis and ball-milling. *J. Radioanal. Nucl. Chem.* **2016**, *308*, 1095–1102. [CrossRef]

33. Zhang, P.; Wang, X.; Xue, B.; Huang, P.; Hao, Y.; Tang, J.; Maletić, S.P.; Rončević, S.D.; Sun, H. Preparation of graphite-like biochars derived from straw and newspaper based on ball-milling and tempo-mediated oxidation and their supersorption performances to imidacloprid and sulfadiazine. *Chem. Eng. J.* **2021**, *411*, 128502. [CrossRef]

34. Wang, W.; Gao, P.; Yang, C.; Zhao, Z.; Zhen, S.; Zhou, Y.; Zhang, T. Separable and reactivated magnetic $mZVAl/nFe_3O_4$ composite induced by ball milling for efficient adsorption-reduction- sequestration of aqueous Cr(VI). *Sep. Purif. Technol.* **2022**, *288*, 120689. [CrossRef]

35. Kumar, M.; Xiong, X.; Wan, Z.; Sun, Y.; Tsang, D.C.W.; Gupta, J.; Gao, B.; Cao, X.; Tang, J.; Ok, Y.S. Ball milling as a mechanochemical technology for fabrication of novel biochar nanomaterials. *Bioresour. Technol.* **2020**, *312*, 123613. [CrossRef]

36. Amusat, S.O.; Kebede, T.G.; Dube, S.; Nindi, M.M. Ball-milling synthesis of biochar and biochar–based nanocomposites and prospects for removal of emerging contaminants: A review. *J. Water Process. Eng.* **2021**, *41*, 101993. [CrossRef]

37. Hu, Y.; Li, B.; Yu, C.; Fang, H.; Li, Z. Mechanochemical preparation of single atom catalysts for versatile catalytic applications: A perspective review. *Mater. Today* **2023**, *63*, 288–312. [CrossRef]

38. Zhao, L.Y.; Dong, X.L.; Lu, A.H. Mechanochemical synthesis of porous carbons and their applications in catalysis. *ChemPlusChem* **2020**, *85*, 866–875. [CrossRef]

39. Yin, Z.; Zhang, Q.; Li, S.; Cagnetta, G.; Huang, J.; Deng, S.; Yu, G. Mechanochemical synthesis of catalysts and reagents for water decontamination: Recent advances and perspective. *Sci. Total Environ.* **2022**, *825*, 153992. [CrossRef]

40. Wang, P.; Hu, J.; Liu, T.; Han, G.; Ma, W.-M.; Li, J. New insights into ball-milled zero-valent iron composites for pollution remediation: An overview. *J. Clean. Prod.* **2023**, *385*, 135513. [CrossRef]

41. Wei, M.; Wang, B.; Chen, M.; Lyu, H.; Lee, X.; Wang, S.; Yu, Z.; Zhang, X. Recent advances in the treatment of contaminated soils by ball milling technology: Classification, mechanisms, and applications. *J. Clean. Prod.* **2022**, *340*, 130821. [CrossRef]

42. Balaz, P.; Achimovicova, M.; Balaz, M.; Billik, P.; Cherkezova-Zheleva, Z.; Criado, J.M.; Delogu, F.; Dutkova, E.; Gaffet, E.; Gotor, F.J.; et al. Hallmarks of mechanochemistry: From nanoparticles to technology. *Chem. Soc. Rev.* **2013**, *42*, 7571–7637. [CrossRef] [PubMed]

43. Ditenberg, I.A.; Osipov, D.A.; Smirnov, I.V.; Grinyaev, K.V.; Esikov, M.A. Effect of preliminary high-energy ball milling on the structural-phase state and microhardness of ni3al samples obtained by spark plasma sintering. *Adv. Powder Technol.* **2023**, *34*, 130919. [CrossRef]

44. Chuev, I.I.; Kovalev, D.Y. Effects of titanium high energy ball milling on the solid-phase reaction Ti+C. *Mater. Chem. Phys.* **2022**, *283*, 126025. [CrossRef]

45. Delogu, F.; Gorrasi, G.; Sorrentino, A. Fabrication of polymer nanocomposites via ball milling: Present status and future perspectives. *Prog. Mater. Sci.* **2017**, *86*, 75–126. [CrossRef]

46. Arbain, R.; Othman, M.; Palaniandy, S. Preparation of iron oxide nanoparticles by mechanical milling. *Miner. Eng.* **2011**, *24*, 1–9. [CrossRef]

47. Qian, L.; Li, H.; Wei, Z.; Liang, C.; Dong, X.; Lin, D.; Chen, M. Enhanced removal of cis-1,2-dichloroethene and vinyl chloride in groundwater using ball-milled sulfur- and biochar-modified zero-valent iron: From the laboratory to the field. *Environ. Pollut.* **2023**, *336*, 122424. [CrossRef] [PubMed]

48. Li, H.; Qian, L.; Liang, C.; Zheng, T.; Dong, X.; Chen, M. Enhanced Cr(VI) reduction by zero-valent iron and ferroferric oxide wet ball milling: Synergy of electron storage and electron transfer. *Chem. Eng. J.* **2023**, *457*, 141254. [CrossRef]

49.   Wang, X.; Yang, H.; Yu, X.; Hu, C.; Hu, J.; Li, R.; Zhang, Y. Functional metal powders: Design, properties, applications, and prospects. *Mater. Sci. Eng. B* **2022**, *280*, 115708. [CrossRef]

50.   Li, H.N.; Zhang, H.M.; Huang, K.K.; Liang, D.; Zhao, D.D.; Jiang, Z.Y. Effect of ball milling speed on the quality of Al_2O_3 stripped graphene in a wet milling medium. *Ceram. Int.* **2022**, *48*, 17171–17177. [CrossRef]

51.   Yang, Z.; Liu, J.; Yang, S.; Fan, D.; Fu, P. Graphite-modified zero-valent aluminum prepared by mechanical ball milling for selective removal of hydrophobic carbon tetrachloride. *Chem. Eng. J.* **2023**, *474*, 145591. [CrossRef]

52.   Sun, W.; Zhang, T.; Li, J.; Zhu, X. Enhanced gaseous acetone adsorption on montmorillonite by ball milling generated Si–OH and interlayer under synergistic modification with H_2O_2 and tetramethylammonium bromide. *Chemosphere* **2023**, *321*, 138114. [CrossRef] [PubMed]

53.   Yang, X.; Wang, L.; Shao, X.; Tong, J.; Zhou, J.; Feng, Y.; Chen, R.; Yang, Q.; Han, Y.; Yang, X.; et al. Characteristics and aqueous dye removal ability of novel biosorbents derived from acidic and alkaline one-step ball milling of hickory wood. *Chemosphere* **2022**, *309*, 136610. [CrossRef] [PubMed]

54.   Yang, X.; Wang, L.; Tong, J.; Shao, X.; Feng, Y.; Zhou, J.; Han, Y.; Yang, X.; Ding, F.; Zhang, J.; et al. Alkaline ball-milled peanut-hull biosorbent effectively removes aqueous organic dyes. *Chemosphere* **2023**, *313*, 137410. [CrossRef] [PubMed]

55.   Zhao, L.; Zhang, Y.; Wang, L.; Lyu, H.; Xia, S.; Tang, J. Effective removal of Hg(II) and MeHg from aqueous environment by ball milling aided thiol-modification of biochars: Effect of different pyrolysis temperatures. *Chemosphere* **2022**, *294*, 133820. [CrossRef] [PubMed]

56.   Nasrullah, A.; Khan, A.S.; Bhat, A.H.; Din, I.U.; Inayat, A.; Muhammad, N.; Bakhsh, E.M.; Khan, S.B. Effect of short time ball milling on physicochemical and adsorption performance of activated carbon prepared from mangosteen peel waste. *Renew. Energy* **2021**, *168*, 723–733. [CrossRef]

57.   Lee, S.H.; Annamalai, S.; Shin, W.S. Engineered ball-milled colloidal activated carbon material for advanced oxidation process of ibuprofen: Influencing factors and insights into the mechanism. *Environ. Pollut.* **2023**, *322*, 121023. [CrossRef] [PubMed]

58.   Bordoloi, N.; Goswami, R.; Kumar, M.; Kataki, R. Biosorption of Co(II) from aqueous solution using algal biochar: Kinetics and isotherm studies. *Bioresour. Technol.* **2017**, *244*, 1465–1469. [CrossRef]

59.   Abdelhadi, S.O.; Dosoretz, C.G.; Rytwo, G.; Gerchman, Y.; Azaizeh, H. Production of biochar from olive mill solid waste for heavy metal removal. *Bioresour. Technol.* **2017**, *244*, 759–767. [CrossRef]

60.   Wei, L.K.; Abd Rahim, S.Z.; Al Bakri Abdullah, M.M.; Yin, A.T.M.; Ghazali, M.F.; Omar, M.F.; Nemes, O.; Sandu, A.V.; Vizureanu, P.; Abdellah, A.E. Producing metal powder from machining chips using ball milling process: A review. *Materials* **2023**, *16*, 4635. [CrossRef]

61.   Zhang, F.; Han, F.; Lu, Y.; Wen, G.; Gu, S.; Wang, Z.; Tang, P. Experimental study and numerical simulation of the influence of ball milling parameters on granule sizes of mold powder. *Powder Technol.* **2023**, *413*, 118037. [CrossRef]

62.   Burmeister, C.F.; Kwade, A. Process engineering with planetary ball mills. *Chem. Soc. Rev.* **2013**, *42*, 7660–7667. [CrossRef] [PubMed]

63.   Zhang, Q.; Saito, F. A review on mechanochemical syntheses of functional materials. *Adv. Powder Technol.* **2012**, *23*, 523–531. [CrossRef]

64.   Tucho, W.M.; Mauroy, H.; Walmsley, J.C.; Deledda, S.; Holmestad, R.; Hauback, B.C. The effects of ball milling intensity on morphology of multiwall carbon nanotubes. *Scr. Mater.* **2010**, *63*, 637–640. [CrossRef]

65.   Pierard, N.; Fonseca, A.; Colomer, J.F.; Bossuot, C.; Benoit, J.M.; Van Tendeloo, G.; Pirard, J.P.; Nagy, J.B. Ball milling effect on the structure of single-wall carbon nanotubes. *Carbon* **2004**, *42*, 1691–1697. [CrossRef]

66.   Cheng, Z.; Lyu, H.; Shen, B.; Tian, J.; Sun, Y.; Wu, C. Removal of antimonite Sb(III) from aqueous solution using a magnetic iron-modified carbon nanotubes (CNTs) composite: Experimental observations and governing mechanisms. *Chemosphere* **2022**, *288*, 132581. [CrossRef] [PubMed]

67.   Huot, J.; Cuevas, F.; Deledda, S.; Edalati, K.; Filinchuk, Y.; Grosdidier, T.; Hauback, B.C.; Heere, M.; Jensen, T.R.; Latroche, M.; et al. Mechanochemistry of metal hydrides: Recent advances. *Materials* **2019**, *12*, 2778. [CrossRef] [PubMed]

68.   Toraman, O.Y.; Katırcıoglu, D. A study on the effect of process parameters in stirred ball mill. *Adv. Powder Technol.* **2011**, *22*, 26–30. [CrossRef]

69.   Bulgakov, V.; Pascuzzi, S.; Ivanovs, S.; Kaletnik, G.; Yanovich, V. Angular oscillation model to predict the performance of a vibratory ball mill for the fine grinding of grain. *Biosyst. Eng.* **2018**, *171*, 155–164. [CrossRef]

70.   Thambiliyagodage, C.; Wijesekera, R. Ball milling—A green and sustainable technique for the preparation of titanium based materials from ilmenite. *Curr. Res. Green Sustain. Chem.* **2022**, *5*, 100236. [CrossRef]

71.   Xu, Y.; Zhang, B.; Feng, G. Electromagnetic design and thermal analysis of module combined permanent magnet motor with wrapped type for mine ball mill. *IET Electr. Power App.* **2021**, *16*, 139–157. [CrossRef]

72.   Fu, H.; Li, X.; Wang, J.; Lin, P.; Chen, C.; Zhang, X.; Suffet, I.H. Activated carbon adsorption of quinolone antibiotics in water: Performance, mechanism, and modeling. *J. Environ. Sci.* **2017**, *56*, 145–152. [CrossRef] [PubMed]

73.   Bae, S.; Kim, Y.; Kim, S.; Chung, C.M.; Cho, K. Enhanced sulfate ion adsorption selectivity in capacitive deionization with ball-milled activated carbon. *Desalination* **2022**, *540*, 116014. [CrossRef]

74.   Chen, T.; Gu, W.; Li, G.; Wang, Q.; Liang, P.; Zhang, X.; Huang, X. Significant enhancement in catalytic ozonation efficacy: From granular to super-fine powdered activated carbon. *Front. Environ. Sci. Eng.* **2017**, *12*, 6. [CrossRef]

75. Yuan, R.; Dong, Y.; Hou, R.; Shang, L.; Zhang, J.; Zhang, S.; Chen, X.; Song, H. Structural transformation of porous and disordered carbon during ball-milling. *Chem. Eng. J.* **2023**, *454*, 140418. [CrossRef]

76. Wang, L.; Chen, X.; Lu, Y.; Liu, C.; Yang, W. Carbon quantum dots displaying dual-wavelength photoluminescence and electrochemiluminescence prepared by high-energy ball milling. *Carbon* **2015**, *94*, 472–478. [CrossRef]

77. Gohr, M.; Abd-Elhamid, A.I.; El-Shanshory, A.A.; Soliman, H.M.A. Adsorption of cationic dyes onto chemically modified activated carbon: Kinetics and thermodynamic study. *J. Mol. Liq.* **2022**, *346*, 118227. [CrossRef]

78. Shan, D.; Deng, S.; Zhao, T.; Wang, B.; Wang, Y.; Huang, J.; Yu, G.; Winglee, J.; Wiesner, M.R. Preparation of ultrafine magnetic biochar and activated carbon for pharmaceutical adsorption and subsequent degradation by ball milling. *J. Hazard. Mater.* **2016**, *305*, 156–163. [CrossRef] [PubMed]

79. Chen, C.; Yang, F.; Beesley, L.; Trakal, L.; Ma, Y.; Sun, Y.; Zhang, Z.; Ding, Y. Removal of cadmium in aqueous solutions using a ball milling-assisted one-pot pyrolyzed iron-biochar composite derived from cotton husk. *Environ. Sci. Pollut. Res.* **2023**, *30*, 12571–12583. [CrossRef]

80. Naghdi, M.; Taheran, M.; Brar, S.K.; Rouissi, T.; Verma, M.; Surampalli, R.Y.; Valero, J.R. A green method for production of nanobiochar by ball milling-optimization and characterization. *J. Clean. Prod.* **2017**, *164*, 1394–1405. [CrossRef]

81. Liu, X.; Shen, F.; Qi, X. Adsorption recovery of phosphate from aqueous solution by cao-biochar composites prepared from eggshell and rice straw. *Sci. Total Environ.* **2019**, *666*, 694–702. [CrossRef] [PubMed]

82. Yang, X.; Liu, Z.; Jiang, Y.; Li, F.; Xue, B.; Dong, Z.; Ding, M.; Chen, R.; Yang, Q.; An, T.; et al. Micro-structure, surface properties and adsorption capacity of ball-milled cellulosic biomass derived biochar based mineral composites synthesized via carbon-bed pyrolysis. *Appl. Clay Sci.* **2020**, *199*, 105877. [CrossRef]

83. Xiang, W.; Wan, Y.; Zhang, X.; Tan, Z.; Xia, T.; Zheng, Y.; Gao, B. Adsorption of tetracycline hydrochloride onto ball-milled biochar: Governing factors and mechanisms. *Chemosphere* **2020**, *255*, 127057. [CrossRef] [PubMed]

84. Ma, Y.; Yao, Y.; Deng, Z.; Tang, J.; Liu, Y.; Ma, J.; Zhang, Z. Ball milling and phosphoric acid hydrothermally co-functionalized sludge biochar for efficiently adsorptive removal of environmental concentration sulfamethoxazole: Experimental, characterization and dft study. *Sep. Purif. Technol.* **2024**, *328*, 125051. [CrossRef]

85. Zou, H.; Zhao, J.; He, F.; Zhong, Z.; Huang, J.; Zheng, Y.; Zhang, Y.; Yang, Y.; Yu, F.; Bashir, M.A.; et al. Ball milling biochar iron oxide composites for the removal of chromium Cr(VI) from water: Performance and mechanisms. *J. Hazard. Mater.* **2021**, *413*, 125252. [CrossRef]

86. Lyu, H.; Gao, B.; He, F.; Zimmerman, A.R.; Ding, C.; Huang, H.; Tang, J. Effects of ball milling on the physicochemical and sorptive properties of biochar: Experimental observations and governing mechanisms. *Environ. Pollut.* **2018**, *233*, 54–63. [CrossRef] [PubMed]

87. Xu, X.; Xu, Z.; Huang, J.; Gao, B.; Zhao, L.; Qiu, H.; Cao, X. Sorption of reactive red by biochars ball milled in different atmospheres: Co-effect of surface morphology and functional groups. *Chem. Eng. J.* **2021**, *413*, 127468. [CrossRef]

88. Qi, G.; Pan, Z.; Zhang, X.; Miao, X.; Xiang, W.; Gao, B. Effect of ball milling with hydrogen peroxide or ammonia hydroxide on sorption performance of volatile organic compounds by biochar from different pyrolysis temperatures. *Chem. Eng. J.* **2022**, *450*, 138027. [CrossRef]

89. Zhou, Y.; Xiao, J.; Hu, R.; Wang, T.; Shao, X.; Chen, G.; Chen, L.; Tian, X. Engineered phosphorous-functionalized biochar with enhanced porosity using phytic acid-assisted ball milling for efficient and selective uptake of aquatic uranium. *J. Mol. Liq.* **2020**, *303*, 112659. [CrossRef]

90. Xu, X.; Zheng, Y.; Gao, B.; Cao, X. N-doped biochar synthesized by a facile ball-milling method for enhanced sorption of CO_2 and reactive red. *Chem. Eng. J.* **2019**, *368*, 564–572. [CrossRef]

91. Qu, J.; Xu, Y.; Zhang, X.; Sun, M.; Tao, Y.; Zhang, X.; Zhang, G.; Ge, C.; Zhang, Y. Ball milling-assisted preparation of N-doped biochar loaded with ferrous sulfide as persulfate activator for phenol degradation: Multiple active sites-triggered radical/non-radical mechanism. *Appl. Catal. B Environ. Energy* **2022**, *316*, 121639. [CrossRef]

92. Wu, J.; Wang, T.; Liu, Y.; Tang, W.; Geng, S.; Chen, J. Norfloxacin adsorption and subsequent degradation on ball-milling tailored N-doped biochar. *Chemosphere* **2022**, *303*, 135264. [CrossRef] [PubMed]

93. Lyu, H.; Xia, S.; Tang, J.; Zhang, Y.; Gao, B.; Shen, B. Thiol-modified biochar synthesized by a facile ball-milling method for enhanced sorption of inorganic Hg^{2+} and organicCH_3Hg. *J. Hazard. Mater.* **2020**, *384*, 121357. [CrossRef] [PubMed]

94. Zhang, P.; Bing, X.; Jiao, L.; Xiao, H.; Li, B.; Sun, H. Amelioration effects of coastal saline-alkali soil by ball-milled red phosphorus-loaded biochar. *Chem. Eng. J.* **2022**, *431*, 133904. [CrossRef]

95. Zheng, Y.; Wan, Y.; Chen, J.; Chen, H.; Gao, B. Mgo modified biochar produced through ball milling: A dual-functional adsorbent for removal of different contaminants. *Chemosphere* **2020**, *243*, 125344. [CrossRef] [PubMed]

96. Wei, X.; Wang, X.; Gao, B.; Zou, W.; Dong, L. Facile ball-milling synthesis of cuo/biochar nanocomposites for efficient removal of reactive red 120. *ACS Omega* **2020**, *5*, 5748–5755. [CrossRef] [PubMed]

97. Yu, F.; Tian, F.; Zou, H.; Ye, Z.; Peng, C.; Huang, J.; Zheng, Y.; Zhang, Y.; Yang, Y.; Wei, X.; et al. Zno/biochar nanocomposites via solvent free ball milling for enhanced adsorption and photocatalytic degradation of methylene blue. *J. Hazard. Mater.* **2021**, *415*, 125511. [CrossRef] [PubMed]

98. Quan, G.; Sui, F.; Wang, M.; Cui, L.; Wang, H.; Xiang, W.; Li, G.; Yan, J. Mechanochemical modification of biochar-attapulgite nanocomposites for cadmium removal: Performance and mechanisms. *Biochem. Eng. J.* **2022**, *179*, 108332. [CrossRef]

99. Li, F.; Wan, Y.; Chen, J.; Hu, X.; Tsang, D.C.W.; Wang, H.; Gao, B. Novel ball-milled biochar-vermiculite nanocomposites effectively adsorb aqueous As(V). *Chemosphere* **2020**, *260*, 127566. [CrossRef]

100. Tang, J.; Zhao, B.; Lyu, H.; Li, D. Development of a novel pyrite/biochar composite (BM-FeS$_2$@BC) by ball milling for aqueous Cr(VI) removal and its mechanisms. *J. Hazard. Mater.* **2021**, *413*, 125415. [CrossRef]

101. Zhao, B.; Tang, J.; Lyu, H.; Liu, F.; Wang, L. Low molecular weight organic acids strengthen the electron transfer of natural fes2/biochar composite for Cr(VI) reduction: Experimental observations and governing mechanisms. *J. Environ. Chem. Eng.* **2022**, *10*, 107181. [CrossRef]

102. Zhao, L.; Zhang, H.; Zhao, B.B.; Lyu, H.H. Activation of peroxydisulfate by ball-milled α-feooh/biochar composite for phenol removal: Component contribution and internal mechanisms. *Environ. Pollut.* **2022**, *293*, 118596. [CrossRef] [PubMed]

103. Shi, Q.; Guo, S.; Tang, J.; Lyu, H.; Ri, C.; Sun, H. Enhanced removal of aged and differently functionalized polystyrene nanoplastics using ball-milled magnetic pinewood biochars. *Environ. Pollut.* **2023**, *316*, 120696. [CrossRef] [PubMed]

104. Li, Y.; Zimmerman, A.R.; He, F.; Chen, J.; Han, L.; Chen, H.; Hu, X.; Gao, B. Solvent-free synthesis of magnetic biochar and activated carbon through ball-mill extrusion with Fe$_3$O$_4$ nanoparticles for enhancing adsorption of methylene blue. *Sci. Total Environ.* **2020**, *722*, 137972. [CrossRef] [PubMed]

105. Yang, X.; Luo, K.; Pi, Z.; Shen, P.; Zhou, P.; He, L.; Li, X.; Yang, Q. Insight to the mechanism of tetracycline removal by ball-milled nanocomposite CeO$_2$/Fe$_3$O$_4$/biochar: Overlooked degradation behavior. *Sep. Purif. Technol.* **2023**, *307*, 122703. [CrossRef]

106. Ai, D.; Wei, T.; Meng, Y.; Chen, X.; Wang, B. Ball milling sulfur-doped nano zero-valent iron @biochar composite for the efficient removal of phosphorus from water: Performance and mechanisms. *Bioresour. Technol.* **2022**, *357*, 127316. [CrossRef] [PubMed]

107. Wang, M.; Yan, J.; Diao, Y.; Zhou, X.; Luo, T.; Wang, H.; Quan, G.; Sun, X.; Wang, J. Ball milled Mg/Al hydroxides modified nitrogen-rich biochar for arsenic removal: Performance and governing mechanism. *Carbon Res.* **2023**, *2*, 30. [CrossRef]

108. Cui, S.; Zhang, R.; Peng, Y.; Gao, X.; Li, Z.; Fan, B.; Guan, C.Y.; Beiyuan, J.; Zhou, Y.; Liu, J.; et al. New insights into ball milling effects on mgal-ldhs exfoliation on biochar support: A case study for cadmium adsorption. *J. Hazard. Mater.* **2021**, *416*, 126258. [CrossRef] [PubMed]

109. Yang, X.; Wang, L.; Tong, J.; Shao, X.; Chen, R.; Yang, Q.; Li, F.; Xue, B.; Li, G.; Han, Y.; et al. Synthesis of hickory biochar via one-step acidic ball milling: Characteristics and titan yellow adsorption. *J. Clean. Prod.* **2022**, *338*, 130575. [CrossRef]

110. Venkataraman, A.; Amadi, E.V.; Chen, Y.; Papadopoulos, C. Carbon nanotube assembly and integration for applications. *Nanoscale Res. Lett.* **2019**, *14*, 220. [CrossRef]

111. Huang, J.Y.; Yasuda, H.; Mori, H. Highly curved carbon nanostructures produced by ball-milling. *Chem. Phys. Lett.* **1999**, *303*, 130–134. [CrossRef]

112. Oh, Y.; Choi, J.; Kim, Y.; Kim, K.; Baik, S. The effects of ball milling process on the diameter dependent fracture of single walled carbon nanotubes. *Scr. Mater.* **2007**, *56*, 741–744. [CrossRef]

113. Liu, Z.T.; Fei, Z.H.; Wang, J.P.; Li, Z.X.; Chen, J.; Wu, X.H. Adsorption of nitrobenzene using short open-ended carbon nanotubes as adsorbent. *Asian J. Chem.* **2014**, *26*, 903–905. [CrossRef]

114. Ahn, J.H.; Shin, H.S.; Kim, Y.J.; Chung, H. Structural modification of carbon nanotubes by various ball milling. *J. Alloys Compd.* **2007**, *434*, 428–432. [CrossRef]

115. Soares, O.S.G.P.; Rocha, R.P.; Gonçalves, A.G.; Figueiredo, J.L.; Órfão, J.J.M.; Pereira, M.F.R. Easy method to prepare N-doped carbon nanotubes by ball milling. *Carbon* **2015**, *91*, 114–121. [CrossRef]

116. Coa, F.; Strauss, M.; Clemente, Z.; Rodrigues Neto, L.L.; Lopes, J.R.; Alencar, R.S.; Souza Filho, A.G.; Alves, O.L.; Castro, V.; Barbieri, E.; et al. Coating carbon nanotubes with humic acid using an eco-friendly mechanochemical method: Application for Cu(II) ions removal from water and aquatic ecotoxicity. *Sci. Total Environ.* **2017**, *607–608*, 1479–1486. [CrossRef] [PubMed]

117. Bor, A.; Ichinkhorloo, B.; Uyanga, B.; Lee, J.; Choi, H. Cu/CNT nanocomposite fabrication with different raw material properties using a planetary ball milling process. *Powder Technol.* **2018**, *323*, 563–573. [CrossRef]

118. Jargalsaikhan, B.; Bor, A.; Lee, J.; Choi, H. Al/CNT nanocomposite fabrication on the different property of raw material using a planetary ball mill. *Adv. Powder Technol.* **2020**, *31*, 1957–1962. [CrossRef]

119. Liu, Y.B.; Zhang, X.M.; Deng, J.H.; Liu, Y. A novel CNTs-Fe$_3$O$_4$ synthetized via a ball-milling strategy as efficient fenton-like catalyst for degradation of sulfonamides. *Chemosphere* **2021**, *277*, 130305. [CrossRef]

120. Nguyen, H.P.; Cao, T.M.; Nguyen, T.T.; Van Pham, V. Improving photocatalytic oxidation of semiconductor (TiO$_2$, SnO$_2$, ZnO)/CNTs for nox removal. *J. Ind. Eng. Chem.* **2023**, *127*, 321–330. [CrossRef]

121. Olszewski, R.; Nadolska, M.; Lapinski, M.; Przesniak-Welenc, M.; Cieslik, B.M.; Zelechowska, K. Solvent-free synthesis of phosphonic graphene derivative and its application in mercury ions adsorption. *Nanomaterials* **2019**, *9*, 485. [CrossRef] [PubMed]

122. Guo, B.; Ji, X.; Wang, W.; Chen, X.; Wang, P.; Wang, L.; Bai, J. Highly flexible, thermally stable, and static dissipative nanocomposite with reduced functionalized graphene oxide processed through 3d printing. *Compos. Part B Eng.* **2021**, *208*, 108598. [CrossRef]

123. Rout, D.R.; Jena, H.M.; Baigenzhenov, O.; Hosseini-Bandegharaei, A. Graphene-based materials for effective adsorption of organic and inorganic pollutants: A critical and comprehensive review. *Sci. Total Environ.* **2023**, *863*, 160871. [CrossRef]

124. Yu, W.G.; Gao, X.F.; Yuan, Z.C.; Liu, H.H.; Wang, X.C.; Zhang, X.X. Facial fabrication of few-layer functionalized graphene with sole functional group through diels-alder reaction by ball milling. *RSC Adv.* **2022**, *12*, 17990–18003. [CrossRef] [PubMed]

125. Sivakumar, M.; Yadav, S.; Hung, W.S.; Lai, J.Y. One-pot eco-friendly synthesis of edge-carboxylate graphene via dry ball milling for enhanced removal of acid and basic dyes from single or mixed aqueous solution. *J. Clean. Prod.* **2020**, *263*, 121498. [CrossRef]

126. Chandran, S.V.; Narayanan, B.N. Copper oxide incorporated ball-mill produced less-defective graphene for hybrid supercapacitors. *Diam. Relat. Mater.* **2024**, *143*, 110842. [CrossRef]

127. Suvarna, K.S.; Binitha, N.N. Graphene preparation by jaggery assisted ball-milling of graphite for the adsorption of Cr(VI). *Mater. Today Proc.* **2020**, *25*, 236–240. [CrossRef]

128. Pan, P.F.; Wang, X.; Ji, Y.Q.; Dong, W.M.; Zhang, L.; Wang, L.; Zhang, M. One-step synthesis of ZrO_2 nanopowders dispersed with graphene by ball milling. *Ceram. Int.* **2020**, *46*, 24799–24804. [CrossRef]

129. Caicedo, F.M.C.; López, E.V.; Agarwal, A.; Drozd, V.; Durygin, A.; Hernandez, A.F.; Wang, C.L. Synthesis of graphene oxide from graphite by ball milling. *Diam. Relat. Mater.* **2020**, *109*, 108064. [CrossRef]

130. Zhuang, S.; Lee, E.S.; Lei, L.; Nunna, B.B.; Kuang, L.; Zhang, W. Synthesis of nitrogen-doped graphene catalyst by high-energy wet ball milling for electrochemical systems. *Int. J. Energy Res.* **2016**, *40*, 2136–2149. [CrossRef]

131. Zhao, S.Q.; Chen, D.; Wei, F.H.; Chen, N.N.; Liang, Z.; Luo, Y. Removal of congo red dye from aqueous solution with nickel-based metal-organic framework/graphene oxide composites prepared by ultrasonic wave-assisted ball milling. *Ultrason. Sonochem.* **2017**, *39*, 845–852. [CrossRef] [PubMed]

132. Ye, W.; Chi, Q.Q.; Zhou, H.; Gao, P. Ball-milling preparation of titanium/graphene composites and its enhanced hydrogen storage ability. *Int. J. Hydrogen Energy* **2018**, *43*, 19164–19173. [CrossRef]

133. Wang, W.G.; Babu, D.D.; Huang, Y.Y.; Lv, J.Q.; Wang, Y.B.; Wu, M.X. Atomic dispersion of Fe/Co/N on graphene by ball-milling for efficient oxygen evolution reaction. *Int. J. Hydrogen Energy* **2018**, *43*, 10351–10358. [CrossRef]

134. Song, M.Y.; Choi, E.; Kwak, Y.J. Increase in the dehydrogenation rates and hydrogen-storage capacity of mg-graphene composites by adding nickel via reactive ball milling. *Mater. Res. Bull.* **2020**, *130*, 110938. [CrossRef]

135. Zhang, Y.; Cheng, Y.Q.; Song, J.H.; Zhang, Y.J.; Shi, Q.; Wang, J.X.; Tian, F.H.; Yuan, S.; Su, Z.; Zhou, C.; et al. Functionalization-assistant ball milling towards si/graphene anodes in high performance li-ion batteries. *Carbon* **2021**, *181*, 300–309. [CrossRef]

136. Kahimbi, H.; Hong, S.B.; Yang, M.H.; Choi, B.G. Simultaneous synthesis of nio/reduced graphene oxide composites by ball milling using bulk ni and graphite oxide for supercapacitor applications. *J. Electroanal. Chem.* **2017**, *786*, 14–19. [CrossRef]

137. Tan, M.A.; Qin, Y.; Luo, J.X.; Wang, Y.P.; Zhang, F.Z.; Zhao, X.H.; Lei, X.D. Cus loaded on reduced graphene oxide prepared by ball milling method as cathode material for high- power aqueous Cu-Al hybrid-ion batteries. *Electrochim. Acta* **2024**, *476*, 143734. [CrossRef]

138. Ahmad, J.; Sofi, F.A.; Mehraj, O.; Majid, K. Fabrication of highly photocatalytic active anatase TiO_2-graphene oxide heterostructures via solid phase ball milling for environmental remediation. *Surf. Interfaces* **2018**, *13*, 186–195. [CrossRef]

139. Cheng, J.P.; Xiong, D.P.; Jiang, W.Q.; Ye, W.B.; Song, P.; Feng, Z.Y.; He, M. SnO_2-MoO_2 nanoparticles coated on graphene oxide as a high-capacity, high-speed, long-life lithium-ion battery anode. *Chem. Phys. Lett.* **2024**, *835*, 140994. [CrossRef]

140. Ravichandran, S.; Sahadevan, J.; Sivaprakash, P.; Sagadevan, S.; Kim, I.; Tighezza, A.M.; Ali, A.; Muthu, S.E. Synthesis and physicochemical properties of graphene incorporated indium tin oxide nanocomposites for optoelectronic device applications. *Mat. Sci. Eng. B-Adv.* **2024**, *301*, 117199. [CrossRef]

141. Mondal, O.; Mitra, S.; Pal, M.; Datta, A.; Dhara, S.; Chakravorty, D. Reduced graphene oxide synthesis by high energy ball milling. *Mater. Chem. Phys.* **2015**, *161*, 123–129. [CrossRef]

142. Li, T.L.; Teng, Y.X.; Li, X.; Luo, S.J.; Xiu, Z.M.; Wang, H.T.; Sun, H.W. Sulfidated microscale zero-valent iron/reduced graphene oxide composite (S-mZVI/rGO) for enhanced degradation of trichloroethylene: The role of hydrogen spillover. *J. Hazard. Mater.* **2023**, *446*, 130657. [CrossRef] [PubMed]

143. Fu, F.; Dionysiou, D.D.; Liu, H. The use of zero-valent iron for groundwater remediation and wastewater treatment: A review. *J. Hazard. Mater.* **2014**, *267*, 194–205. [CrossRef] [PubMed]

144. Ambika, S.; Devasena, M.; Nambi, I.M. Synthesis, characterization and performance of high energy ball milled meso-scale zero valent iron in fenton reaction. *J. Environ. Manag.* **2016**, *181*, 847–855. [CrossRef] [PubMed]

145. Zhang, Y.; Li, D.; She, L.; Guo, F.; Jia, F.; Zhang, L.; Ai, Z.; Liu, X. Ball-milled zero-valent iron with formic acid for effectively removing Cu(II)-edta accomplished by edta ligands oxidative degradation and Cu(II) removal. *J. Hazard. Mater.* **2024**, *465*, 133009. [CrossRef] [PubMed]

146. Wei, J.; Zheng, Z.; Zhao, L.; Qiu, Z.; Zeng, D. Oxalic acid modification enables high efficiency and proton conductive of Fe-base amorphous toward acid orange II in wastewater removal. *Sep. Purif. Technol.* **2024**, *332*, 125768. [CrossRef]

147. Zhang, X.; Yao, Z.; Gao, Y.; Yan, S.; Peng, X.; Shen, W. Efficient Cu(II) removal with boronated zero-valent iron via inhibition of oxygen adsorption and enhanced electron transfer. *Appl. Surf. Sci.* **2024**, *654*, 159466. [CrossRef]

148. Hou, M.; Zhang, Y.; Jiao, X.; Ding, N.; Jiao, Y.; Pan, Y.; Xue, J.; Zhang, Y. Polyphenol-modified zero-valent iron prepared using ball milling technology for hexavalent chromium removal: Kinetics and mechanisms. *Sep. Purif. Technol.* **2023**, *326*, 124874. [CrossRef]

149. Shen, W.; Zhang, J.; Xiao, M.; Zhang, X.; Li, J.; Jiang, W.; Yan, J.; Qin, Z.; Zhang, S.; He, W.; et al. Ethylenediaminetetraacetic acid induces surface erosion of zero-valent iron for enhanced hexavalent chromium removal. *Appl. Surf. Sci.* **2020**, *525*, 146593. [CrossRef]

150. Zeng, X.; Wang, L.; Zhang, Y.; Zhou, S.; Yu, Z.; Liu, X.; Chen, C. Enhanced removal of organic pollutants by ball-milled Fes/ZVl activated persulfate process: Characterization, performance, and mechanisms. *Surf. Interfaces* **2022**, *29*, 101697. [CrossRef]

151. Du, M.; Kuang, H.; Zhang, Y.; Zeng, X.; Yi, C.; Hussain, I.; Huang, S.; Zhao, S. Enhancement of ball-milling on pyrite/zero-valent iron for persulfate activation on imidacloprid removal in aqueous solution: A mechanistic study. *J. Environ. Chem. Eng.* **2021**, *9*, 105647. [CrossRef]

152. Song, X.; Tian, J.; Ma, J.; Ni, J.; Liu, D.; Wang, W.; Shi, W.; Yuan, Y.; Cui, F.; Chen, Z. Peroxydisulfate activation by a versatile ball-milled nZVl@MoS$_2$ composite: Performance and potential activation mechanism. *Chem. Eng. J.* **2023**, *453*, 139830. [CrossRef]

153. Wu, S.; Deng, S.; Ma, Z.; Liu, Y.; Yang, Y.; Jiang, Y. Ferrous oxalate covered zvi through ball-milling for enhanced catalytic oxidation of organic contaminants with persulfate. *Chemosphere* **2022**, *287*, 132421. [CrossRef] [PubMed]

154. Yang, Z.; Ding, G.; Yan, L.; Wang, R.; Zhang, W.; Wang, X.; Rao, P. Ball-milled sulfide iron-copper bimetals based composite permeable materials for Cr(VI) removal: Effects of preparation parameters and kinetics study. *Chemosphere* **2023**, *338*, 139388. [CrossRef] [PubMed]

155. Zhang, T.; Zhao, Y.; Kang, S.; Bai, H.; Gu, W.; Fang, D.; Komarneni, S.; Zhang, Q. Mechanical activation of zero-valent iron (ZVl) in the presence of CaCo$_3$: Improved reactivity of zvi for enhancing As(III) removal from water. *J. Clean. Prod.* **2021**, *286*, 124926. [CrossRef]

156. Zhao, J.; Su, A.; Tian, P.; Tang, X.; Collins, R.N.; He, F. Arsenic (III) removal by mechanochemically sulfidated microscale zero valent iron under anoxic and oxic conditions. *Water Res.* **2021**, *198*, 117132. [CrossRef] [PubMed]

157. He, K.; Wang, S.; Liu, Y.; Cao, Z.; Yang, L.; He, F. Enhanced removal of hexavalent chromium by lignosulfonate modified zero valent iron: Reaction kinetic, performance and mechanism. *Sci. Total Environ.* **2023**, *857*, 159397. [CrossRef] [PubMed]

158. Zhou, F.; Liu, Q.; Qin, Y.; Liu, W.; Zhang, L. Efficient Fe(III)/Fe(II) cycling mediated by l-cysteine functionalized zero-valent iron for enhancing Cr(VI) removal. *J. Hazard. Mater.* **2023**, *456*, 131717. [CrossRef]

159. Shi, Y.; Wang, D.; Gao, F.; Liu, L.; Liu, Q.; Wang, L.; Tang, J. Mechanochemical nitridation of micron zero-valent iron for enhanced dechlorination of trichloroethylene: Mechanistic insights into nitrogen sources and ball milling conditions. *Sep. Purif. Technol.* **2024**, *337*, 126381. [CrossRef]

160. Hu, Y.; Ke, K.; Sun, H.; Wang, Z.; Zhang, X.; Shen, W.; Huang, S.; Lu, W.; Wang, X. Coffee grounds modified zero-valent iron for efficient heavy metal removal. *J. Water Process. Eng.* **2023**, *56*, 104397. [CrossRef]

161. Li, Z.; Zhao, Z.; Fan, J.; Wang, W.; Li, L.; Liu, J. Spinel ferrite-enhanced Cr(VI) removal performance of micro-scale zero-valent aluminum: Synergistic effects of oxide film destruction and lattice spacing expansion. *Sep. Purif. Technol.* **2022**, *294*, 121110. [CrossRef]

162. Ren, T.; Zhang, Y.; Liu, J.; Zhang, Y.; Yang, S. Ethanol-assisted mechanical activation of zero-valent aluminum for fast and highly efficient removal of Cr(VI). *Appl. Surf. Sci.* **2020**, *533*, 147543. [CrossRef]

163. Wu, S.; Yang, S.Y.; Liu, S.J.; Zhang, Y.X.; Ren, T.F.; Zhang, Y.Q. Enhanced reactivity of zero-valent aluminum with ball milling for phenol oxidative degradation. *J. Colloid Interface Sci.* **2020**, *560*, 260–272. [CrossRef] [PubMed]

164. Jiang, Y.T.; Yang, S.Y.; Wang, M.Q.; Xue, Y.C.; Liu, J.Q.; Li, Y.; Zhao, D.Y. A novel ball-milled aluminum-carbon composite for enhanced adsorption and degradation of hexabromocyclododecane. *Chemosphere* **2021**, *279*, 130520. [CrossRef] [PubMed]

165. Hu, Q.; Wang, Q.; Feng, C.; Zhang, Z.; Lei, Z.; Shimizu, K. Insights into mathematical characteristics of adsorption models and physical meaning of corresponding parameters. *J. Mol. Liq.* **2018**, *254*, 20–25. [CrossRef]

166. Zhao, J.; Liu, J.; Li, N.; Wang, W.; Nan, J.; Zhao, Z.; Cui, F. Highly efficient removal of bivalent heavy metals from aqueous systems by magnetic porous Fe$_3$O$_4$-MnO$_2$: Adsorption behavior and process study. *Chem. Eng. J.* **2016**, *304*, 737–746. [CrossRef]

167. Ye, H.Y.; Yu, K.; Li, B.; Guo, J.Z. Study on adsorption properties and mechanism of sodium hydroxide-modified ball-milled biochar to dislodge lead(II) and mb from water. *Biomass Convers. Biorefinery* **2023**. [CrossRef]

168. Li, Y.; Liu, X.; Zhang, P.; Wang, X.; Cao, Y.; Han, L. Qualitative and quantitative correlation of physicochemical characteristics and lead sorption behaviors of crop residue-derived chars. *Bioresour. Technol.* **2018**, *270*, 545–553. [CrossRef] [PubMed]

169. Xiao, J.; Hu, R.; Chen, G. Micro-nano-engineered nitrogenous bone biochar developed with a ball-milling technique for high-efficiency removal of aquatic Cd(II), Cu(II) and Pb(II). *J. Hazard. Mater.* **2020**, *387*, 121980. [CrossRef]

170. Li, R.; Zhang, Y.; Deng, H.; Zhang, Z.; Wang, J.J.; Shaheen, S.M.; Xiao, R.; Rinklebe, J.; Xi, B.; He, X.; et al. Removing tetracycline and Hg(II) with ball-milled magnetic nanobiochar and its potential on polluted irrigation water reclamation. *J. Hazard. Mater.* **2020**, *384*, 121095. [CrossRef]

171. Qu, J.; Wu, Z.; Liu, Y.; Li, R.; Wang, D.; Wang, S.; Wei, S.; Zhang, J.; Tao, Y.; Jiang, Z.; et al. Ball milling potassium ferrate activated biochar for efficient chromium and tetracycline decontamination: Insights into activation and adsorption mechanisms. *Bioresour. Technol.* **2022**, *360*, 127407. [CrossRef] [PubMed]

172. Liu, D.; Cheng, J.; Xiao, X.; Liao, X.; Zhang, S.; Shi, B. Pyrolysis combined ball-milling for the preparation of biochar from chinese baijiu distillers' grains for the adsorption of heavy metal ions. *Ind. Crops Prod.* **2023**, *203*, 117234. [CrossRef]

173. Zawrah, M.F.; Alhogbi, B.G. Preparation and characterization of SiO$_2$@C nanocomposites from rice husk for removal of heavy metals from aqueous solution. *Ceram. Int.* **2021**, *47*, 23240–23248. [CrossRef]

174. Qu, J.; Zhang, B.; Tong, H.; Liu, Y.; Wang, S.; Wei, S.; Wang, L.; Wang, Y.; Zhang, Y. High-efficiency decontamination of Pb(II) and tetracycline in contaminated water using ball-milled magnetic bone derived biochar. *J. Clean. Prod.* **2023**, *385*, 135683. [CrossRef]

175. Qu, J.; Che, N.J.; Niu, G.L.; Liu, L.F.; Li, C.L.; Liu, Y.L. Iron/manganese binary metal oxide-biochar nano-composites with high adsorption capacities of Cd^{2+}: Preparation and adsorption mechanisms. *J. Water Process. Eng.* **2023**, *51*, 103332. [CrossRef]

176. Di, Z.C.; Ding, J.; Peng, X.J.; Li, Y.H.; Luan, Z.K.; Liang, J. Chromium adsorption by aligned carbon nanotubes supported ceria nanoparticles. *Chemosphere* **2006**, *62*, 861–865. [CrossRef] [PubMed]

177. Zou, H.; Hu, E.; Yang, S.; Gong, L.; He, F. Chromium(VI) removal by mechanochemically sulfidated zero valent iron and its effect on dechlorination of trichloroethene as a co-contaminant. *Sci. Total Environ.* **2019**, *650*, 419–426. [CrossRef] [PubMed]

178. Cao, Y.; Xiao, W.; Shen, G.; Ji, G.; Zhang, Y.; Gao, C.; Han, L. Carbonization and ball milling on the enhancement of Pb(II) adsorption by wheat straw: Competitive effects of ion exchange and precipitation. *Bioresour. Technol.* **2019**, *273*, 70–76. [CrossRef]
179. Du, H.; Xi, C.; Tang, B.; Chen, W.; Deng, W.; Cao, S.; Jiang, G. Performance and mechanisms of naoh and ball-milling co-modified biochar for enhanced the removal of Cd^{2+} in synthetic water: A combined experimental and dft study. *Arab. J. Chem.* **2022**, *15*, 103817. [CrossRef]
180. Meng, P.; Fang, X.; Maimaiti, A.; Yu, G.; Deng, S. Efficient removal of perfluorinated compounds from water using a regenerable magnetic activated carbon. *Chemosphere* **2019**, *224*, 187–194. [CrossRef]
181. Lyu, H.; Gao, B.; He, F.; Zimmerman, A.R.; Ding, C.; Tang, J.; Crittenden, J.C. Experimental and modeling investigations of ball-milled biochar for the removal of aqueous methylene blue. *Chem. Eng. J.* **2018**, *335*, 110–119. [CrossRef]
182. Naghdi, M.; Taheran, M.; Pulicharla, R.; Rouissi, T.; Brar, S.K.; Verma, M.; Surampalli, R.Y. Pine-wood derived nanobiochar for removal of carbamazepine from aqueous media: Adsorption behavior and influential parameters. *Arab. J. Chem.* **2019**, *12*, 5292–5301. [CrossRef]
183. Zhang, Q.; Wang, J.; Lyu, H.; Zhao, Q.; Jiang, L.; Liu, L. Ball-milled biochar for galaxolide removal: Sorption performance and governing mechanisms. *Sci. Total Environ.* **2019**, *659*, 1537–1545. [CrossRef] [PubMed]
184. Huang, J.; Zimmerman, A.R.; Chen, H.; Gao, B. Ball milled biochar effectively removes sulfamethoxazole and sulfapyridine antibiotics from water and wastewater. *Environ. Pollut.* **2020**, *258*, 113809. [CrossRef] [PubMed]
185. Ma, Y.; Zeng, C.; Ding, Y.; Tang, J.; Mašek, O.; Deng, Z.; Mu, R.; Zhang, Z. Facile synthesis of ball milling and magnetization co-modified sludge-derived biochar for efficient adsorbing environmental concentration sulfamethoxazole from various waters: Performance and mechanism. *Sep. Purif. Technol.* **2024**, *331*, 125584. [CrossRef]
186. Tang, J.; Ma, Y.; Cui, S.; Ding, Y.; Zhu, J.; Chen, X.; Zhang, Z. Insights on ball milling enhanced iron magnesium layered double oxides bagasse biochar composite for ciprofloxacin adsorptive removal from water. *Bioresour. Technol.* **2022**, *359*, 127468. [CrossRef] [PubMed]
187. Huang, Z.; Yi, Y.; Zhang, N.; Tsang, P.E.; Fang, Z. Removal of fluconazole from aqueous solution by magnetic biochar treated by ball milling: Adsorption performance and mechanism. *Environ. Sci. Pollut. R* **2022**, *29*, 33335–33344. [CrossRef] [PubMed]
188. Zhang, Y.; Zheng, Y.; Yang, Y.; Huang, J.; Zimmerman, A.R.; Chen, H.; Hu, X.; Gao, B. Mechanisms and adsorption capacities of hydrogen peroxide modified ball milled biochar for the removal of methylene blue from aqueous solutions. *Bioresour. Technol.* **2021**, *337*, 125432. [CrossRef] [PubMed]
189. Jiang, F.; Wei, C.; Yu, Z.; Ji, L.; Liu, M.; Cao, Q.; Wu, L.; Li, F. Fabrication of iron-containing biochar by one-step ball milling for Cr(VI) and tetracycline removal from wastewater. *Langmuir* **2023**, *39*, 18958–18970. [CrossRef]
190. Yan, N.; Hu, B.; Zheng, Z.; Lu, H.; Chen, J.; Zhang, X.; Jiang, X.; Wu, Y.; Dolfing, J.; Xu, L. Twice-milled magnetic biochar: A recyclable material for efficient removal of methylene blue from wastewater. *Bioresour. Technol.* **2023**, *372*, 128663. [CrossRef]
191. Sun, Y.F.; Zhang, A.M.; Yin, Y.; Dong, Y.M.; Cui, Y.C.; Zhang, X.; Hong, J.M. The investigation of adsorptive performance on modified multi-walled carbon nanotubes by mechanical ball milling. *Mater. Chem. Phys.* **2007**, *101*, 30–34. [CrossRef]
192. Araga, R.; Kali, S.; Sharma, C.S. Coconut-shell-derived carbon/carbon nanotube composite for fluoride adsorption from aqueous solution. *CLEAN–Soil Air Water* **2019**, *47*, 1800286. [CrossRef]
193. Feng, K.; Xu, Z.; Gao, B.; Xu, X.; Zhao, L.; Qiu, H.; Cao, X. Mesoporous ball-milling iron-loaded biochar for enhanced sorption of reactive red: Performance and mechanisms. *Environ. Pollut.* **2021**, *290*, 117992. [CrossRef] [PubMed]
194. Tang, J.; Ma, Y.; Zeng, C.; Yang, L.; Cui, S.; Zhi, S.; Yang, F.; Ding, Y.; Zhang, K.; Zhang, Z. Fe-al bimetallic oxides functionalized-biochar via ball milling for enhanced adsorption of tetracycline in water. *Bioresour. Technol.* **2023**, *369*, 128385. [CrossRef] [PubMed]
195. Gupta, S.; Sireesha, S.; Sreedhar, I.; Patel, C.M.; Anitha, K.L. Latest trends in heavy metal removal from wastewater by biochar based sorbents. *J. Water Process. Eng.* **2020**, *38*, 101561. [CrossRef]
196. Baskar, A.V.; Bolan, N.; Hoang, S.A.; Sooriyakumar, P.; Kumar, M.; Singh, L.; Jasemizad, T.; Padhye, L.P.; Singh, G.; Vinu, A.; et al. Recovery, regeneration and sustainable management of spent adsorbents from wastewater treatment streams: A review. *Sci. Total Environ.* **2022**, *822*, 153555. [CrossRef]